Emergent Spin Ordering at C_{60} interfaces

Fatma Ali Salim Al Ma'Mari

School of Physics and Astronomy

University of Leeds

Submitted in accordance with the requirements for the degree of

Doctor of Philosophy

August 2016

Intellectual Property Statement

The candidate confirms that the work submitted is her own, except where work which has formed part of jointly authored publications has been included. The contribution of the candidate and the other authors to this work has been explicitly indicated below. The candidate confirms that appropriate credit has been given within the thesis where reference has been made to the work of others.

This copy has been supplied on the understanding that it is copyright material and that no quotation from the thesis may be published without proper acknowledgement.

The right of Fatma Al Ma'Mari to be identified as Author of this work has been asserted by her in accordance with the Copyright, Designs and Patents Act 1988.

©2016 The University of Leeds and Fatma Al Ma'Mari.

For all publications Dr. O. Céspedes suggested experiments, discussed results and wrote the manuscripts. Also for all thesis, Dr. O. Céspedes provided guidance for experiments and data analysis. The figures 4.5,4.9 and 5.5 are directly attributable to him. Design and optimisation of C_{60} is done by Dr. M.C. Wheeler and Dr. O. Céspedes. The magnetometry data in section 5.2.1.2 was obtained in collaboration with Mr. M. Rogers. The experiment in section 5.2.3 was performed by Mr. M. Rogers using ALBA synchtron facilities. However, the analysis of this section was done by Fatma Al Ma'Mari.

Work from the following jointly authored publications is presented in this thesis:

F. Al Ma'Mari, T. Moorsom, G. Teobaldi, W. Deacon, T. Prokscha, H. Luetkens, S. Lee, G. E. Sterbinsky, D. A. Arena, D. A. MacLaren, M. Flokstra, M. Ali, M. C. Wheeler, G. Burnell, B. J. Hickey O. C*é*spedes. Beating the Stoner criterion usingmolecular interfaces. *Nature*, 524, 69–73 (2015). Chapter 4 and section 5.2.1.1.

Work attributable to the candidate: grew and characterized the samples, conducted the magnetometry and mSR, and contributed to the data analysis. **Work attributable to others:** Mr. T. Moorsom contributed to samples growth and characterisation includes μSR. Dr. G. Teobaldi performed and analysed the DFT simulations; Mr. W. Deacon grew and characterized some of the Cu/C_{60} multilayers; Dr. T. Prokscha, Dr. H. Luetkens, Dr. S. Lee and Dr. M. Flokstra contributed to the design measurement and analysis of the μSR experiments; Dr. D. A. MacLaren contributed to the TEM images and structural analysis; Dr. G.E. Sterbinsky, and Dr. D. A. Arena performed the X-ray magnetic circular dichroism and X-ray absorption spectroscopy measurements; Dr. M. C. Wheeler contributed to the sample structure, measurement setup, discussion and ideas; Dr. M. Ali, Dr. G. Burnell and Prof. B.J. Hickey: general help with this work and with discussion/ideas. Dr. O. C*é*spedes designed the study, analysed the data and wrote the manuscript. All authors discussed the results and commented on the manuscript.

Acknowledgements

Firstly, I would like to express my sincere gratitude to my supervisor Dr. Oscar C*é*spedes for his continuous support during my Ph.D study and for his patience, motivation, and immense knowledge. His excellent scientific qualities, great humanity and his guidance helped me all the time of the research process. Special thanks to him for always raising my morale and trying to help me with his comprehensive advice, for inspiring me with his deep insight in experimental physics. I really cannot find enough words to express my sincere appreciation and admiration. Thanks! I would also like to thank my co-supervisor Prof. Chris Marrows and the rest of the academic staff: Prof. Bryan. J. Hickey, Dr. Thomas A Moore and Dr Satoshi Sasaki for their insightful comments and encouragement. Special thanks to Prof. Gavin Burnell and Dr. Mannan Ali for their vast experience and their infinite patience to help everyone in the group.

My sincere thanks also goes to the "C_{60}" team. In particular, I am grateful to Dr. May Wheeler: her sound character, her exceptional personality and her rare value as a person helped and guided me in this interesting field. Special thanks go to her for her constant support and encouragement. Thanks to Tim Morsoom because he continually and convincingly conveyed a spirit of adventure in regard to research, and an excitement in regard physics in general. I am also extremely fortunate to know and work with Matthew Rogers under a stimulating atmosphere. He is a wonderful and friendly person who was instrumental in helping me. I have greatly benefited from his keen scientific insight and very much appreciated his enthusiasm and willingness about research. Thanks to Shoug alghamdi for letting me practice my Arabic and being a wonderful sister. I would like to thank the "night lab club" team: Dr. Priyasmita Sinha and Kowsar Shahbazi for the the sleepless nights we worked together at the lab, and for all the fun we have had in the last few years. I would also like to thank Amy Westerman, George Stefanou and Arpita Mitra for being great friends and being always beside me. I would like to thank my former officemates: Robert Buda and Dr. Susan Riley and the current ones: Dr. Katharina Zeissler and Benjamin Steele for having a great environment. I

sincerely thank Dr. Joe Batley for his help and his inspiration in transport measurements. I would like to thank Franz Herling as well for his code and his valuable discussion about weak localisation effect. Also, I want to thank Dr. Rowan Temple, Dr. Sophie Morley and Dr. Philippa Shepley for their kindness; they are willing to give their helping hands as soon as I am in need. I would like to express my full appreciation to the cryogenic technicians: John Turton, the late Philip Cale, Brian Gibbs and Luck Bone for infinite patience in filling the cryostat whenever I ask. I thank all the members in condensed matter physics group for the stimulating atmosphere; you supported me greatly and were always willing to help me. I would also like to thank Dr. Thomas Prokscha, Dr. Hubertus Luetkens at PSI, who made the muon experiments so interesting and enjoyable. I would like to extend a very heartfelt thank to my friends Neveen for her positive energy, gentle nature and courage.

I am grateful to this Sultan Qaboos University to give the opportunity to study here, I could not have gone through the doctoral program overseas without their financial support.

And finally, I would like to express my deepest appreciation and thankfulness to my parents, sisters and my brother for always being here although far away. Only their continuous support and love made this work possible.

Thank you very much, everyone!

Abstract

This work is a pioneer study on the role played by molecular interfaces in altering the electronic states of non-ferromagnetic materials. Here, we consider diamagnetic copper and paramagnetic manganese and scandium, to overcome the Stoner criterion and make them magnetically ordered at room temperature. The mechanism is mediated by the charge transfer from the transition metal and hybridization with molecular carbon, creating new 3d-π states that drastically modify the electron energy bands around the Fermi energy of both metal and molecule. This effect is achieved via interfaces between metallic thin films and C_{60} molecular layers. The emergent spin ordering arising in these systems is measured using magnetometry shows magnetically ordered behaviour at room temperature, but dependent on the thickness and continuity of the metallic layer. To determine how in the layered structure the emergent spin ordering is distributed, low-energy muon spin spectroscopy is utilised by studying the depolarization process of low-energy muons implanted in the sample. This technique indicates localised spin-ordered states at, and close to, the metallo-molecular interface. X-ray absorption spectroscopy provides an excellent tool for identifying the emergent spin ordering of specific elements within a sample. The change in the molecular orbitals of C_{60} due to charge transfer and 3d-π hybridization is evaluated based on this technique. The presence of spin ordering in a non-magnetic metallic host due to molecular charge transfer has a drastic effect not only on the magnetic but also on the transport properties of the system. The decisive role of the molecular interfaces in the physics of spin dependent scattering within a non-magnetic host has been demonstrated. Localised spin ordering leads to changes in the Kondo and weak localisation effects with applications in low temperature thermometry and quantum devices. It is found that there is an additional magnetic scattering that has a pronounced contribution when C_{60} molecules are embedded into the non-magnetic Cu and hence creates localised spins. The localised spin ordering that emerged at molecular interfaces is a new approach for novel generation of materials for future spintronics devices.

CONTENTS

Abbreviations

AC	alternating current	AFM	atomic force microscopy
DC	direct current	DOS	density of states
E_F	Fermi energy	FCC	face centred cubic
FM	ferromagnet	HOMO	highest occupied molecular orbital
IV	current-voltage	LE-μSR	low energy muon spin rotation and relaxation
LUMO	lowest unnoccupied molecular orbital	MR	magnetoresistance
NM	normal metal	OSC	organic semiconductor
PZT	piezoelectric	RF	radio frequency
RMS	root mean square	SQUID	superconducting quantum interference device
TEM	transmission electron microscopy	UHV	ultra high vacuum
VSM	vibrating sample magnetometry	WL	weak localisation
XAS	x-ray absorption spectroscopy	XMCD	x-ray magnetic circular dichroism
XRD	x-ray diffraction	XRR	x-ray reflection
ZFC	zero field cooling	ZFR	zero field remanent

CHAPTER 1

Introduction

Spintronics, or the functional control of the electron spin in electronic devices, is a promising research field that has attracted scientific and engineering interest. It takes full advantage of the spin of the electron instead of or in addition to the charge. The possibility of performing electronics with the spin of the electron is fundamental for potential future devices with high processing speed, low power consumption, that are non-volatile and for quantum computing. Organic spintronics, by combining spintronics and organic electronics, has recently grown into a massive research activity [1–3]. The great promise that is held by organic semiconductors (OSCs) for novel electronics and spintronic applications is due to recyclability and the interesting properties of molecular materials, such as both mechanical [4–7] and chemical flexibility [1]. However, the attractive aspect for OSCs in spintronic applications is the extremely long spin lifetimes in some materials [8; 9], thus the spin polarisation of the carriers can be maintained for a longer time than their inorganic counterparts. This feature, is as a result of the small spin-orbit interaction [10–13], associated with light-element compounds: carbon is a light atom that has a low atomic number (Z) and the strength of spin-orbit interaction is proportional to Z^4. However, C_{60} has higher spin-orbit interaction due to the curvature of the molecule compared to other carbon allotropes [11]. A very weak hyperfine interaction in ^{12}C further increases the spin lifetime [14], hence C_{60} molecules have a considerable advantage compared to organic materials containing hydrogen, which have a stronger hyperfine interaction.

A particularly intriguing material system for advanced spintronic applications has arisen from the peculiar interaction between organic molecules and metals, forming hybrid interfaces or spinterfaces, as coined by Sanvito [15]. The hybrid organic/metal interfaces have provided new functionalities beyond those of conventional inorganic materials such as active selection of the amplitude and sign of the spin polarisation (that is, the imbalance around the Fermi energy between spin-up and spin-down states) that is not present in conventional spintronics [1].They have presented a new pathway for tailoring the electronic and magnetic properties at these hybrid interfaces which hold significant promise towards engineering the performance of molecular spintronic devices [2]. A lot of recent interest has been focused on such hybrid interfaces involving carbon based molecules and significant advances have been made in understanding their electronic and magnetic properties. The hybrid metal-carbon states are formed

due to charge transfer and hybridization between the d-orbitals of transition metals and the π carbon orbitals. These states strongly affect the electronic and magnetic properties of both materials due to a spin polarized charge transfer [3; 4; 16]. Over the past decade, studies have focused on the interaction between molecules and magnetic transition metals, where unexpected magnetic behaviour has been reported, even at room temperature [3; 16–24].

This thesis presents a new perspective in the field of molecular spintronics by studying non-magnetic transition metals. It demonstrates the crucial role of the molecular interfaces in transforming a non-magnetic element, such as diamagnetic copper or paramagnetic manganese and scandium, into a magnetic material when it comes into contact with C_{60} molecules. The interaction between the molecules and the metal leads to a change in the density of states (DOS) at the Fermi energy (E_F) and/or the exchange interaction between the electrons, as described by the Stoner criterion for ferromagnetism [25]. The framework of this study is established by using C_{60} molecules, due to their structural simplicity and robustness. C_{60} films have high electron affinity [26; 27] and a lowest unoccupied molecular orbital [28; 29] which prompts a high charge transfer and allows interfacial manipulation.

Throughout this thesis, the interplay at the interface between C_{60} and metals is investigated using a broad range of experimental techniques. It has been shown that the properties of both C_{60} and metals can be manipulated through the metallo-molecular interfaces. To understand this phenomenon, the relevant theoretical concepts are introduced in chapter 2. In this chapter, the physical principles of magnetic ordering in metals and the corresponding Stoner criterion are described. A general introduction to molecular magnetism and the key properties of organic semiconductors (OSCs) are considered as well as their possible applications. In the latter part of chapter 2, the theory behind the mechanisms of magnetic scattering is summarized at a required level for understanding the results presented in this work.

Chapter 3 describes the main experimental methods used in this work, including sample deposition, structural, magnetic and transport characterisation. Each technique probes the specific details necessary to further our understanding of metallo-molecular

interfacial phenomenon. The samples are superlattices deposited by a combination of sputter deposition of the metals and *in-situ* thermal sublimation of C_{60}. X-ray reflectivity and atomic force microscopy have been used to investigate the structural surface morphology of the samples. The magnetic properties are determined via superconducting quantum interference device (SQUID) magnetometry. Synchrotron radiation techniques such as X-ray absorption spectroscopy (XAS), X-ray magnetic circular dichroism (XMCD) and low energy muon spin spectroscopy (LE-μSR) contribute to the understanding of these magnetic systems which are difficult to detect using SQUID magnetometry. SQUID magnetometry is sensitive to the total magnetisation of the measured sample whereas XAS and LE-μSR allow element specificity and depth resolution of magnetic properties, respectively. Low temperature transport measurements have been utilised as a probe to detect the magnetic scattering due to the spin ordering.

In this work, the emergent magnetic ordering arising from interfaces between non-magnetic transition metals and C_{60} molecules is outlined in two results chapters: chapter 4 presents the diamagnetic/C_{60} interfaces and chapter 5 discusses the paramagnetic/-C_{60} interfaces. A comprehensive study of this emergent magnetism has been pursued by using magnetometry, LE-μSR and XAS as well as XMCD. For instance, information about the total magnetisation of the emergent spin ordering within the samples is provided by magnetometry, whereas LE-μSR is used to confirm where the magnetisation is localised, as this technique is sensitive to the local magnetism at a specific sample depth. The contribution of different elements is distinguished by XAS and XMCD. The latter allows element-selective magnetic properties to be obtained by taking the difference in the absorption of two XAS measurements recorded with opposite light helicity. The contrast provided by XMCD is used as a significant magnetic characterisation of the emergent spin ordering in C_{60}. The changes to the electronic structure of C_{60} due to interfacial effects are also outlined. The unique results given by each technique are discussed in detail.

The potential of metallo-molecular interfaces for spintronics devices has been investigated using low temperature electronic transport, and is presented in chapter 6. The magnetic scattering due to the emergent spin ordering of the hybridised C_{60} molecular orbitals with the 3d band of the diamagnetic Cu has been detected through two ef-

fects: Kondo and weak localisation. These magnetotransport measurements allow the detection of very small concentrations of magnetic spins, which cannot be obtained by other techniques. Both mechanisms are discussed in this chapter.

CHAPTER 2

Theoretical background

2.1 Introduction

The main focus of this thesis lies in the role of hybrid interfaces between organic molecules and transition metals that can be used to tune the magnetic and electronic properties of transition metals. This chapter covers the basic principles of magnetism in metals and progresses to the principles of magnetism arising in organic molecules. The first part of the chapter focuses on the magnetic ordering in metals in which the physical principle of Stoner criterion for ferromagnetism is described. The second part introduces the magnetic ordering in organic molecules starting with the theoretical framework and its influence on the development on the emerging field of organic spintronics. In this part, the underlying physics of molecular magnetism and the evolution of the metallo-molecular interface are discussed. The key properties of organic semiconductors (OSCs) and C_{60} are considered. Finally, the concepts necessary for the understanding of electron magnetic scattering mechanisms are explained; the Kondo effect and weak localisation (WL).

2.2 Magnetic ordering in metals

2.2.1 Stoner criterion for ferromagnetism

Ferromagnetism is characterised by a spontaneous magnetisation even in the absence of a magnetic applied field. The alignment of the magnetic moments along a given direction in a ferromagnetic material is caused by the exchange interaction between them. The exchange interaction is an electrostatic interaction which depends on the relative position of charges. The electrostatic interaction together with the Pauli exclusion principle, which forbids two electrons from being in the same quantum state, can give rise to interactions among the magnetic moments and this plays a role in determining the magnetic properties.

To give a qualitative explanation, consider two electrons with spatial wave functions $\psi_a\ (r_1)$ and $\psi_b\ (r_2)$ and spatial coordinates r_1 and r_2, respectively. According to the Pauli exclusion principle, the total wave function of the two electrons must be antisymmetric under electron exchange. The total wave function is a product of the

space and spin wave functions. This asymmetry can be achieved in two ways by either possessing a symmetric spatial state combined with an antisymmetric spin wave function or vice versa. The former results in a spin singlet state χ_S *(S=0)* whereas the latter results in a spin triplet state χ_T *(S=1)* . The total wave function for the singlet case Ψ_S and the triplet case Ψ_T including both the spatial and spin components [30] are

$$\Psi_S = \frac{1}{\sqrt{2}} \left[\psi_a(r_1)\psi_b(r_2) + \psi_a(r_2)\psi_b(r_1)\right] \chi_S \tag{2.1}$$

$$\Psi_T = \frac{1}{\sqrt{2}} \left[\psi_a(r_1)\psi_b(r_2) - \psi_a(r_2)\psi_b(r_1)\right] \chi_T \tag{2.2}$$

The energy of the singlet $E_{(S)}$ and triplet $E_{(T)}$ states is given by

$$E_{S(T)} = \int \psi^*_{S(T)} \hat{\mathcal{H}} \psi_{S(T)} dr_1 dr_2 \tag{2.3}$$

where $\hat{\mathcal{H}}$ is the Hamiltonian. Assuming both spin parts of the wave functions are normalised, the difference between the energies is

$$E_S - E_T = 2 \int \psi^*_a(r_1)\psi^*_b(r_2)\hat{\mathcal{H}}\psi_a(r_2)\psi_b(r_1) dr_1 dr_2 \tag{2.4}$$

The exchange constant (or the exchange integral *J*) is evaluated as

$$J = \frac{E_S - E_T}{2} = \int \psi^*_a(r_1)\psi^*_b(r_2)\hat{\mathcal{H}}\psi_a(r_2)\psi_b(r_1) dr_1 dr_2 \tag{2.5}$$

Generalizing the Hamiltonian $\hat{\mathcal{H}}$ to include all pairs of atoms on the lattice sites *i,j* with the two spin states S_1 and S_2 will give

$$\hat{\mathcal{H}} = -2 \sum_{ij} J_{ij} \mathbf{S_1}.\mathbf{S_2} \tag{2.6}$$

If *J<0*, then E_S<E_T and the singlet state is favoured. The spins are aligned antiparallel to each other in the singlet state, which indicates an antiferromagnetic interaction. However, *J>0* indicates a ferromagnetic interaction whereby the triplet state is favoured and the spins are in parallel alignment [30; 31]. As stated in equation 2.2, the positive exchange integral implies a stable triplet state for electrons close together with an antisymmetric spatial wave function. This leads to a minimisation in the electrostatic energy when the electrons are further apart from each other. This is

consistent with Hund's rule which suggests that a single electron in the outer shells will be in parallel alignment with its neighbouring single occupancy electron before double occupation occurs with opposite alignment. Hence, we would expect that the majority of transition metals experience ferromagnetic interaction because they have unpaired electrons in the outer "d subshell". However, the majority of the transition metals exhibit paramagnetic or diamagnetic interactions and only three elements are ferromagnetic at room temperature: iron (Fe), cobalt (Co) and nickel (Ni).

Edmund C. Stoner in 1938 [32] derived a criterion that predicts which metals will exhibit itinerant ferromagnetism at room temperature. He revealed that ferromagnetism only appears when the exchange energy is greater than the kinetic energy required to flip a spin (i.e. the energy associated with a change in the occupancy of the up and down spin bands). This condition is fulfilled when the product of the exchange integral *J* and the density of states at Fermi energy D(E_F) are greater than unity

$$D(E_F)J \geq 1 \tag{2.7}$$

which is known as the Stoner criterion. In materials where equation 2.7 holds there is an associated energy splitting of the density of states (DOS) between the spin up and spin down bands called the exchange splitting Δ_{ex}. This splitting takes place even when there is no magnetic field applied and hence a spontaneous magnetisation is observed. Whenever the Stoner criterion is not satisfied, this spontaneous magnetisation will not appear. Figure 2.1a-b illustrates the spin-split energy bands for ferromagnetic nickel and the comparison between the exchange integral and density of states for different metallic elements. Stoner parameters for various elements are shown in figure 2.1c.

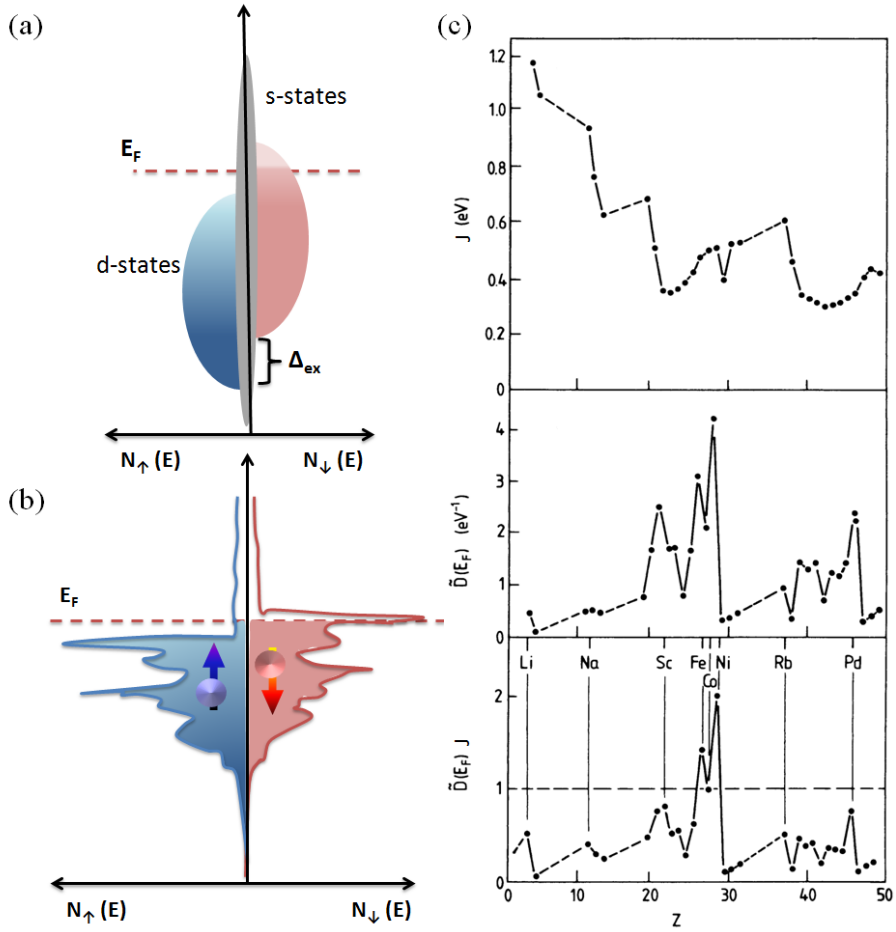

Figure 2.1: *(a) A diagram of density of states illustrates the broad s and the narrow d electron bands contribution to the density of states. (b) The spin-dependent density of states in a ferromagnetic element, in this case for nickel. The d states here are splitting with respect to each other due to the exchange interaction, adapted from [33]. (c) The Stoner parameters: the exchange integral J and the density of state at Fermi energy D(E_F) as a function of the atomic number Z. The bottom panel of (c) shows the product of the exchange integral and the density of states where the elements with values above one display ferromagnetism. Sc and Pd are close to achieving the ferromagnetic conditions, taken from [25]*

2.3 Magnetic ordering at molecular interfaces

2.3.1 Metallo-molecular interfaces

The use of organic molecules in magnetism has become an important focus of scientific interest in the last few decades [34–36]. The first theoretical framework for designing ferromagnetic (FM) molecular solids was proposed by McConnel [37]. He predicted that a FM spin-coupling occurs in a molecular system when a region of negative spin density in one molecule overlaps with a region of positive spin density in another molecule leaving incomplete cancellation of antiferromagnetic coupled spin components . This mechanism has been supported by a new term in the Hamiltonian assuming an interaction takes places between two neighbouring molecules *A* and *B* as

$$\hat{\mathcal{H}} = -2S_A S_B \sum_{ij} J_{ij} \rho_A^i \rho_B^j \tag{2.8}$$

where S_A and S_B are the total spins on molecule *A* and *B*, *i* and *j* indicate the atoms located in the *A* and *B* molecules respectively, and coupled by exchange integral J_{ij}. The spin densities on atoms *i* and *j* are ρ_A^i and ρ_B^j. By assuming the magnetic coupling constants are usually negative, then the two neighbouring molecules will exhibit a ferromagnetic exchange interaction if spin densities of the interaction atoms have opposite signs (negative product), which gives an overall positive coupling. However, this mechanism is limited to the magnetic exchange between aromatic free radicals where these structures possess atoms with unequal positive and negative spin densities. McConnel developed a second mechanism that describes the spin alignment in charge transfer complexes where the excited triplet states propagate along a donor and acceptor molecule and give rise to magnetic ordering [38; 39]. After that, the research in the molecular solid magnets developed progressively, where room temperature ferromagnetism was observed in 1991 [40]. However, the need for achieving magnetism at a single molecular level that is stable at room temperature was a challenging target from a technological perspective at that time. In this aspect, the magnetics research in molecular systems has considered new classes of materials that include embedding transition metal centres in molecules [41; 42]. This has been developed recently by growing molecules on magnetic surfaces to overcome the stability problems that had

been experienced by embedding metal centres in molecules. It also has shown that organic molecules adsorbed on metallic surfaces exhibit distinctive behaviour that alters the electronic and magnetic properties of both contributing materials [3; 16–18; 43]. Such investigations have opened exciting new frontiers to engineer the magnetism via organic molecules.

To gain a better understanding of this phenomenon, it is important to note that the molecules are characterised by discrete levels, namely molecular orbitals, unlike inorganic crystals which are formed by a continuum of states. In analogy to the valence and conduction bands in conventional semiconductors, the lowest unoccupied molecular orbital (LUMO) and the highest occupied molecular orbital (HOMO), respectively, are the orbitals involved in the charge transport in the system. When an organic molecule is brought into contact with a metal surface, it experiences two main bonding mechanisms: physisorption and chemisorption. The interactions which are associated with the physisorption mechanism are characterised by weak adsorption energy ≤ 0.1 V and a molecule-surface distance that is typically ≥ 3 Å. However, the adsorption energy associated with the chemisorption interaction is large ≥ 0.5 V, and the molecule-surface distance is ≤ 2.5 Å. These interactions influence the orbitals of the molecule and the surface of the metal and hence lead to a change in the electronic and magnetic properties of the molecule and the metal surface at the interface. The physisorption interaction is characterised by weak van der Waals interactions [44] that cause a broadening of the molecular electronic levels due to their proximity to the metallic states. Also, the surface-molecule interaction leads to rearrangement of the electron density and modifies the alignment of the molecular orbitals close to Fermi level [2; 45; 46]. In contrast to physisorption, the chemisorption interaction between the molecule and the metal leads to the formation of a new quantum mechanical system. This is due to strong charge transfer and hybridisation between the molecular orbitals (π-orbitals) and the metallic states (d-states), namely π-d hybrid interfacial states. The hybrid states have mixed molecule-metal characteristics that may turn out to be very different from the isolated molecule or metal (i.e. chemical, electronic and magnetic), an approach that has been coined “spinterface” physics by S. Sanvito [15].

The metallo-molecular interface plays an important role in altering the magnetic properties of both the metallic surface and the molecule. To better understand the interfacial effects in emerging new magnetic characteristics, it is important to consider the DOS of both the organic molecule and the metal surface. The metallic surface considered here is a ferromagnet as an example. As illustrated in figure 2.2, the electronic structure of ferromagnetic metals is defined by a broad DOS which splits into majority and minority sub-bands corresponding to spin-up and spin down electrons respectively. On the other hand, the DOS of the organic molecule is made up of discrete molecular energy levels: the LUMO and the HOMO; however, only the changes in the LUMO are represented here for simplicity. If the ferromagnetic metal and the organic molecule are well separated and there is no interaction at the interface then the electronic structure is a superposition of the individual DOS of the two spin components. However, when the molecule is brought closer to the metal and progressively into contact with it, the DOS gets altered in two ways. Firstly, the molecular orbitals become finite and electrons can leak in and out of the molecule and lead to a broadening of the DOS. The broadening depends on the interaction at the interface where the proximity and the symmetry of the molecule have a direct effect on the degree of interaction. Furthermore, the molecular orbitals for up and down spin electrons are broadened by different amounts due to an imbalance in energy for the up and down spins in the ferromagnetic material. Secondly, the molecular energy levels can be shifted from their initial position in an isolated molecule and this can be spin dependent. Due to this shift, a particular spin polarised molecular orbital can align with the E_F; for instance, the majority component presented in figure 2.2. This broadening and shift induces a spin polarisation on the molecular layer and therefore alters the magnetic properties of both elements at the interface [15].

The manifestation of hybrid interfacial states has built new functionalities in the field of organic spintronics that cannot be obtained with conventional inorganic materials. In the very recent years, several studies have developed towards understanding the fundamental phenomena of the hybrid interfaces, on magnetic surfaces, with unique electronic and magnetic characteristic in order to construct spin-functional devices. Cespedes et al. [20] pioneered to present evidence for contact-induced magnetism at the interface between carbon nanotubes and a ferromagnet. Barraud et al. [22] has

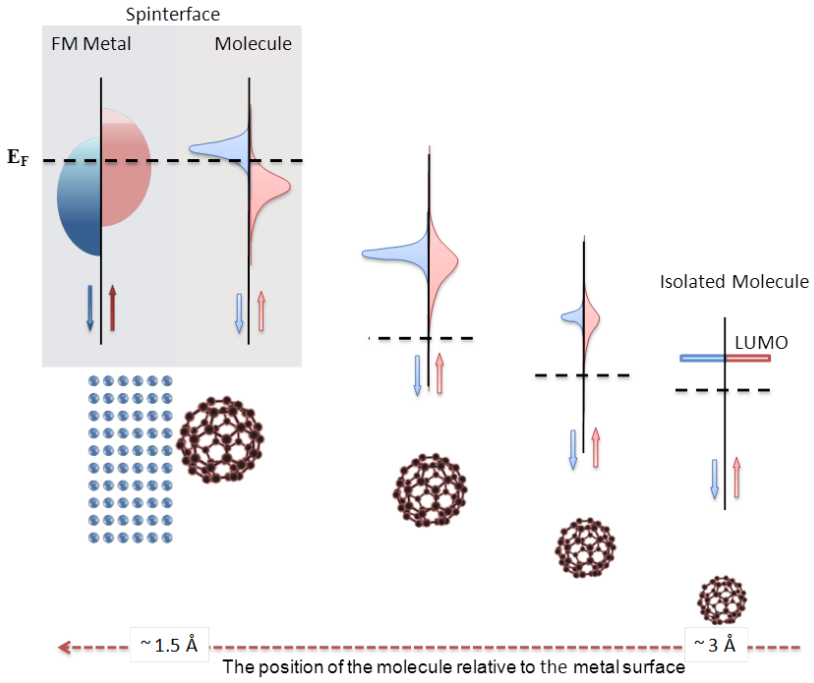

Figure 2.2: *Schematic representation of the molecular hybridisation with a ferromagnetic metal (FM). The bottom representation is for the molecule (C_{60} in this case) when it gets closer to the metal surface The top representation is for the DOS of both the FM (far left) and the isolated molecule (far right); the molecule has discrete levels whereas the FM is characterised with a band structure. The DOS of the isolated molecule changes as it is progressively coupled to the FM metal where the chemisorption and physisorption interactions become stronger. Moving from right to left towards the FM metal, the initial discrete molecular orbitals broaden and shift their position to the Fermi level E_F of the FM. Figure reproduced from [15]*

related this phenomenon to the nature of the chemical bonds (hybridisation) between the organic molecules and magnetic surfaces at the interface. Steil and colleagues [47] have also made a significant step in this field by investigating the mechanism of the charge carrier transfer process across the ferromagnetic metal/organic interface. They successfully accessed the dynamics of the hybrid interface via pump-probe photoemission experiments and elucidated the role of hybrid states for efficient spin filtering properties. Theoretical work has also played an important part in understanding the spinterface. First principle calculations have been used by several groups to study the hybridization between the organic molecules and ferromagnetic electrodes on the spin

injection process [48; 49]. They demonstrated the changes in the electronic structure of the molecules associated with the interaction at metal-molecule interfaces. They also proved that the spin can be manipulated in organic molecules with a gate potential.

2.3.2 Organic semiconductors

The route of molecular magnetism described in the above section has established remarkable progress in the field of organic, or molecular spintronics. Recently, the use of organic materials has gathered much attention for advanced spintronics applications. This is partly owing to their low-weight, small cost of processing and mechanical flexibility. Organic materials have been implemented successfully in magnetic tunnel junctions and significant magnetoresistance (MR) values have been obtained, due their long spin lifetimes, at both low and room temperatures [22; 50–52].

OSCs are characterised by strong intramolecular covalent carbon-carbon bonding whereas the interaction between molecules is dominated by weak Van der Waals forces. Carbon has six electrons: two core electrons and four valence electrons in the configuration $1s^2$, $2s^2$ and $2p^2$. Upon formation of molecules and to lower the total energy in the system, s and p orbitals in the valence orbitals rearrange and form sp^2 or (sp^3)-hybrid orbitals, which determines the properties of OSCs. The hybridisation between the carbon atoms in the molecules leads to the formation of π-bonds, which are formed by the lateral overlap (side-to-side) of p orbitals along a plane perpendicular to the inter-nuclear axis. The electrons in the π-bonds are delocalized over the single molecule. Owing to this delocalization, electron transport takes place via interactions between the π-orbitals of adjacent molecules. Between adjacent carbon atoms, strong covalent σ-bonds are formed with the hybrid orbitals by the overlap of molecular orbitals along the inter-nuclear axis. However, the σ-bonds are localised and do not contribute to the electron transport.

The buckminsterfullerene C_{60} is a carbon-based OSC, the first fullerene discovered by Kroto et al. in 1985 [53]. C_{60} has gathered much attention for advanced molecular spintronic devices. This is because C_{60} molecules are very robust and easily form

high-quality films via thermal sublimation without being damaged by depositing metals on top [53; 54]. The LUMO levels of C_{60} are well matched with the Fermi levels of common ferromagnetic materials, thus allowing relatively easy spin injection compared to other organic materials [28; 55]. Consequently, C_{60} has been introduced as the spacer layer in spin valve devices and significant magnetoresistance (MR) values have been obtained at both low and room temperatures in barriers up to 100 nm thick [50–52; 54; 56]. Changes in the exchange bias and coercivity of spin valves grown on C_{60} have also been observed [19; 57].

C_{60} is a close spherical cage molecule made up of 20 hexagonal and 12 pentagonal faces. Crystalline C_{60} possesses a face-centred cubic (fcc) crystal structure at room temperature and the molecules are orientationally disordered. Below 260 K, C_{60} undergoes first order structural transition to simple cubic (s.c) structure and the freely rotating molecules of solid C_{60} are orientationally frozen below 90 K [58].

C_{60} is diamagnetic in nature. It sets up an induced magnetic dipole that opposes the externally applied magnetic field. It has pronounced characteristics of high electron affinity values [26; 27] and low LUMO [28; 29] which give rise to charge transfer strong enough to prompt a high spin state. The latter takes place together with hybridisation effects and plays a role in the design of magnetic materials consisting of non-magnetic elements in this research.

2.4 Spin dependent scattering

2.4.1 Kondo effect

The Kondo effect is a scattering mechanism that arises from the interactions between magnetic atoms and the conduction electrons in a non-magnetic metal. The magnetic atoms (or magnetic impurities as they are often described when discussing the Kondo effect) have intrinsic angular momentum or "spin" which leads to different interactions with the conduction electrons compared with non-magnetic atoms. In pure metals, the electrical resistance decreases as the temperature is lowered because the lattice

vibrations (phonons) become small (i.e. frozen out) and the electrons can travel easily without getting scattered by phonons. However, the presence of magnetic atoms gives rise to a minimum resistance at a certain temperature, known as the Kondo temperature T_K, below which the electrical resistance increases logarithmically with decreasing temperature. Such behaviour was explained by Japanese theorist Jun Kondo in 1964 [59]. The electrical resistance R arising from the magnetic atoms is calculated based on the scattering matrix of conduction electrons by the localised spin which has two possible probabilities either spin-conserving or the spin-fliping and given by

$$R = R_B \left(1 + 2\frac{J\rho}{N} log\frac{kT}{x}\right) \tag{2.9}$$

where R_B is the resistance per impurity atom. N and ρ are the number of the conduction electrons and the DOS within energy interval x, respectively. k is Boltzmann's constant and T is the temperature. J is the exchange interaction between the conduction electrons and the magnetic atoms. It carries two possible interactions that can be either positive or negative. The former indicates a parallel alignment of the magnetic moment of conduction electrons with the impurity magnetic moment and an antiparallel alignment is associated with the latter. The negative exchange interaction is responsible for the extra scattering and gives rise to an increase in the resistance at low temperatures [60].

2.4.2 Weak localisation

WL is a quantum transport phenomenon that was discovered in two-dimensional metallic systems [61] and it has appeared as a reliable method for the study of transport properties of disordered conductors [62]. It results from quantum interference between diffusively scattered electron waves. Due to this quantum interference, the backscattering probability of the electron is modified constructively or destructively. Constructive interference occurs between electron waves travelling along time reversed paths. However, destructive interference takes place due to inelastic scattering (electron-electron and electron-phonon) that destroys the time reversal symmetry and causes a change in the phase of one of the interfering electron waves after a characteristic time τ_{in}. Magnetic impurities, due to the interaction of the electron with the local magnetic moment, also destroy the interference and cause a shift in the phase between the interfering

electron waves in a characteristic magnetic scattering time τ_m. A combination of the inelastic $\tau_{in}$and magnetic scattering τ_m times is described as the phase-breaking time τ_ϕ and defined as

$$\tau_\phi^{-1} = \tau_{in}^{-1} + 2\tau_m^{-1} \tag{2.10}$$

The time τ_ϕ exhibits a temperature dependence due to scattering mechanisms that behave differently as the temperature is changed. Hence WL is observed as a logarithmic increase in the resistance with decreasing the temperature.

The spin orbit interaction also takes place and plays a role in the backscattering mechanism. Hikami et al. [63] showed that the backscattering is only enhanced when $\tau_\phi(T) \ll \tau_{so}$, where τ_{so} is the time after which the electron spin undergoes the effect of spin orbit interaction and reversed its spin consequently. However, a system with strong spin orbit scattering $\tau_\phi(T) \gg \tau_{so}$ leads to destructive interference between the backscattered electron waves, and the backscattering intensity decreases accordingly. This is called the weak anti-localisation (WAL) effect which shows characteristic logarithmic temperature dependence of the resistance, where the resistance decreases with lowering the temperature opposite to the WL effect.

The effect of localisation can be seen clearly in the magnetic field dependence of the resistivity (MR). The phase difference between the interfering electron waves is modulated if it is subjected to perpendicular magnetic field. A small prependicular field breaks the interference of the wave function of an electron and can even suppress the WL effect. Furthermore, a weak magnetic field is found to have strong effects on spin orbit and spin-flip scattering times. Therefore, the MR allows the study of the different scattering mechanisms upon the WL [63]. For a two-dimensional metallic film, the conductivity (σ) in a magnetic field B due to WL is given by

$$\begin{aligned}\sigma(B) - \sigma(0) = \frac{e^2}{2\pi^2 h}\Bigg[\psi\left(\frac{1}{2}+\frac{B_0}{B}\right) ln\left(\frac{B}{B_0}\right) - \frac{3}{2}\psi\left(\frac{1}{2}+\frac{B_1(T)}{B}\right) \\ -\frac{3}{2}ln\left(\frac{B}{B_1(T)}\right) + \frac{1}{2}\psi\left(\frac{1}{2}\frac{B_\phi(T)}{B}\right) + \frac{1}{2}ln\left(\frac{B}{B_\phi(T)}\right)\end{aligned} \tag{2.11}$$

where ψ is the digamma function, and the fields B_x are defined by

$$B_0 = B_{el} + B_{so} + B_m \tag{2.12}$$

$$B_1(T) = B_{in}(T) + \frac{4}{3}B_{so} + \frac{2}{3}B_m \tag{2.13}$$

$$B_\phi(T) = B_{in}(T) + 2B_m \tag{2.14}$$

B_ϕ is the phase coherence characteristic field where the localized impurity spin field B_m and inelastic characteristic field B_m act to destroy the phase coherence. B_{so} is the spin orbit characteristic field that arises from scattering through the spin orbit interaction and B_{el} is the elastic characteristic field. Each characteristic field B_x is related to a characteristic scattering time τ_x by

$$B_x = \frac{\hbar}{4eD\tau_x} \tag{2.15}$$

D is the diffusion constant for electrons in a metal. It represents the distance that the electron can travel through a metal within a time through the relation

$$l_x = \sqrt{D\tau_x} \tag{2.16}$$

If the mean free path l_e and Fermi velocity ν_F of the metal are known, *D* can be calculated using

$$D = \frac{1}{d}\nu_F l_e \tag{2.17}$$

where *d* is the dimensionality of the metal [31]. The characteristic lengths l_x correspond to a characteristic magnetic field B_x and are deduced from the MR curves using [64]

$$l_x = \sqrt{(\hbar/4eB_x)} \tag{2.18}$$

The characteristic lengths are l_ϕ, l_{so}, and l_e. l_ϕ is the distance travelled by an electron before it loses phase coherence, l_{so} represents the electron before its spin experience the effect of the spin orbit interaction and finally l_e is the mean free path.

CHAPTER 3

Experimental methods

3.1 Introduction

In this chapter the various experimental techniques employed in this study are outlined including fabrication and characterisation techniques. Sample deposition was performed using a magnetron sputter deposition and thermal sublimation system. Characterisation of the samples can be broadly classified into: structural and surface morphology (X-ray reflectivity XRR and atomic force microscopy AFM), magnetometry (superconducting quantum interference device vibrating magnetometer SQUID) and electron transport (helium flow cryostat). Synchrotron radiation techniques such as X-ray absorption spectroscopy XAS, X-ray magnetic circular dichroism XMCD and low energy muon spin rotation and relaxation LE-μSR were also used in this study. Using synchrotron radiation techniques contributes to the understanding of magnetic systems in which magnetic information about specific elements and magnetic profile of the samples can be probed. The principles and procedure of all techniques are detailed as well as their applications to this study.

3.2 Fabrication: Sputtering deposition

Sputtering is a physical vapour deposition process that is extensively used to grow high quality thin films. A sputtering gas is ionised to form a plasma that can be accelerated towards a target electrically so that atoms are removed and diffused towards a substrate[65].

There are several sputtering methods including DC, RF and magnetron sputtering. The DC sputtering system used in this investigation consists of a pair of electrodes: cathode and anode. The cathode is biased at around -400 V and with a target material placed on the front surface. On the anode, the substrates are placed and usually grounded. The operational process of the sputter system is run under high vacuum conditions using a roughing pump and a cryo-pump with a base pressure in the main chamber of about 10^{-8} mTorr when using a liquid nitrogen trap (Meissner trap). The sputtering chamber is filled with an inert gas (typically argon), which is introduced

with a flow of 24 SCCM (standard cubic centimetres per minute) resulting in a pressure of 2-3 mbar to the evacuated chamber. Argon is ionised under the application of a DC voltage to create a plasma between the two electrodes. Then argon ions are accelerated towards the negatively biased surface of the target and material is ejected as a consequence of the collisions. Subsequently, the sputtered atoms condense on the surface of the substrate to form a thin film [66].

In magnetron sputtering, permanent magnets are placed beneath the target surface in order to confine the plasma by the Lorentz force. Figure 3.1 illustrates the operation of the DC magnetron sputtering system. The magnetic field lines form a closed loop path that acts as an electron trap around the surface of the target. The ejected electrons from the target move in cycloid orbits immediately above the target. The orbital motion of the electrons strongly increases the probability of ionization of the sputtering gas, leading to a higher deposition rate [67].

Our sputtering system consists of eight sputtering magnetrons, two for magnetic targets and six for nonmagnetic targets as well as an RF magnetron and an evaporation source. Such an arrangement allows the deposition of different materials *in-situ*, without breaking vacuum. The system is also equipped with a shutter system to perform a sequential deposition where multilayered stacks with a large number of thin layers with alternating compositions can be deposited. Care must be taken to obtain a clean deposition process with good yield of high quality films. For instance, the oxidised silicon substrates are cleaned with acetone and isopropanol in an ultrasonic bath before loading into the deposition system. Also, all targets are subjected to a pre-sputtering cleaning process for 10 to 15 minutes before deposition by energetic argon ions bombardment to remove contaminated surface layers.

C_{60} molecules are deposited *in-situ* via thermal sublimation where the base pressure in the chamber during the molecule sublimation is in the 10^{-8} mTorr range. The molecules in powder form are placed in a crucible which is resistively heated by a tungsten filament, see figure 3.2. The tungsten filament is attached to two copper rods where a high current source of approximately 20 A is fed into these copper rods. When the temperature of the crucible is high enough, the molecules are thermally sublimated

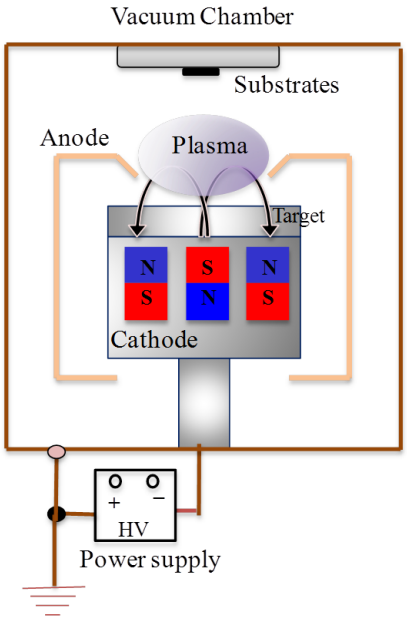

Figure 3.1: *A schematic diagram of a DC magnetron sputtering system. A DC voltage is applied between two electrodes: cathode (target) and anode (the target can or shield), after introducing argon gas to the evacuated chamber. The argon atoms are ionised due to the accelerated electrons between the electrodes resulting in purple glowing plasma. These ionised ions bombard the target and metal ions are ejected from the surface and consequently deposit on the substrate. The presence of permanent magnets beneath the sputtering target traps electrons and enhances the ionization rate. The high ionization rate increases the sputtering rate.*

and deposited on the substrate surface. The C_{60} source was pre-heated prior to actual sublimation or deposition to remove the fullerene oxides and solvent impurities, and produce pure fullerene films [68]. To avoid excessive heating, the evaporation source is encased with a water-cooled system. A quartz crystal monitor is used along with the evaporation source to determine the thickness of the deposited film during the sublimation process. It operates at a natural frequency in the MHz range. This oscillating frequency changes as the mass of the deposited film on its surface varies. Electronically, the changes in frequencies are measured and converted into thickness. In order to keep accurate thickness of the deposited film, the tooling factor is calibrated by measuring the actual film thickness via X-ray reflectivity after each deposition. A schematic diagram of the evaporation source used throughout this study is illustrated in figure 3.2.

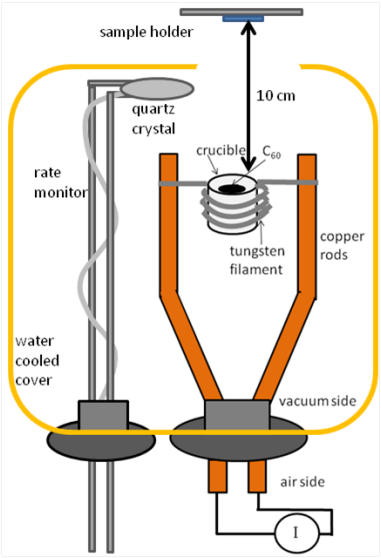

Figure 3.2: *Schematic diagram of the C_{60} evaporation source. The molecules are placed in an alumina crucible and heated via applying current of about 20 A to a tungsten filament. This lead to heat the filament to several hundred Kelvin with equivalent vapour pressure of 1.0 Pa [69]. Taken from [70].*

The thickness uniformity obtained from the vapor pressure of C_{60} is a very important parameter to consider while depositing samples. This is because properties such as thickness and roughness have an effect on the emergent magnetism of the films. The distribution of the molecules leaving the evaporation source is dependent on a number of geometric considerations, such as the source to substrate distance, which is about 10 cm, and the position of the substrate relative to the evaporation source. Since the former is immovable due to space constraints in the chamber, the alignment of the latter plays a role in the thickness uniformity in this study. Figure 3.3 shows examples of the thickness uniformity of C_{60} films where nine 8×8 mm^2 silicon substrates are distributed across the substrate plate. The thickness is not identical for all the points on the substrate plate. However, the uniformity has been improved by the use of a smaller substrate size (4×4 mm^2) and by placing it in the middle of the plate where the centre of substrate is centred over the evaporation source.

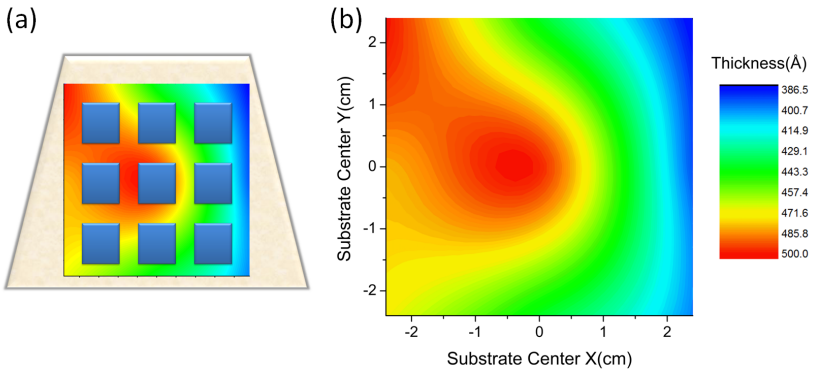

Figure 3.3: *The distribution of C_{60} thickness across the substrate plate measured by X-ray reflectivity. (a) Nine C_{60} samples placed at different positions on the sample plate. (b) C_{60} thickness map for the samples as pictured in (a). There are fluctuations in the position of the evaporated plume of fullerene which causes the deposition of layers with varying thickness and roughness.*

The samples were grown on 4×4 mm^2 Si/SiO_2 substrates. They have a typical multilayered structure of Ta (5 nm)/ [C_{60}(20 nm)/ Metal (***t*** nm)]×***N***/ Al(5 nm), from bottom to top, see figure 3.4. The thickness of the metallic layer ***t*** and the number of repeats ***N*** are varied based on the properties to be studied. To reduce the oxidation of the samples in ambient air, the complete stack was capped with a 5 nm Al layer. Ta is used as a seed layer to provide a smooth interface with C_{60} due to the small grain size that Ta has which promotes a smoother surface to the toplying layer. For control samples, an insulating layer of Al_2O_3 is introduced as a spacer layer to break any contact between C_{60} and the studied material. The spacer layer is deposited by sputtering a thin layer of Al, then oxidizing it in a plasma containing Ar and O_2, a process called plasma oxidation. The flow rate of both argon and oxygen are 16 SCCM and 76 SCCM respectively, equivalent to pressure of 1.6 mTorr and 6 mTorr. The entire process in the sputtering system is programmed so that multilayer deposition, oxidation steps and evaporation process are performed automatically.

The interfacial morphology of the deposited multilayers was studied by cross-section transmission electron microscopy (TEM). It revealed that the metallic layers are continuous and there is no inter-diffusion between the organic and the metal. This

provides evidence of the high quality of the deposited films from our system.

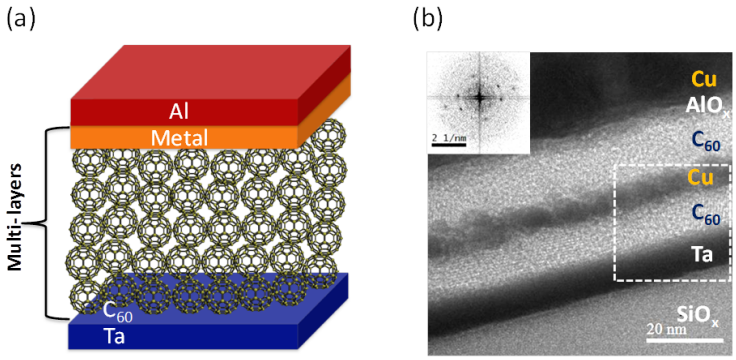

Figure 3.4: *(a) Schematic representation of the sample structure used in this study where Ta is used as a seed layer to provide smooth interfaces with C_{60} and Al as a capping to prevent oxidation. Depending on the study, the metallic layer is varied along with number of repeats. (b) Cross-sectional TEM images of a Si/SiO_2/Ta/C_{60}/Cu/C_{60}/Al/Cu stack reveals no significant inter-diffusion between the layers. Inset: fast Fourier transform of the region indicated by the dotted box shows the presence of sharp spots in the diffraction pattern due to the crystallinity of the C_{60} layer. (b) is taken from [71].*

3.3 Structural and surface morphology characterisation

3.3.1 X-ray reflectivity

XRR is a non-destructive technique used for characterisation of thin films. It depends on the interaction of reflection and refraction of electromagnetic waves at interfaces between different media with different index of refraction. The technique is performed simply by measuring the specularly reflected X-ray intensity as a function of grazing incidence angle. Analysis of the reflected intensity provides information about density, roughness and thickness for both thin films and multilayer samples. To describe such refractive phenomena, the interface between vacuum and the medium of interest is taken to be homogeneous with sharp boundaries. For X-rays, the index of refraction

for materials is less than unity

$$n = 1 - \delta, \tag{3.1}$$

δ is of order 10^{-5} and can be expressed as

$$\delta = \frac{2\pi\rho r_0}{k^2}, \tag{3.2}$$

where ρ is the electron density and r_0 is the Bohr radius. k is the wave vector of the radiation.

The relation between the angle of incidence θ and the angle of refraction $\theta^{'}$can be deduced from Snell's law δ is very small and Snell's law is expressed as

$$\cos\theta = n\cos\theta^{'}, \tag{3.3}$$

X-rays undergo total external reflection from solid surfaces at incident angles below the critical angle θ_c. This critical angle can be derived by setting $\theta^{'} = \theta_c$ and expanding the cosine in Snell's law to give

$$\theta_c = \sqrt{2\delta} = \sqrt{\frac{4\pi\rho r_0}{k^2}}, \tag{3.4}$$

which gives information about the electron density, ρ, of the reflecting medium [72–74].

Exceeding the critical angle causes the X-rays to enter the film and reflect from the top and bottom interfaces. Multiple reflections can occur within the film and give rise to interference fringes, see figure 3.5. The period of the interference fringes in the reflected intensity are known as Kiessig fringes [75]. The peaks and dips in the oscillations correspond to the wave scattering in phase and out of phase, respectively. The decay rate of oscillations provides information of roughness whereas the angular positions of the oscillations provide information about the thickness of the film. The surface roughness causes the reflectivity to fall off more rapidly assuming the scattering from a rough interface is weak and the multiple reflections may be neglected [73]. On the other hand, the thickness of the sample *t* can be deduced by analyzing the angular distribution of the resulting interference pattern using the Kiessig equation:

$$\lambda = 2t\sqrt{\sin^2\theta_n - \sin^2\theta_c}, \tag{3.5}$$

where n is an integer, λ is the wavelength and θ_n is the angular position of constructive peaks [76; 77]. Figure 3.5a shows a typical example of scattering from a single thin film sample. Throughout this work, Cu Kα X-rays are generated from a copper target with a characteristic wavelength of 1.54 Å using Bruker D8 discover system.

In this study, the thickness of the metallic layer plays a significant role in the magnetic properties and strongly affects the magnetisation. Depositing these materials with acceptable precision in thickness is difficult when layers become very thin, for instance as thin as 1 nm. This is because a few seconds difference in the deposition time due to the movement of the substrate to/from the target could lead to a difference in thickness of a few nanometres. To obtain reliable data for the thickness, calibration samples were grown in a superlattice periodic structure by depositing one material on top of another in a repetitive sequence with layer thickness similar to the intended samples. The period and the thickness of the superlattice are determined from the angular positions of the peaks utilising Bragg's law [78] as illustrated in figure 3.5b. The X-ray reflectivity data of a superlattice structure was fitted with Bede software package where individual layer thicknesses, roughnesses and densities of the layers can be extracted from the fit [79].

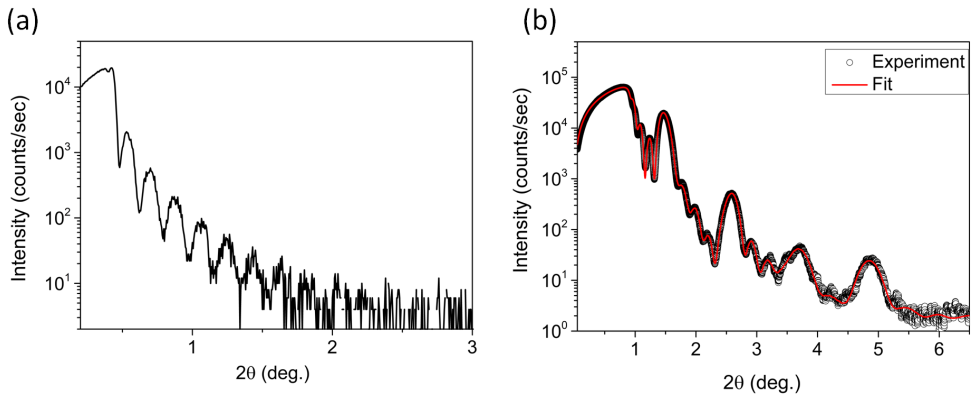

Figure 3.5: *X-ray reflectivity measurements of (a) a single film of C_{60} (43±2 nm) and (b) a multilayer stack of [Ta(4.49± 0.07nm)/Cu(2.8±0.1 nm)]×5. The thickness of (a) was determined by the Kiessig equation 3.5 whereas the thickness of (b) was obtained using the Bede fitting software as presented by the solid red line.*

3.3.2 Atomic force microscopy

AFM is a scanning probe microscope technique which can be utilised to investigate the properties of surfaces with sub nanometre resolution. AFM relies on scanning a very sharp tip over the sample surface using interaction forces between the tip and the surface. The significant interaction forces between the tip and sample is a combination of long-range attractive van der Waals forces and short- range repulsive Coulomb interaction [80]. The tip, in the AFM configuration, is mounted on the free end of a micro-machined cantilever and the other end is attached to a piezoelectric (PZT) actuator, as depicted in figure 3.6. The PZT actuator is controlled by feedback mechanisms that keep the tip at a constant force, or constant height above the sample surface depending on the adopted imaging mode. In this research 'tapping mode' AFM was used where the friction and adhesion are reduced, hence the surface damage to the sample is minimised. In tapping mode, the cantilever is driven by a force F_o to oscillate at or close to its natural resonance frequency ω_o using the PZT actuator, while the tip-sample interactions are kept to a minimal amount of time t. The PZT actuator applies a force on the cantilever base in order to maintain the vibrations of the cantilever tip at fixed amplitude through a feedback loop. The motion of the tip-cantilever can be described as differential equation of the second order

$$m\frac{d^2z}{dt^2} + kz + \frac{m\omega_o}{Q}\frac{dz}{dt} = F_{ts} + F_o\cos(\omega t) \tag{3.6}$$

where z is the transverse displacement of the cantilever. k,Q and ω are the force constant of the free cantilever, the quality factor and angular frequency of the driving force, respectively. F_{ts} represents the tip-surface interaction forces. In the absence of tip-surface forces, it describes the motion of a forced harmonic oscillator with damping. The steady state solution to the differential equation is sinusoidal and given by

$$z(z_c, t) = z_o(z_c) + A(z_c)\cos(\omega t - \phi(z_c)) \tag{3.7}$$

where z_o, A and ϕ are the mean deflection, amplitude and phase shift of the oscillation, and z_c is the distance between the tip and the sample surface [81; 82]. When the vibrating tip passes over the surface in a raster pattern, its vibration amplitude changes according to the surface topography of the sample. An optical system is used to detect the change in oscillation amplitude. This system consists of a laser beam impinged

at the cantilever and a split photodiode which detects the deflected beam and records the signal according to the change in the oscillations. The feedback generates an error signal as a difference between the measured values with the set reference value. This signal controls the PZT that adjusts the tip–sample separation to maintain constant amplitude during the scanning motion. The surface topography of the sample, in this situation, is mapped by recording the error signal as a function of the lateral position of the tip [80]. In this way, the detected error signal is used to extract the root mean square (RMS) roughness as a measure of the surface roughness of the sample. *Gwyddion* software is applied to the mapped image obtained from AFM to quantitatively analyse the surface roughness [83]. AFM images were taken using Bruker multimode 8 instrument with electronics controlled by Nanoscope 5 technology. Silicon tips were used (Bruker TESP Probes) with nominal radius of 8 nm, spring constant of the cantilever 42 Nm^{-1} and resonant frequency of 300 kHz.

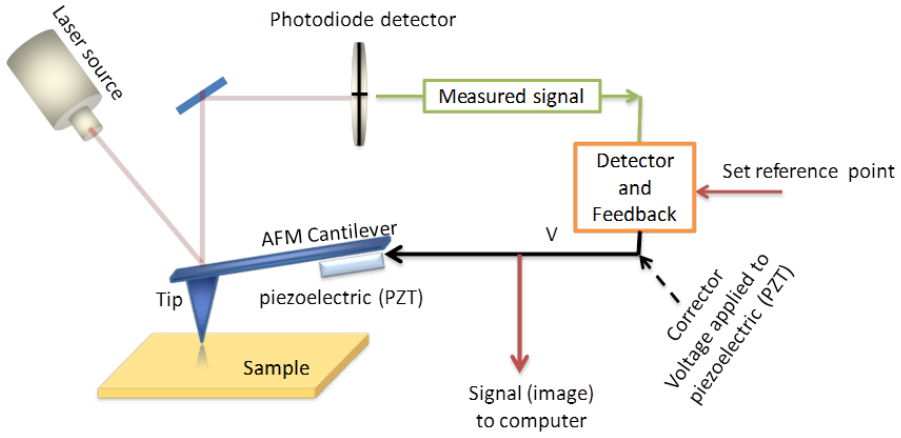

Figure 3.6: *Schematic representation of atomic force microscopy (AFM). It works in tapping mode using cantilever-tip ensemble at a fixed frequency. The reflected laser signal from the optical system to the feedback circuit gives information about sample topography.*

3.4 Magnetic characterisation

3.4.1 Magnetometry

A vibrating sample magnetometer (VSM), is an instrument that is used to measure the magnetic moment of a sample with very high precision. It is based upon Faraday's law where a magnetic field produced by an oscillating magnetized sample produces a changing magnetic flux in the detection coils. In a VSM, a sample is attached to the end of a sample rod and usually positioned at the vertical centre in the gap between two pole magnets. The basic measurement is accomplished by oscillating the magnetised sample at a certain frequency near a pair of oppositely wound pickup coils. The vibrating sample induces a signal in the pick up coils based on Faraday's law. The induced voltage is synchronously amplified and lock-in detected the signal in the VSM detection module [84].

In this study, Quantum Design SQUID-VSM system has been used to investigate the magnetic properties of the samples. The SQUID sensitivity is about 10^{-8} emu which is better than the a typical VSM sensitivity of 10^{-6} emu; as the studied samples have moments of the oder of 0.1 to 10 μemu. The SQUID magnetometer can operate over a broad range of temperatures (1.8 K to 1000 K) and magnetic fields up to 7 T. The extremely sensitive magnetic measurements are performed through a system of superconducting detection coils inductively coupled to a superconducting loop with two Josephson junctions. The detection coils are configured as a second order axial gradiometer to minimize signals caused by fluctuations in the applied field of the superconducting magnet. This configuration consists of two symmetrical end coils connected in series with a central coil wound in opposition as shown in figure 3.7. The coils assembly is positioned at the centre of the uniform field region of a superconducting coil. A SQUID measurement is performed by vibrating a sample that is mounted on a nonmagnetic rod through the superconducting detection coils. As the magnetized sample vibrates through the coils, it produces a change in flux in the detection coils.

In the absence of any external magnetic field, the input current splits equally through the Josephson junctions. However, when a small external magnetic field is applied, a

screening current I_s begins circulating in the superconducting loop and generates a magnetic field that cancels the applied net flux. The screening current increases as the magnetic flux is increased and the junctions become momentarily resistive when the magnetic flux reaches half a quantum. The screening current changes sign when the applied flux reaches half of a flux quantum and goes to zero at one flux quantum. The variations of the current in the detection coils, corresponds to the change in magnetic flux and produces a DC output voltage which is proportional to the magnetic moment of the sample. The SQUID feedback circuit is used as a null detector so no current flows in the detection coil except the induced current due to a change in flux in them [85; 86]. In this system, the most notable features of magnetic materials have been measured. For instance, hysteresis loops have been obtained by successively measuring magnetic moments at various field values. Magnetisation curves have been measured as a function of temperature. These measurements have been done taking into account the contribution from the substrate and the sample holder.

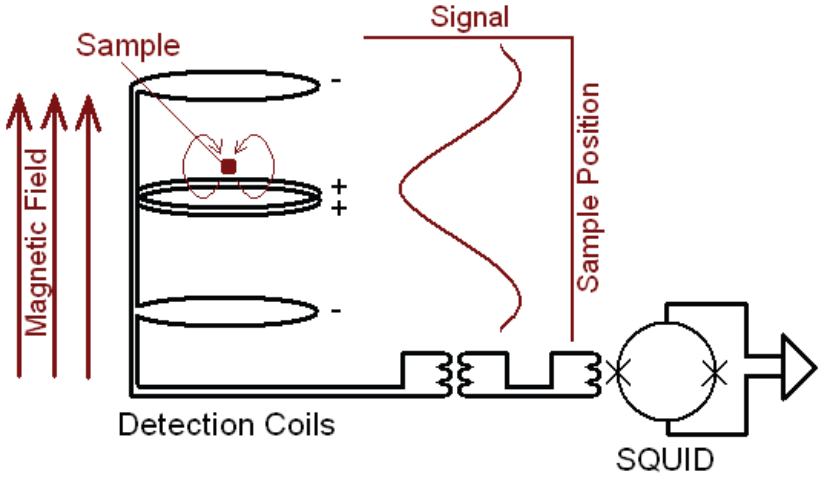

Figure 3.7: *The configuration of a magnetometer with superconducting detection coils connected to an input coil of inductance that is coupled in turn to the DC SQUID [87].*

3.5 Synchrotron radiation techniques

Synchrotron facilities use electromagnetic radiation emitted when charged particles are accelerated along a curved trajectory. The synchrotron radiation techniques are powerful tools for the fundamental understanding of magnetic state of matter. In this work, various synchrotron radiation techniques were used such as XAS, XMCD and LE-μSR. The first two techniques are inherently element selective, which allows disentangling of the various contributions of magnetic properties from different elements in a sample. The XAS and XMCD experiments were carried out at the Brookhaven National Laboratory using the U4B beamline on the now decommissioned NSLS synchrotron and the ALBA Synchrotron light source in Barcelona. A LE-μSR technique provides a unique quantum probe of local magnetic moment distributions in matter. This experiment was performed at the Swiss Muon Source SμS at the Paul Scherrer Institut (PSI).

3.5.1 Low energy muon spin rotation spectroscopy

Muons (μ) are elementary particles used extensively in materials research and condensed matter science as a microscopic magnetic probe to investigate the local magnetic field in a wide range of materials [88; 89]. Muons originate from the decay of pions, which are created by accelerating a high-energy proton beam (500 MeV – 1 GeV) into a nucleus of a light atom target such as carbon. These charged pions (π^+) go through a rapid decay within 26 ns into a muon and a neutrino. The important consequence of such two-body decay is that the muon and the neutrino are emitted in opposite directions due to conservation of momentum. The neutrino has a spin antiparallel to its momentum, and this implies that the generated muon has also similar antiparallel spin-momentum alignment. This certain spin-momentum orientation of muon will produce a beam of 100% spin polarized muons [89] .

Muons are unstable particles that decay in about 2.2 μs. They carry a positive (μ^+) or negative (μ^-) charge, and spontaneously decay in a three-body process: a positron (or an electron) and a neutrino (ν_μ) anti-neutrino ($\bar{\nu_\mu}$) pair as follows:

$$\mu^{+(-)} = e^{+(-)} + \nu_\mu + \bar{\nu_\mu} \tag{3.8}$$

Negative muons carry the same elementary charge as electrons with a spin of 1/2 but their mass is about 207 times larger than that of an electron. The muon has a corresponding antiparticle with a positive charge (μ^+) but equal mass and spin. In comparison to protons, muons have a mass of one ninth of the proton mass and approximately 3.2 times larger magnetic moment than that of the proton. The magnetic moment associated with the spin allows muon to interact with a magnetic field which makes muon a sensitive magnetic nanoprobe when implanted in matter. It gives a significant advantage in studying a variety of static and dynamic phenomena in superconductivity, magnetism and many other fields, even without the application of an external magnetic field [88; 89]. However the energy of the muons that are produced from the pion decay is very high of about 4 MeV. Such energy is equivalent to an implantation depth of the order of mm, which limits the application of the muon technique to study only the bulk properties and no depth profile can be extracted in this case.

To be able to use muon technique for thin films and multilayers and perform depth dependent studies, the energy of muons needs to be low ($\sim$ keV) and tuneable. To generate a sufficient amount of low energy muon particles, a moderation method is used at PSI. The experiment starts when an intense muon beam with energy $\sim$ 4 MeV is incident at a rate of 1.7×10^8 μ^+/s onto a cryogenic moderator in an ultra high vacuum (UHV) chamber with a base pressure of 10^{-10} mbar to obtain stable moderation efficiency. The low energy (LE) beam setup with μSR spectrometer is shown in figure 3.8. The moderator consists of a thin silver substrate (125 μm) which is cooled by the cryostat to a base pressure of 10 K. A thin layer (200 Å) of condensed van der Waals bound argon gas is deposited on the cold silver substrate. This layer is protected by depositing a 12 Å layer of solid nitrogen on top of it. A portion of the intense beam is decelerated from its initial energy of 4 MeV to about 15 eV when it hits the moderator. The muons emerging from the moderator pass through an electrostatic transport system consisting of "einzel" lenses, a mirror and a conical electrode after being accelerated in a positive potential of 15 kV. The einzel lenses are used to focus the muon beam without changing the energy of the beam. The electrostatic mirror separates the low energy muons from the fast muons exiting the moderator by means of a 90° deflection. The 90° deflection at the electrostatic mirror leads to a horizontally polarised beam where the spins are oriented transversely to their motion. The lens system is used then

to focus the low energy resulting beam into the detection stage [90; 91].

The detection of the low energy muons takes place through a 10 nm carbon foil that is located midway along the beam transport system. On passing the beam, a few electrons are released at the foil and give indication of the muon implantation signal in a microchannel plate (MCP2). The final kinetic energy of the arriving muons can be implanted with the full energy range between 0.5 and 30 keV. This can be controlled by an accelerating or decelerating potential applied to the sample. The sample in the μSR experiment is mounted on a silver plate to eliminate any magnetic signal since silver has no magnetic moment and a very small nuclear moment. The sample holder is then placed on a sapphire plate on a continuous-flow helium cryostat. The polarised muons implanted on the sample decay into positrons and are detected by a set of scintillators (positron counters) [90; 91].

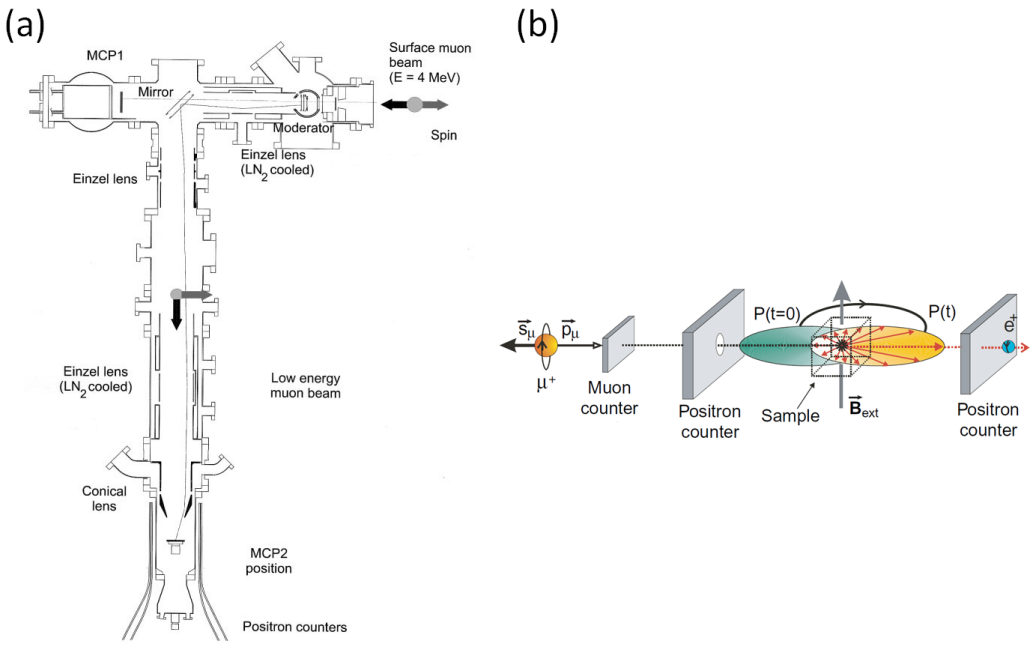

Figure 3.8: *(a) Setup of the LE- μ^+ beam at the PSI, it has about a 2.2 m total path length between the moderator and MCP2 detector. (b) Schematic diagram of the principle of a muon spin rotation and relaxation experiment in an externally applied transverse field. p_μ and s_μ represent the momentum and the spin of the muons [89].*

The measurements in this work are performed in the absence of an external magnetic field, a configuration called Zero Field-μSR. It is a very sensitive configuration that can be used to detect weak internal magnetism in the sample that occurs as a result of the ordered magnetic moments or static and dynamic random field distributions. The muon spin precesses about this internal magnetic field, with a frequency that is proportional to the size of the field. Then a positron decays from this process and emits preferentially along the muon spin direction. The distribution of the magnetic fields at the muon site is reconstructed from the time dependence of the muon spin-depolarisation function by collecting several million positrons on a timescale of up to 10 μs [90; 91]. If the implanted muons experience any magnetic field *B* not parallel to their initial polarization, they will precess with a frequency $\omega_\mu = \gamma_\mu$B, where γ_μ= 2π $\times$135.54 MHz/T is the gyromagnetic ratio for the muon. The precession will be associated with a gradual loss of polarisation. This precession appears as an oscillation in the signal of the positron detectors surrounding the sample. The amplitude of this oscillation (*A*) is the muon decay asymmetry parameter and is proportional to the polarisation of the corresponding muon state [89; 92]. The resulting asymmetry spectra are fitted with the following function:

$$A\left(t\right) = Ae^{-\lambda t} + \sum_{i=1}^{\infty} A\cos(\phi + 2\pi\nu_i t)e^{-\lambda_i t} + A_{tail}e^{-\lambda_{tail}t} \tag{3.9}$$

where ν_i representing the frequencies, ϕ is the angle of the muon spin at t = 0 with respect to the positron detector and γ is the decay constant determined by the polarisation loss mechanism. The first and last terms refer to the muons' fast and tail decays respectively. The initial (fast) decay $Ae^{-\lambda t}$ corresponds to the rapid loss of polarization at short timescales, whereas the tail component $A_{tail}e^{-\lambda_{tail}t}$ describes the eventual loss of polarization from implanted muons due to thermal relaxation processes and give indication about the dynamic of the system. The amplitude of oscillation in tail term A_{tail} is know as assymmetry tail.The μSR data analysis software package *musrfit* [93] was used to fit the data based on the equation above. This program is developed at PSI to fit muon μSR spectra for different energies.

3.5.2 X-ray absorption spectroscopy and magnetic dichroism

XAS is a synchrotron radiation technique used for determining the electronic structure of materials. It gives the capability of probing a specific element of interest within a sample without interference from other elements present in the sample. The element specificity determination is based on the transition of electrons from the core electronic states to empty energy states at specific X-ray photon energies, one of the important features of the absorbing element. XAS is not limited by the sample type; a wide variety of materials such as atoms, molecules and solid samples can be studied in different states such as powder, solid and solution [94].

When X-rays are directed onto a sample, they may be absorbed by exciting a core electron into a higher unoccupied electronic state. An electron from a higher energy state drops to fill the core gap via two relaxation processes, X-ray fluorescence and Auger emission. X-ray fluorescence process is accompanied by emission of a characteristic X-ray (fluorescence) photon with energy matches the energy gap between the upper and lower level. However, in an Auger emission, the energy liberated by a transfer of electrons to lower energy state simultaneously causes a second electron to be ejected, termed the Auger electron. Multiple subsequent decay processes are associated with this emission, leading to a cascade in which a large number of electrons are released from the sample surface. These electrons were measured by a picoammeter and collected as drain current in a total electron yield (TEY) configuration. The resulting drain current signal is proportional to the X-ray absorption intensity. At specific X-ray photon energies, the probability of the X-ray absorption increases significantly. These abrupt rises in absorption are called the absorption edges, where each edge matches the energy required to eject a core electron into higher energy levels and represents a different core-electron binding energy. The edges are named according to the principal quantum number (n) of the excited electron. For instance, the K-edge is when the transition of a core electron originates from n=1 (1s) whereas the L-edge is from n=2 (2s or 2p) electron, etc. The X-ray spectra from this experiment represent the scanned X-ray energy through the binding energy of a core shell of the targeted element that gives information about the local electronic environment.

In addition to electronic structural identification, XAS can provide element-specific magnetic information of matter if circularly polarized X-rays are used by means of XMCD. XMCD arises from the fact that the excitation of a core electron into unoccupied states is dependent on the polarization of the outer electron shell of a material (such as d band in transtion metals or p in carbon) and the helicity of the incoming photons. An XMCD spectrum is obtained from the difference in the absorption amplitude of two XAS measurements recorded with opposite circular polarised photons.

The principle of XMCD in a magnetic material can be simply described by a two-step process, as schematically shown in figure 3.9. The first step involves the transfer of angular moment from the circularly polarized light to the excited electron (photoelectron). For 3d metals as an example, the 2p core state is split into $p_{3/2}$ (L_3-edge) and $p_{1/2}$(L_2-edge) levels. The circularly polarised light transfers its angular momentum to the photoelectron. Because the latter originates from a spin-orbit split level, such as $p_{3/2}$ level, part of the transfer momentum goes to the spin via the spin-orbit coupling. Thus the excited electrons are spin polarised. The transferred momentum from the right circularly polarized photons (h^+) is opposite to those from left circularly polarized photons (h^-), so photoelectrons created in the two cases will have opposite spins. The spin polarization of the photoelectrons is also opposite at L_3-edge and L_2-edge because these levels have opposite spin-orbit coupling. In the second step, the exchange-split 3d band act as spin detector of the excited photoelectrons which will be reflected in the absorption signal. The difference in the absorption intensity for the right (h^+) and the left (h^-) circularly polarized light allows a quantitative determination of the magnetic moment [95].

In this experiment, a soft X-ray beam covering a photon energy range of about 20-1200 eV is used with an energy resolution $\Delta E/E = 10^{-3}$. Magnetic fields of up to ± 1.5 T were used to saturate the sample with respect to the incident beam. The circularly polarised beam is obtained from a bending magnet and then refined with a spherical grating monochromator before reaching the sample. The latter is attached to an aluminium holder via silver paint which provides a drain for the photoelectrons emitted during the absorption process (TEY configuration). The TEY signal is normalized to an independent gold monitor signal. All measurements are run under UHV conditions

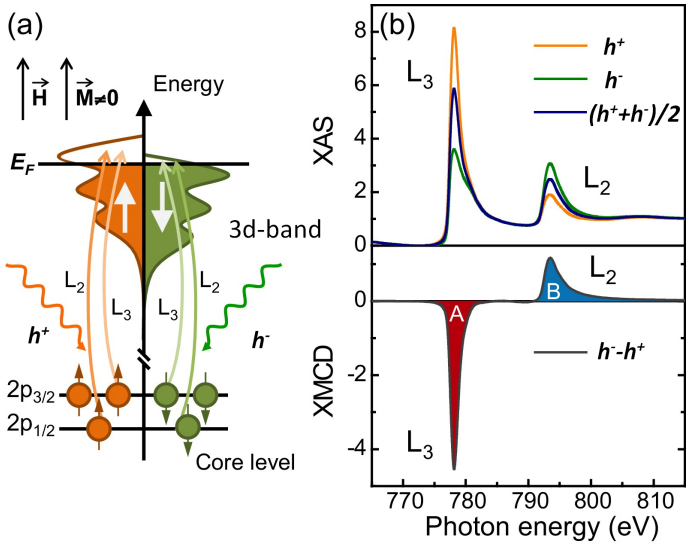

Figure 3.9: *Diagram of XMCD spectrum for L-edge absorption of a 3d transition metal. (a) The two-step model representation where the core electrons are excited by circularly polarised photons and being detected in the spin-dependent 3d band; details in the text. (b) $L_{3/2}$-edge XAS spectra obtained with right (h^+) and left (h^-) circularly polarised X-ray and the resulting dichroism signal. Figure adapted from [96].*

to prevent electron scattering.

3.6 Low temperature electron transport

Electron transport measurements were performed in an Oxford instruments helium flow cryostat equipped with a superconducting solenoid that can produce magnetic fields of up to 8 T. A variable temperature insert (VTI) immersed in a liquid helium reservoir is used to allow a continuous adjustment of sample temperature over a wide range. The helium reservoir is isolated from the ambient room temperature and surrounded by a liquid nitrogen jacket. To reduce the evaporation loss due to heat, the cryostat is double shielded by a high vacuum space between the walls and liquid nitrogen jacket. The sample temperature can be controlled over the range from 1.4 K to 300 K by balancing the helium flow via an adjustable needle valve as well as a heater and the pumping speed. Temperatures below 300 K are obtained by reducing the vapour

pressure of liquid helium in the sample space using an oil free scroll pump. The temperatures can be reduced further to 1.4 K by lowering the vapour pressure of the liquid through increasing the pumping speed [97]. The measured sample is mounted on a holder attached to the end of a wired stick sat at the lower end of the cryostat. The electrical measurements are fed through the stick to the sample in a four-point probe configuration. The current is applied into two of the probes and the voltage drop across the other probes is measured.

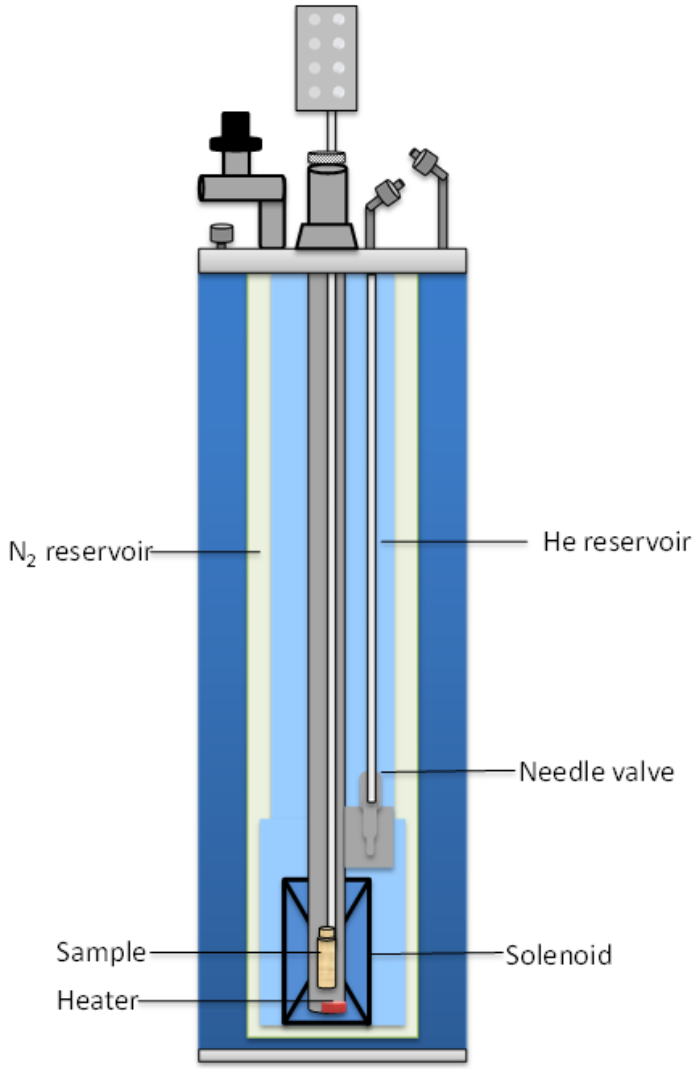

Figure 3.10: *Schematic diagram of the ^{4}He cryostat with the principal elements of the system. The system operates in a liquid helium with a superconducting magnet (solenoid) which generates magnetic fields of up to 8 T.*

CHAPTER 4

Emergent magnetism at diamagnetic metal/C_{60} interfaces

4.1 Introduction

Hybrid interfaces are formed when a molecule is brought into contact with a transition metal where hybridisation between the d orbitals of the transition metal and the π carbon electrons occurs. Also charge transfer takes place at the interface when transition metal and organic material with different individual Fermi levels are placed in contact. The hybrid states and charge transfer have shown interesting effects on electronic and magnetic properties of the interacting materials. Unexpected magnetic behaviour has been reported on molecular interactions with magnetic transition metals [3; 16–18; 20–22]. The changes in magnetic properties are due to the change in the density of states (DOS) at the Fermi energy (E_F) and/or the exchange-correlation integral. It is therefore possible to change the electronic states of non-ferromagnetic materials via molecular interfaces to closely satisfy the Stoner criterion [25].

In this study we reveal the appearance of magnetic ordering arising from interfaces between thin films of 3d non-ferromagnetic metals and fullerenes. Diamagnetic copper (Cu) and C_{60} molecules are the materials investigated in this chapter. C_{60} has good lattice match with Cu leading to up to three electrons per molecule and even, in some cases, metallisation of the interface [98]. In particular, Density Functional Theory (DFT) show that the C_{60} center can sit at an fcc site of Cu and charge transfer depends on C_{60}-adsorption geometries on Cu(111)-4x4 [71; 99]. The calculations indicate a reconstructed interface with C_{60}/7-atom vacancy on a Cu(111)-4x4 slab geometry is energetically favoured and allows more charge transfer compared to other geometries, details of calculation are shown in the supplementary information [71]. Also, the 3d bands in Cu are filled and they are close to the Fermi level [25].

The samples studied were deposited in superlattices of Cu interfaced with C_{60} molecules. By using magnetometry, low energy muon spectroscopy (LE-μSR) and X-ray absorption spectroscopy (XAS) as well as X-ray magnetic circular dichroism (XMCD), the magnetic properties of the samples were determined. Results from SQUID-VSM magnetometry have made a major contribution to this work by measuring the magnetic moment of the samples with very high sensitivity of $\lesssim 10^{-8}$ emu (typical moment of the emergent magnetism in a Cu/C_{60} sample is of the order of μemu),

see section 3.4.1 . The thickness, temperature and interfacial coupling in relation to the emergent magnetism have been studied in detail. Information from magnetometry is complemented by the use of LE-μSR. This technique is useful to determine where the emergent magnetism is localised within a sample, whereas magnetometry techniques are limited to measuring a complete sample stack. In XAS, the element specificity offers an excellent tool for identifying the sample compositions as explained in section 3.5.2. This technique is used to check for the presence of transition magnetic metals and exclude any magnetism that could arise from these elements.

4.2 Characterisation of hybrid diamagnetic metal/C_{60} interfaces

4.2.1 Magnetometry

The samples have a typical structure of Ta (5 nm)/[C_{60} (20 nm)/ Cu (t nm)]$\times$ R /Al(5 nm), with $1< t < 25$ and $1 < R < 8$; t and R represent the thickness of Cu and number of bilayer repeats respectively. Cu/C_{60} multilayers were deposited on top of a 5 nm thick layer of Ta which acts as a seed layer and provides a smooth growth of the subsequent layers. The complete stack of the samples was capped with 5 nm of Al to prevent oxidation once it is exposed to ambient air. For control samples, the spacer layer was grown by depositing a thin layer of metallic Al, then oxidising it in a plasma containing Ar/O_2 to obtain an insulating Al_2O_3 layer that breaks any electronic coupling between C_{60} and Cu. The typical sample size is 4×4 mm^2, the size required to fit the sample holder for the SQUID-VSM.

4.2.1.1 Room temperature magnetic behaviour

The magnetometry measurements of a typical multilayered system of C_{60}/Cu with structure of Ta(5)/[C_{60}(15 nm)/Cu(2 nm)]x5/Al(5 nm) show hysteresis at room temperature with a saturation magnetisation of approximately 65 emu/cc, as shown in figure 4.1. This phenomenon can be attributed to charge transfer and hybridisation between π

orbitals of C_{60} and the 3d band of Cu leading to sizeable interfacial induced magnetic moments. The strength and characteristics of the hybridisation depend on the contact geometry and electronic properties of the contact metal. These properties in turn cause a change in the electronic structure of the metal and the molecule including a change in the density of states. The latter may be observed by broadening molecular orbitals and shift towards the Fermi level in the metallic system. This leads to an induced magnetic moment in a system without ferromagnetic materials.

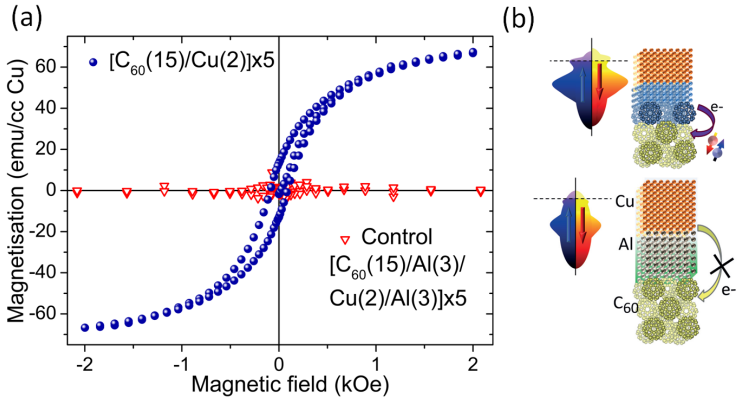

Figure 4.1: *(a) Room temperature magnetisation as a function of applied magnetic field for Ta(5)/[C_{60}(15)/Cu(2)]x5/Al(5) and Ta(5)/[C_{60}(15)/Al(3)/Cu(2)/Al(3)]x5 samples,* ***all thicknesses parenthesis are in nm****. The red symbols indicate the control structure where Al is introduced to decouple the organic from the 3d metal whereas the blue symbols indicates the system without the spacer where there is an induced magnetisation. (b) Top panel: Schematic representation of Cu to C_{60} charge transfer effect, where there is a change of density of states (DOS) and band splitting of the metallic film associated with this process. Bottom panel: Decoupling the metallo-molecular interfaces via an Al or Al_2O_3 spacer layer suppresses the effect completely and no change is observed in the metal bands [71].*

In order to eliminate charge transfer and hybridisation effects across the interfaces, a spacer layer of aluminium or aluminium oxide was included between Cu and C_{60}, separating the molecules from the 3d transition metal. The signal disappears in samples where the spacer layer is present as shown by the red symbols in figure 4.1. These experimental observations lend strong support to underline the key role played by charge transfer and hybridisation effects between the molecular p_z orbital and the 3d metal

bands in controlling the emergent spin ordering at the interfaces.

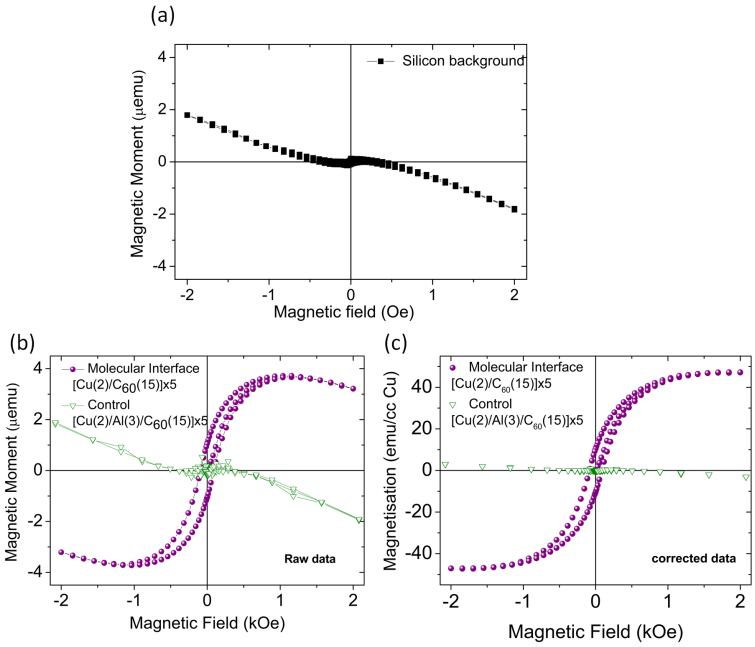

Figure 4.2: *(a) Magnetic moment as a function of the applied magnetic field of a silicon substrate and the holder at room temperature. The non-linear contribution at low fields arising from an artefact of the measurement of about 0.1-0.5 μemu. (b) Raw hysteresis M(H) loops before background subtraction for the C_{60}/Cu and Cu/Al/C_{60} samples at room temperature with an applied fields of 2.0 kOe aligned in-plane. (c) Hysteresis M(H) loops of the same sample after background subtraction at same temperature. The green symbols in both b and c show the measurements of the broken interfaces with the Al spacer. The data represented in both (a) and (b) are taken from [71].*

In magnetometry measurements, the signal for materials with low ferromagnetic moment may be dominated by the diamagnetic or paramagnetic contributions occurring from the sample holder and the substrate material. Therefore, the magnetometry results of the multi-layered systems of C_{60}/Cu have been corrected for the background signals of the sample holder and the substrate by applying a linear correction to both film and substrate data. Figure 4.2 shows the signal from (a) the substrate and holder, (b) the substrate, film and holder and (c) the magnetic signal with the background correction applied. The broken interfaces samples, with an Al spacer, and the samples

with metallic film thicknesses in the range below 1 nm and above 4 nm show very small or no magnetic signal above the background signal, as it is indicated by green symbols in figure 4.2b. However, the samples with a molecular interface and metal thickness in a particular range show magnetic signal indicated by a non-linear moment above 1 μemu.

The emergent magnetism in the C_{60}/Cu systems shows the magnetisation dependence on the thickness of the metallic layer, as apparent in figure 4.3. It shows magnetic ordering when the metallic layer is $\sim$1.5-3.5 nm thick and continuous. The maximum magnetisation is on average approximately (50$\pm$10) emu/cc which takes place when the Cu is 2 nm thick. The magnetisation quickly decays once the metallic-film is discontinuous, less than 1.5 nm. The changes in the DOS may be larger close to the interface but screened deeper within the material. As a consequence, the magnetisation drops when the metallic layer exceeds 2 nm and quenches completely if it is thick enough that the bulk properties dominate. Also, Cu has a considerably low DOS (E_F), with Stoner product one order of magnitude less than unity, that disappears as it is becomes close to bulk [25]. The measurements here show the magnetisation dependence on the thickness of the metallic layer, but not on thickness of the molecular film which is not observed to have an effect as long as the molecular film is smooth and continuous (about 10-20 nm thick).

To determine the sample anisotropy and in order to show that the magnetism is due to the interfacial effects but not due the presence of impurities in the material, the samples were measured in both in-plane and out-of-plane orientations, see figure 4.4. The samples possess anisotropy with an easy axis lies in the plane of the film, and an out-of-plane saturation field of 10-15 kOe. This gives an indication that the emergent magnetisation originates from the metallo-molecular interface but not from the magnetic impurities which are randomly distributed if present in a material (isotropically). A system that contains magnetic impurities would exhibit similar hysteresis in both in-plane and out-plane configurations which is not the case in these samples.

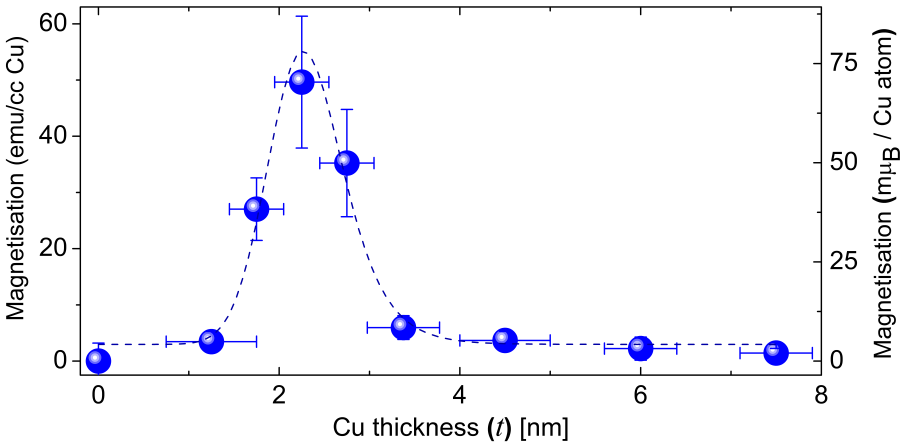

Figure 4.3: *Magnetisation dependence on thickness for Cu films with the structure Ta(5)/[C_{60}(10-20)/Cu(**t**)/C_{60}(10-20)]×(1-5)/Al(5). The results here represent the average magnetisation of 145 Cu samples. The error bars in magnetisation are calculated as the standard error of the mean whereas in thickness correspond to uncertainty in the film thickness. Dashed lines are exponentially modified Gaussian fits. The measurements were performed at room temperature and the calculations of magnetisation have been performed considering the thickness of the metallic layer only, even though the effect may extend further into the molecular layer [71].*

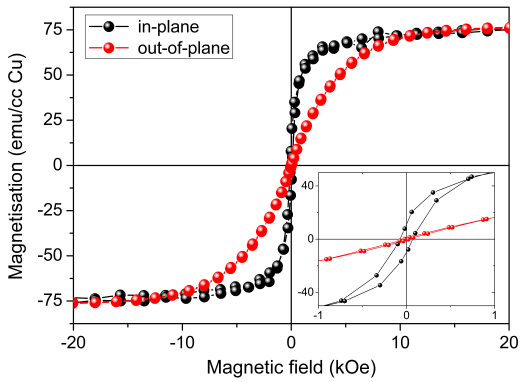

Figure 4.4: *Room temperature hysteresis loops of a C_{60}(10)/Cu(2.5)/C_{60}(10) sample measured in different magnetic field directions. Both in-plane and out-of-plane magnetisation curves have been corrected for the linear slope and normalised to the calibrated in-plane saturation magnetisation. The superconducting trapped flux of about ∼ 20 Oe shift has been subtracted from the data [71].*

4.2.1.2 Temperature dependent magnetisation

In order to understand more about interfacial effects, the magnetisation behaviour of Cu/C_{60} bilayers has been investigated in the temperature range 5- 1000 K for two different Cu layer thicknesses: 1.8 nm and 2.5 nm. The data was obtained by measuring the hysteresis loops at various temperatures in an applied magnetic field (H) of 3 kOe to ensure that the sample was saturated. The saturation magnetisation for both samples is given as a function of temperature as presented in figure 4.5. The samples show a significant decrease in magnetisation with increasing temperature. The reduction in magnetisation with temperature is typical for the thermal behaviour of an ordered magnetic system, and it is believed to arise mainly due to the spin wave (magnon) fluctuations.

The data are fitted using the Bloch $T^{3/2}$ law, which describes the temperature dependence of magnetisation of magnetic materials [100]. The magnetisation as a function of temperature is given by

$$M\left(T\right) = M_0 \left[1 - \left(\frac{T}{T_C}\right)^{\frac{3}{2}}\right]^{\beta}, \tag{4.1}$$

where M_0 is the spontaneous magnetisation at absolute zero, T_C is the Curie temperature and β is a critical exponent [100]. The fitting to the $T^{3/2}$ law provides spontaneous magnetisation and Curie temperature of (121$\pm$20) emu/cc and (814$\pm$20) K, respectively, for 1.8 nm Cu layer. Similar behaviour is observed in 2.5 nm of Cu but with 15% increase in magnetisation and 5% higher T_C. The Curie temperature of the C_{60}/Cu lies within the range of T_C of transition ferromagnets whereas the magnetic moments is less by one to two orders of magnitude.

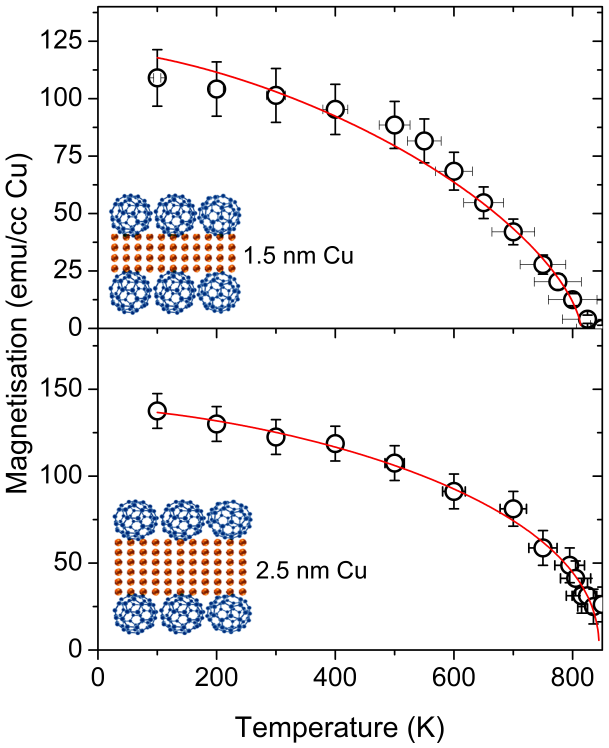

Figure 4.5: *The variation of saturation magnetisation with temperature for Ta(5)/C_{60}(10)/Cu(x)/C_{60}(10)/Al(2) with x equal to (a) 1.8 nm thick layer (b) 2.5 nm layer. Each data point presented in the figure is extracted from hysteresis loops at different temperatures. The red line is the fit to the $T^{3/2}$ Bloch law.*

.

4.2.1.3 Dependence of magnetisation on interfacial coupling

In order to explore the influence of interfacial coupling on the magnetisation, a similar set of multilayered samples of C_{60}/Cu were deposited where the thickness of Cu (2.5 nm) and C_{60} (15 nm) were kept constant while the number of interfaces (layers) was increased. The results show proportionality between the magnetic moment and the number of interfaces, as shown in figure 4.6a. To confirm that the moment originates from magnetic interfaces and is not simply proportional to the amount of deposited material, another set of samples were deposited where the total thickness of the multilayered stack was kept constant but divided into different numbers of repeats. In these samples, the total thickness of C_{60} is 81 nm and Cu is 9 nm. Similar to the first set of samples, the magnetisation also increases with the number of interfaces; for instance, the magnetic moment of [C_{60}(20 nm)/Cu(2.25 nm)]$\times$4 is larger than that of [C_{60}(27 nm)/Cu(3 nm)]$\times$3. This proportionality is limited by the thickness and continuity of the metallic layer and is in good agreement with the magnetisation dependence on the thickness as discussed in section 4.2.1.1. For example, the magnetisation decreases by splitting the sample into eight layers where the Cu film is discontinuous. Similarly, the magnetisation is lower for the multilayered samples with the number of repeats ≤ 2 where the Cu film is thick and has properties closer to bulk Cu. Here, the observation of the dependence of magnetisation on the thickness and number of interfaces excludes any contribution from contaminants but highlights the essential role of interfacial coupling on the magnetic properties.

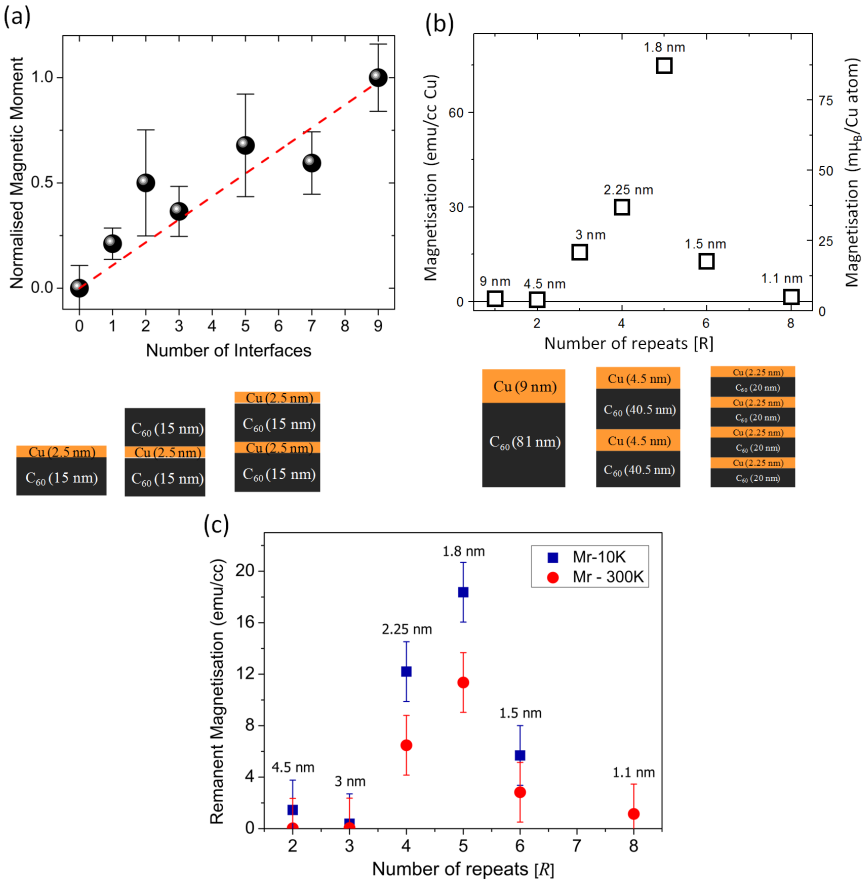

Figure 4.6: *(a) The magnetic moment versus the number of interfaces for [C_{60}(15)/Cu(2.5)]. Both Cu and C_{60} thicknesses are constant and by increasing the number of layers, the number of Cu and C_{60} interfaces are increased. The samples have from one interface, a bilayer repeat [C_{60}(15)/Cu(2.5)] to 9 interfaces [C_{60}(15)/Cu(2.5)]×5 which is equivalent to 5 bilayer repeats. (b) The dependence of magnetisation on the number of interfaces keeping the total amount of material in the samples constant and dividing them into different numbers of layers. The total thickness in the samples here is 90 nm, where 9 nm is contributed to the total thickness of Cu and 81 nm to C_{60}. The samples have from one bilayer repeat sample (R=1) of [C_{60}(81)/Cu(9)] to a sample with eight repeats (R=8) of [C_{60}(10)/Cu(1.1)]×8. The illustrations at the bottom of (a) and (b) represent the sample structures. (c) Remanent magnetisation extracted from the same samples presented in (b) [71]. (b)+(c) data in collaboration with Will Deacon.*

4.2.1.4 Interfaces quality and reproducibility

Sample degradation has a detrimental effect to organic materials which can hinder the quality of samples and change various properties such as the emergent magnetism. However, it is shown by our experiment that it can be controlled which can even be beneficial to protecting the emergent magnetisation. Increasing the number of interfaces slows down the loss of magnetisation due to the degradation process. Degradation of 40% in the magnetic moment is observed for single interface samples over 3 days, yet no degradation is observed for samples with fifteen interfaces over the same period. In a period of 10 days, samples with more interfaces showed a more gradual loss of moment comparing to the samples with less number of interfaces. This data suggests that the bottom interfaces (those closer to the substrate), are protected from degradation by the top layers, have a higher contribution for the magnetisation, figure 4.7.

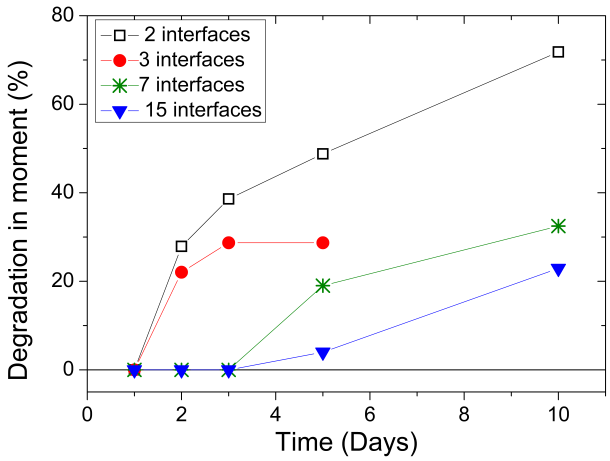

Figure 4.7: *(a) Degradation of magnetic moment as a function of number of interfaces over a period of ten days. The sample structure is Ta(5)/[C_{60}(20)/Cu(2.5)]×N/Al(5) where the number of interfaces is 2N-1 and N is the number of repeats. The lines are guides for the eye.*

In addition, it appears that the choice of the capping layer plays a crucial role in reducing the sample sensitivity to the oxidation process and hence impacts the degradation. For samples with a thinner cap layer, there was a significant loss in moment over a few days, again suggesting that the molecular and metallic film interfaces are

modified due to chemical degradation. Samples with a thicker protective cap layer experienced the same effect but over a longer period of time. The examples in figure 4.8 illustrate this effect.

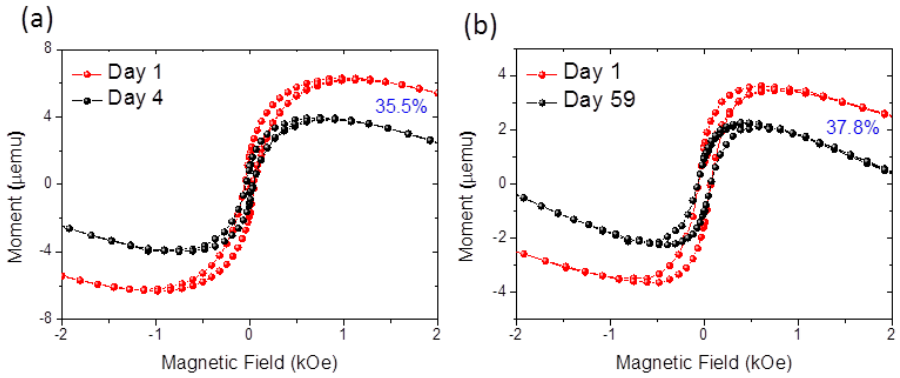

Figure 4.8: *Sample degradation using different cap thicknesses. The raw magnetic moment after different periods of time for Ta(5)/C_{60}(20)/Cu(2.5)/C_{60}(15) with (a) Au(1)/Al(3) and (b) Au (10) cap layers [71].*

Figure 4.9 demonstrates the effect of annealing on the emergent magnetisation. Annealing improves the interface morphology and crystallinity, consequently altering the magnetisation. The magnetisation of a C_{60}/Cu/C_{60} sample was measured at 300 K. The sample was then annealed by heating it to 825 K under 50 mTorr in He atmosphere in a SQUID magnetometer. The magnetisation of the sample was measured again at 300 K after annealing and compared to the non-annealed sample as illustrated in figure 4.9. The annealed sample exhibited a higher saturation magnetisation and coercive field compared to the non-annealed sample. The difference may be attributed to the change in crystallinity and morphology after annealing and oxygen migration from the interface and/or metal. Hence the hybridisation and the charge transfer with the associated modification such as the change in the density of the state will be different. Heating the sample beyond the sublimation temperature of C_{60}, 850 K, causes damage to the molecular film and causes a decrease in magnetisation.

The ability to control the reproducibility of the samples and the yield is critical due to the sensitivity of organic materials to oxygen and moisture. The deposition system is

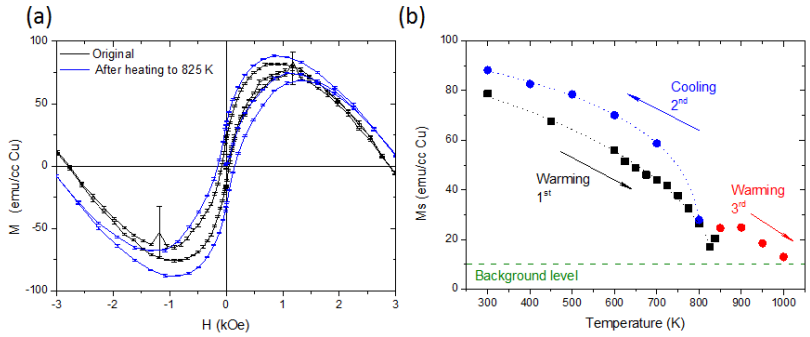

Figure 4.9: *Typical hysteresis loops of Ta(5)/C_{60}(10)/Cu(1.8)/C_{60}(10)/Al(2). Both loops represent raw data that are measured at room temperature. The blue loop is the original sample without annealing whereas the blue loop is measured after annealing the sample to 825 K. (b) The saturation magnetisation during heating and cooling process.*

adapted to improve reproducibility and yield of our samples where sixteen samples can be deposited in one growth run without breaking the vacuum with optimum pressure conditions. Table 4.1 presents results obtained in one growth run for two batches of samples: Cu and Mn samples and their controls. Mn samples will be explained in detail in the next chapter. The magnetisation exhibits consistent results in relation to the number of interfaces, which have been varied between one and two interfaces, and Cu thickness. The magnetisation for the control samples was not quenched completely because 2 nm of Al spacer layer is insufficient for this purpose. 4 nm of Al_2O_3 layer was used later to provide a proper separation between metallic-molecular interfaces, as the data in section 4.2.2.1.

AFM was used to study the roughness dependence on the number of interfaces for samples that are equivalent to the two sets of samples discussed in section 4.2.1.3, see figure 4.10. The set of samples with a constant bilayer thickness, [C_{60}(15 nm)/Cu(2.5 nm)]$\times N$, show a rise in roughness with increasing number of interfaces. However, the other set of samples with a constant total thickness, [C_{60}(81/N nm)/Cu(9/N nm)], show an opposite trend when the whole multilayered stack is split into a larger number of repeats. The roughness experienced drops as the number of interfaces increases but the thickness of Cu and C_{60} in each repeat decreases. This allows the Cu layers to work as a seed layer for the C_{60} hence the latter grows more smoothly. To confirm

Table 4.1: The saturation magnetisation and coercive field of bilayer samples of Cu/C_{60} measured at room temperature, the thicknesses in nm. The samples here were produced in one growth run. The decoupled molecular interface samples are in red. The high coercive field in the decoupled Cu/C_{60} sample could be due to constant anisotropy in the system where the reduction saturation magnetization yields high coercive field to keep constant magnetic anisotropy. Further statistics with a thick decoupled layer needs to confirm the observation.

Sample	Magnetisation (emu/cc)	Coercive field (Oe)
Cu		
Ta(5)/C_{60}(10)/Cu(1.8)/C_{60}(5)/Al(2)	71	78
Ta(5)/C_{60}(10)/Cu(1.8)/C_{60}(10)/Al(2)	52	72
Ta(5)/C_{60}(10)/Cu(2.5)/C_{60}(10)/Al(2)	58	126
Ta(5)/C_{60}(10)/Cu(1.8)/Al(2)	35	96
Ta(5)/C_{60}(10)/Al(2)/Cu(2.5)/Al(2)/C_{60}(10)/Al(2)	13	130
Mn		
Ta(5)/C_{60}(10)/Mn(10)/C_{60}(5)/Al(2)	11	105
Ta(5)/C_{60}(10)/Mn(5)/C_{60}(10)/Al(2)	7	112
Ta(5)/C_{60}(10)/Mn(10)/C_{60}(15)/Al(2)	9	86
Ta(5)/C_{60}(10)/Mn(10)/C_{60}(5)/Al(2)	3	101
Ta(5)/C_{60}(10)/Al(2)/M((5)/Al(2)/C_{60}(5)/Al(2)	In the background	N/A

this is due to the presence of Cu but not due to multiple deposition of C_{60}, C_{60} was deposited into multilayers but without Cu, [C_{60}(10.1nm)/Cu(0 nm)]$\times$8) where 0 nm here means Cu is not deposited. Another sample with the same thickness of C_{60} was deposited but without splitting C_{60}, [C_{60}(81nm)]. The roughness for these samples was the same (1.08$\pm$0.02) nm but different to the one with Cu, [C_{60}(10.1 nm)/Cu(1.1 nm)]x8, (0.85$\pm$0.02) nm, which can be due Cu filling C_{60} valleys and smoothing the molecular layer.

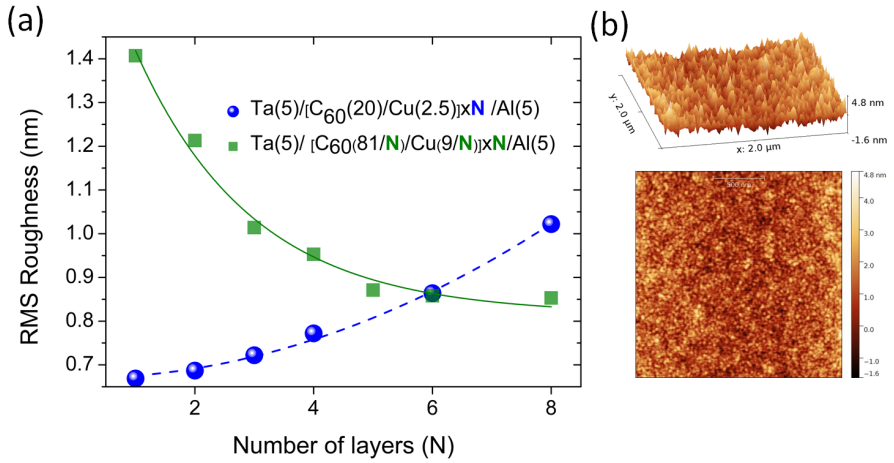

Figure 4.10: *(a) Atomic force microscopy (AFM) data for the same samples in figure 4.6(a) The root mean squared (RMS) roughness versus the number of layers. Green squares for the samples where the thickness of Cu and C_{60} is kept constant (line fit to asymptotic decay) whereas the blue dots for the samples with constant total thickness (line fit to N^2 dependence). (b) The images on the top right show three dimensional AFM images of a C_{60}(15)/Cu(2.5) sample with a cross sectional area of 2.0×2.0 μm^2 and a real 2-dimensional representation of the data with 500×500 nm^2 image.*

4.2.2 Low energy muon spin rotation spectroscopy

Magnetometry measurements showed the presence of magnetism in the multilayered stack of C_{60}/Cu, but breaking the interfaces by introducing Al or Al_2O_3 quenched this emergent magnetism. It also showed that the magnetisation depends on the thickness of the metallic layer. However, the magnetometry cannot provide information about the location of the emergent magnetism; if it is localized at the interface or if it extends further in both the metallic and molecular layers. Furthermore, magnetometry cannot determine how much each material contributes to the emergent magnetism. Conversely, LE-μSR overcomes the limitations of magnetometry and allows depth dependent investigations in multilayered samples. This technique showed successful results when it was applied to other metallo-molecular systems [101; 102]. In this technique, a beam of fully polarised positive muons are implanted in matter and work as a magnetic spin nanoprobe. The energy of the muons is varied between the eV and keV range so the beam can stop at different depths in the range of tens to hundreds of nanometers. The

local polarisation of the muons at different depths is detected using the decay of the positrons which emit in the direction of the muon spin, see section 3.5.1.

In this scenario, two approaches have been adopted to support the emergent magnetism at C_{60}/Cu interfaces that was observed using magnetometry. In the first approach (section 4.2.2.1) two samples were studied: a magnetic sample with molecular interfaces (Cu/C_{60}) and a non-magnetic sample with decoupled interfaces (Cu/Al_2O_3/C_{60}) as a control. In the second approach, a multilayer sample with thick and thin layers of Cu embedded between C_{60} layers is used to probe the dependence of magnetism on the metallic layer thickness (section 4.2.2.2).

4.2.2.1 Magnetic moment localisation at Cu/C_{60} interface

To determine where the emergent magnetism is localized, two samples were deposited: magnetic multilayer-*A* sample with the structure (from bottom to top) Ta (5 nm)/C_{60}(20 nm)/Cu(2.5 nm)/C_{60}(50 nm)/Au(10 nm), and non-magnetic multilayer-*B* with Al_2O_3 layers introduced between Cu and C_{60} to decouple the interface, as a control sample. The magnetometry measurements of theses samples are shown in figure 4.11. In the sample structure, the gold layer is used as a cap layer to protect the inner layers from oxidation and it helps to slow the incident positive muon beam. A thick 50 nm top C_{60} layer is deposited to allow the measurement of a distinguishable signal from the C_{60}/Cu interface without interference from the signal from the Au interface. To get a high magnetic signal, the thickness of the Cu layer is selected to match the highest magnetisation signal, as shown in figure 4.3, the 2.5 nm thick Cu layer. The total sample structure is designed to allow the probing of the layers with accessible positive muon energies. It also provides the maximum stopping profile at the area of interest, which is close to the C_{60}/Cu interface, without interference from the signals from other layers. Therefore, contributions from different layers will be distinguishable, which allows better understanding of the interfacial effect. The depth distribution of the implanted muons was simulated using the Monte Carlo program *TRIM.SP* [103; 104], see figure 4.11. It was used to calculate the fractions of muon in each layer based on the interaction between muons and matter, where the materials type, density and thicknesses are taken

into account.

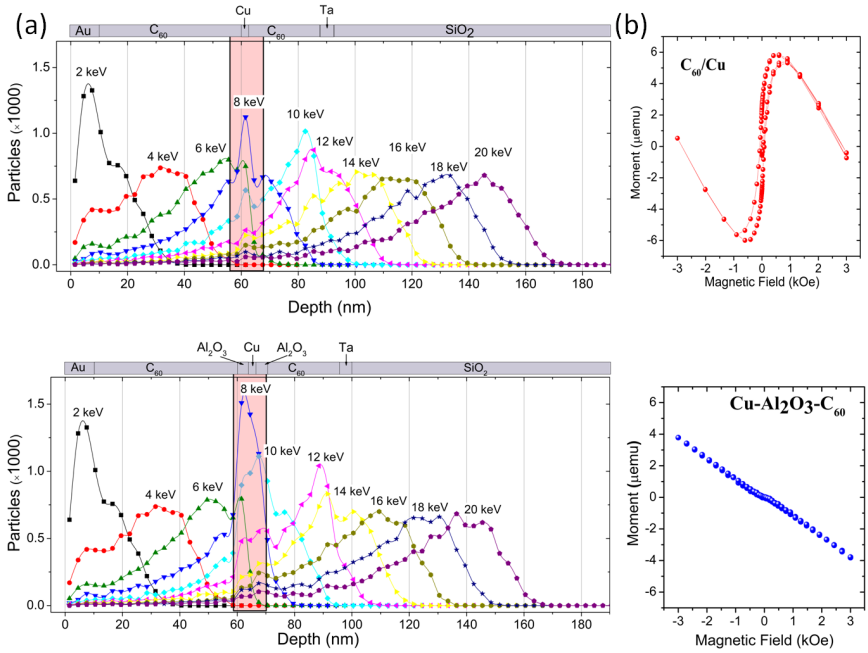

Figure 4.11: *(a) Muon stopping profiles in Ta(5)/C_{60}(20)/Cu(2.5)/C_{60}(50)/Au(10) multilayer-A (top) and a Ta(5)/C_{60}(20)/Al_2O_3(4)/Cu(2.5)/Al_2O_3(4)/C_{60}(50)/Au(10) multilayer-B (bottom). The lines are guides for the eye. The red shaded areas indicate the active and decoupled molecular interfaces for each sample respectively. The maximum absorption of muons for this region takes place at 8 keV where the Cu layer is located. (b) The raw magnetometry data for the Cu/C_{60} (top) and the decoupled sample Cu/Al_2O_3/C_{60} (bottom). A clear hysteresis loop and magnetisation is observed in the first sample while the decoupled sample shows only a diamagnetic contribution from the silicon substrate. The lateral size of these samples is 3×3 mm^2. However, the size of the samples used in the muon experiment is 2 to 2.5 cm; the maximum size to deposit uniform layers while being large enough to match the size of the muon beam [71].*

The μSR measurements were performed at 250 K with different probing energies for both samples; multilayer-*A* and multilayer-*B*. The first measurements were done at zero magnetic field with four different implantation energies: 4 keV, 6 keV, 8 keV and 16 keV as illustrated in figure 4.12b. At 4 keV, muons probe the identical uppermost C_{60}(50 nm)/Au(10 nm) layers of both samples. The magnetic multilayer-*A* exhibits a fraction of approximately 10% loss in the polarisation of the implanted muons at 4 keV. This gives an indication that a region of the sample is influenced by the magnetism which may arise from the stray field of the magnetic interfaces. On increasing the implanted energy to 6 keV, the difference between the two spectra of multilayer-*A* and multilayer-*B* increases and becomes even more pronounced at 8 keV, where a bigger fraction of muons is probing the Cu layer. This reveals that the Cu layer is magnetic in multilayer-*A*, else an overall increase of the muon polarisation would be observed. At implantation energy of 16 keV, the highest muon fraction is located in the substrate and 20% in the bottom C_{60} layer. At this depth, which is far away from Cu layer, the muon polarisation signal decreases. This observation suggests that the magnetism is localised at the Cu/C_{60} interface.

In order to investigate more about the distribution of the magnetism, the μSR response in the zero-field remanent state was studied. The experiment was performed by applying a magnetic field with a strength of 300 G to the samples in order to magnetise them, thus enhancing the depolarisation of muons. The field was removed during the measurements in order to measure in the remanent state. As seen in figure 4.12 at 8 keV, there is a clear difference in the magnetic sample multilayer-*A* spectra in the remanent state compared to the virgin spectra. On the other hand, the non-magnetic multilayer-*B* experienced subtle changes even in the remanent state. To clarify the origin of the observed oscillations, the μSR spectra were fitted to equation 3.9 for each energy at both zero-field virgin and zero-field remanent states. The oscillation frequencies extracted from the fit are plotted in figure 4.13a as a function of energy.

As shown in figure 4.13a, in the zero-field state, both samples exhibited an oscillation at 0.4 MHz. The 0.4 MHz precession can be attributed to the muonium state formed in semiconducting C_{60}. Muonium is a bound state that can be formed when a positive muon is slowed down in matter and picks up an electron from an atom in the

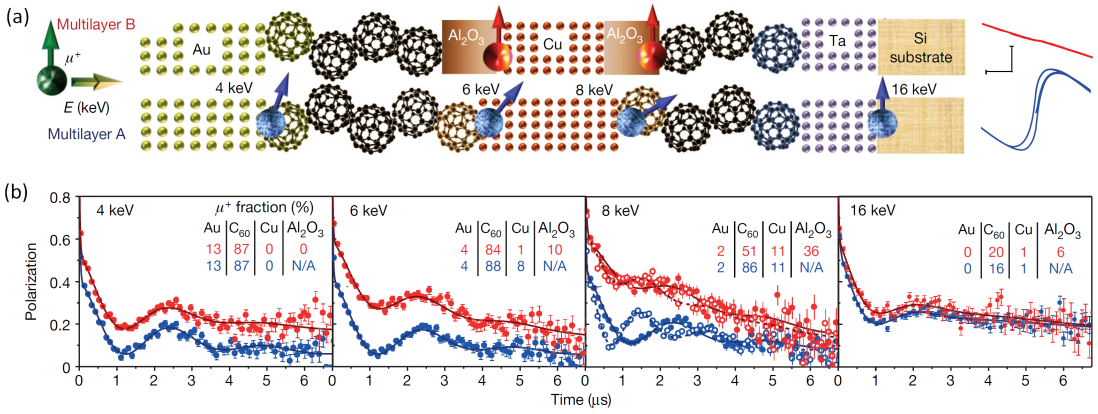

Figure 4.12: *(a) Schematic representation of a spin-polarized muon implanted in the measured samples; multilayer-A, [Ta(5)/C_{60}(20)/Cu(2.5)/C_{60}(50)/Au(10)]; and the control, multilayer-B, [Ta(5)/C_{60}(20)/Al_2O_3(4)/Cu(2.5)/Al_2O_3(4)/C_{60}(50)/Au(10). The muon enters the sample with its spin pointing along a specific direction. The polarity of the spin changes when it is subjected to a local field within the sample.The hysteresis loops to the right are the raw data obtained from magnetometry measurements; the horizontal scale bar denotes 1kOe and the vertical scale bar denotes 100 emu per cm^3 of Cu. (b) Zero-field μSR spectra for four different implantation energies: 4 keV, 6 keV, 8 keV and 16 keV for both multilayer-A and multilayer-B. The former is plotted in blue whereas the latter is in red. The tables show the percentage of muon fraction stopped in each layer. At 8 KeV, where the muon mostly stopped in the Cu layer, zero-field μSR spectra are shown in closed and open symbols indicating the measurements before and after applying a magnetic field of 300 G respectively [71]*

stopping material (abbreviated Mu= μ^+e^-) [105; 106]. It is formed in intrinsic semiconductors and insulators but not in metals. Metals have a strong cloud of conduction electrons that can collectively screen the muon's positive charge. However, a collective screening cannot take place in semiconductors and insulators and the muon often forms muonium state. Muonium also has a net polarisation that makes it a sensitive probe of local magnetic field. The muonium oscillation frequency formed C_{60} is shifted to 0.6 MHz after applying an external field of 300 G. The shift is due to the small residual field in the apparatus of about 0.3 G. Interestingly, the magnetic sample, multilayer-*A*, revealed an additional oscillation frequency at approximately 0.75 MHz which is not observed for non-magnetic sample multilayer-*B*. This new frequency, which is associated with the remanent state, is presumed to be correlated to the presence of an

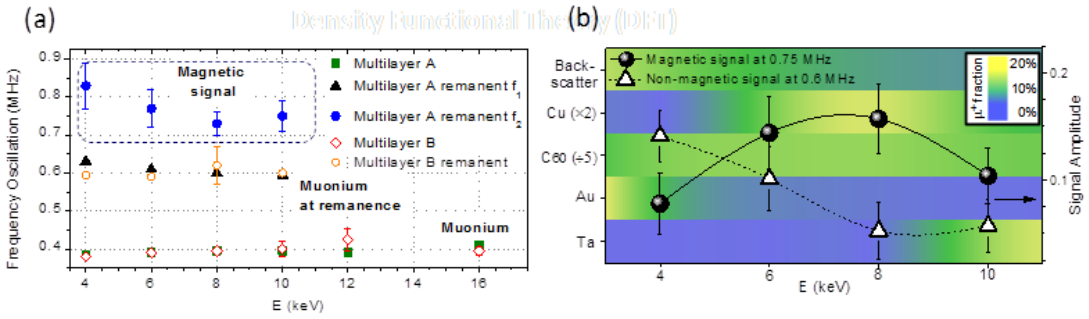

Figure 4.13: *(a) The fit of the oscillation frequencies data in figure 4.12b for the multilayer-A and multilayer-B (control) samples. Multilayer-A shows an additional frequency (0.75 MHz) in the remanent state measurements which does not appear in the control sample. (b) The polarisation amplitude of both the magnetic signal (0.75 MHz) and the non-magnetic signal (0.6 MHz) in the multilayer-A sample. The right-hand axis represents the amplitude of oscillation at a given energy. The background shading is the fraction of muons stopped in the given layers; the layers are presented in the left-hand axis and the percentage of μ^+ fraction is shown in the inset. Backscatter is the fraction of muons that do not decay in the sample. Here, the additional magnetic signal (0.75 MHz) follows the muon fraction that stopped in the Cu layer is maximum at 8 keV. The non-magnetic signal at 0.6 MHz shows the minimum at the same energy [71].*

additional magnetic field of about 0.1 Oe generated by the magnetic interface. It is observed at energies $\leq$10 keV, however its amplitude follows the fraction of muons stopped in the Cu layer as shown in figure 4.13b. The non-magnetic signal at 0.6 MHz, on the other hand, follows the opposite trend to the magnetic signal of muons stopped in C_{60}. All observed results give a clear signature of the existence of a magnetic moment localised in the metallic layer close to the Cu/C_{60} interface.

To clarify the role of muonium and its correlation to the magnetism of the sample, low temperature measurements were performed. The formation of muonium is pronounced at lower temperatures where C_{60} molecules are orientationally ordered [107] and nonconducting; about 75% of the implanted muons in the C_{60} layer form muonium. For this purpose, the magnetic sample multilayer-*A* was measured at 20 K where the formation of muonium is more pronounced. The sample here experienced three low frequency oscillations, 1.2 MHz, 7.4 MHz and 8.6 MHz, that are characteristic of C_{60} [107] as shown in figure 4.14a. The fact that the oscillation frequencies of muonium

are clearly observed at 20 K gives strong evidence that the magnetism is localised in the Cu layer or at the Cu/C_{60} interface. Otherwise, if the magnetism is localised in C_{60}, the oscillations of the muonium would be strongly shifted and would even disappear due to the internal magnetic field. Also, if the sample is free of magnetic ordering, one expects a rise in the muonium asymmetry signal as penetrating deep inside the sample and probing more C_{60} material. However, the muonium signal shows a decrease as the muons start probing the Cu/C_{60} interfaces, 6-8 keV in figure 4.14b. This effect gives further support that the emergent magnetism is localised at the interface.

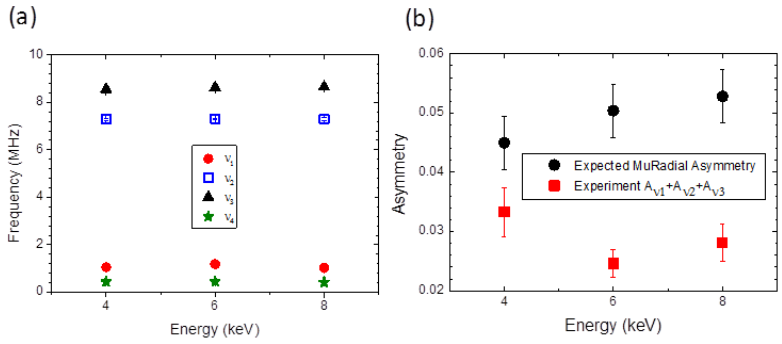

Figure 4.14: *Low temperature fitting of the muonium (Mu) radical lines of the magnetic sample multilayer-A. (a) Oscillation frequencies (radical lines) as a function of the implantation energies; ν_1, ν_2, and ν_3, are the muonium frequencies in C_{60} [107]. (b) Asymmetry (polarisation) of the muonium frequencies and comparison to expected asymmetries given the number of muons stopped in C_{60} layers. The expected asymmetry is calculated by adding the amplitude of low frequency lines respectively for 4, 6 and 8 keV with both fraction of muon in C_{60} and fraction of Mu radical [71].*

4.2.2.2 Metal thickness dependence of the μSR spectra

The object of this study is to reinforce the magnetometry results observed in section 4.2.1.1 which show that the observed magnetic ordering only emerges in thin metallic layers while thick metallic layers show no magnetic contribution. The charge transfer is screened by free electrons in the metals, so the muon behaviour is different when they stop close to thick layers and thin layers of metal. In this approach, a sample with two different Cu thicknesses at the interface is used to probe the dependence of magnetism

on the metallic layer thickness. The sample has a structure Si(sub)/Ta(3 nm)/C_{60}(20 nm)/Cu(2.5 nm)/C_{60}(50 nm)/Cu(15 nm)/C_{60}(20 nm)/Au(10 nm), from bottom to top. The structure of the sample is chosen to probe different layers in the sample within particular muon energies. The middle C_{60} layer is 50 nm thick to ensure that the muon particles that stop on the top thick Cu interface and the bottom thin Cu interface are detected separately at specific energies. The thickness of the Cu layer was selected according to the magnetisation dependence curve in figure 4.3, where a 2.5 nm Cu layer (bottom) showed the maximum magnetisation and for a 15 nm Cu layer (top) no magnetisation was apparent. In this experiment, the muon energy was tuned from 4 to 18 keV so that the depth of implantation varied between 10 and 180 nm, as shown in figure 4.15a. Muon energy of 10 keV and 18 keV probe the majority of the thick top layer and the thin bottom layer respectively. The hysteresis loop of an equivalent sample was measured via SQUID magnetometry as shown in figure 4.15b. It provides a direct confirmation of the presence of magnetism, however it does not provide information about where it is localised.

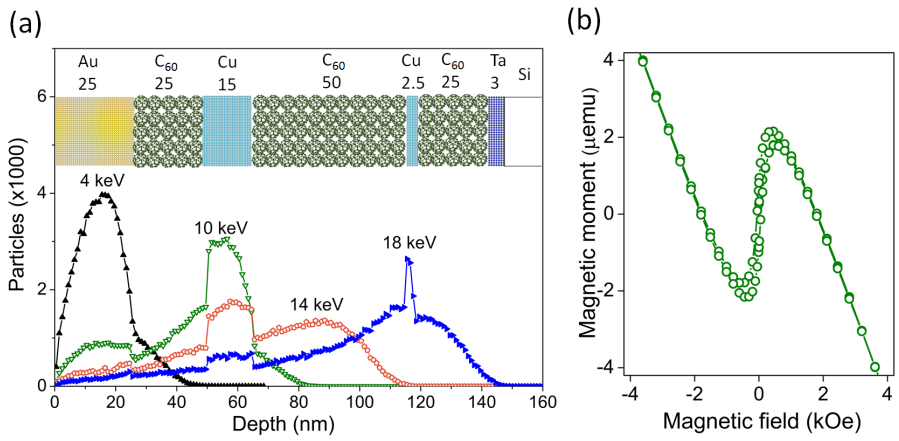

Figure 4.15: *(a) Muon stopping profile of Si(sub)/Ta(3)/C_{60}(20)/Cu(2.5)/C_{60}(50)/Cu(15)/C_{60}-(20)/Au(10) from bottom to top. 10 keV and 18 keV energies are targeting the thick top layer and the thin bottom layer respectively. (b) Raw hysteresis loop of the equivalent sample measured at room temperature.*

To confirm that only the bottom Cu layer contributes to the magnetisation, both layers were studied in the zero-field state and the zero field remanent state at 250 K,

figure 4.16. The detected oscillating μSR signals suggest the existence of relatively ordered magnetic structure at the bottom interface. This is seen as a drop in the polarisation of the muons as they are implanted deeper within the sample towards the magnetic Cu interface. It is also apparent that the asymmetry tail follows the same trend (figure 4.16b) which means that the depolarisation is enhanced due to a sudden change in precessional frequency for the muons. The loss of polarisation here is greater towards the thin Cu layer. After applying a field of 500 G at remanence zero-field, the reduction in the asymmetry tail signal experienced by the muons is further increased. This is an indication that the bottom interface is magnetic and the slight decrease with the other layers could be attributed to the stray field generated at the magnetic interface that extends a bit further over a certain range of depths. This would affect the muons polarisation in other layers, however the maximum contribution originates at the magnetic interface.

Zero-field μSR measurements provide the first evidence of the presence of local magnetism in the thin Cu interface, due to the sensitivity of this method at detecting weak internal magnetism that arises in magnetically ordered materials. The transverse-field (TF) configuration was also used; it allows more information to be gained about the field distribution within sample layers, mainly because the precessions are stronger with an applied field than when recorded in the zero-field geometry. In this configuration, an external field is applied perpendicular to the initial muon polarisation. Figure 4.17a shows the polarisation extracted from TF- μSR time spectrum that was collected at 250 K in a field of 143 G. There is a rapid loss in asymmetry from an initial value of ~ 0.17 that occurs at 4 keV to a value of ~ 0.08 at 18 keV, as the implanted muons approach the interface with the thin Cu (2.5 nm) layer. If there is no internal field present in the sample, muons will precess in phase so their polarisation is conserved. However, if there is a slight variation in the field from one layer to another, the muon precessions progressively dephase and the oscillation is damped [102]. This can be observed clearly in figure 4.17a where the phase (the change in the direction of muon polarisation) changes more than 40 degrees as the muon energy is raised to 18 keV, close to the thin Cu interface. The precessional frequencies of the muons consequently change when the muons experiences a local magnetic field. This is confirmed by a step increase in the oscillation frequency corresponding to a change in the field of

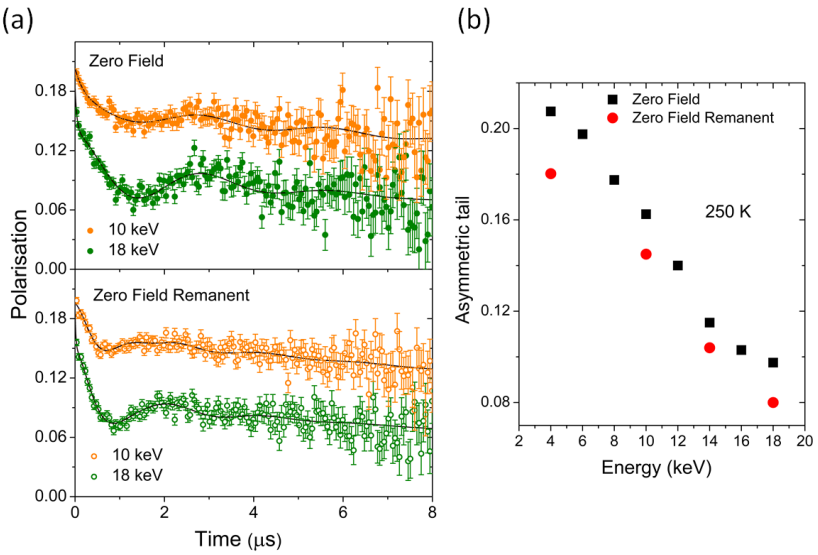

Figure 4.16: *(a) Low-energy muon spectroscopy (μSR) spectra showing the polarisation in a time frame of 8 μs in a multilayered system Ta(3)/C_{60}(20)/Cu(2.5)/C_{60}(50)/Cu(15)/C_{60}(20)/Au(10). The closed symbols represent the zero-field measurements before applying an external magnetic field whereas the open symbols represent the measurements after applying a 500 G field (remanent state). (b) The amplitude of the asymmetry tail as a function of implanted muon energy showing the strongest contributions from the bottom layers.*

about 0.15 G when the muons penetrate the first C_{60} layer in contact with Cu (2.5 nm), see the bottom panel of figure 4.17a. The dephased muon signal and the change in frequency suggest the existence of well ordered magnetic moments close or at vicinity in the neighborhood of the thin Cu (2.5 nm) layer but not the thick Cu layer (15 nm).

Low temperature measurements also play a part in this investigation to yield information on the correlation between the muonium states in C_{60} and the local magnetism. Figure 4.17b shows the frequency oscillations corresponding to the muonium states of semiconducting C_{60} obtained at 20 K from various implantation energies. The asymmetries of the three frequencies were added and compared to the fraction of muon implanted into the C_{60} layers. Since muonium is related to C_{60}, the corresponding signal is expected to increase as more C_{60} is probed. However, the amplitude of the signal decreases over the range of energies that target the bottom Cu layer (2.5 nm) and the

surrounding C_{60} layers in the zero-field remanent state. The fact that the amplitude of oscillation is less pronounced and does not follow the relative contribution from C_{60} gives an indication that the signal is sustained by the existing magnetism, which originates in the thin bottom interface.

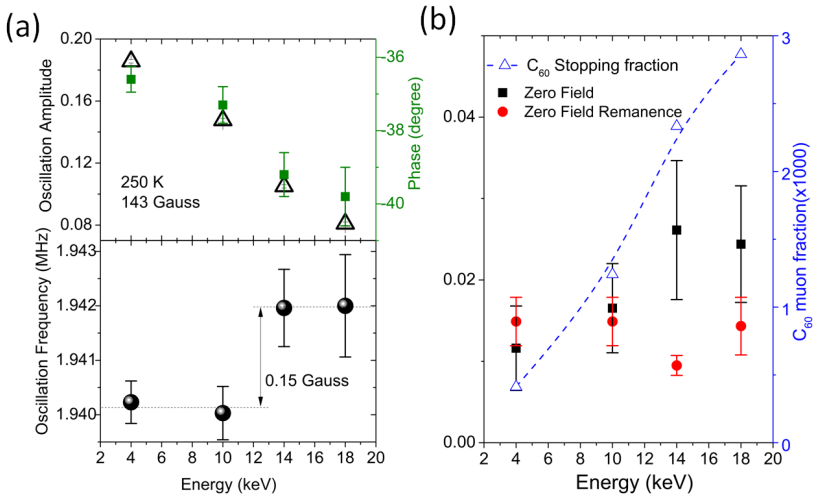

Figure 4.17: *(a) Top panel, the amplitude of oscillation as a function of implanted muon energy in an externally applied transverse field of 143 G at 250 K. Bottom panel, the oscillation frequency for the same applied field shows a change in the frequency as the muons get closer to the C_{60} layer that is in contact with the thin Cu layer. (b) The amplitude of oscillations for the three muonium frequencies at both zero-field and zero-field remanent states. The blue triangles show the contribution of the C_{60} layers to the muonium signal.*

4.2.3 X-ray absorption spectroscopy and magnetic dichrosim

As anticipated, magnetometry and low energy muon experiments strongly suggest the presence of emergent magnetism at the Cu/C_{60} interface. Nevertheless, obtaining reliable information about the sample compositions in order to discriminate the effect of impurities is essential. Experimental investigation of the impurities was studied by means of XAS. XAS spectra of a Ta(5 nm)/C_{60}(10 nm)/Cu(2.5 nm)/C_{60}(10 nm)/Al(2 nm) sample was measured at selected energies to allow the identification of various elements, including magnetic transition metals such as Co, Fe and Ni. The absorption

signal shows no signs of transition metal impurities, as shown in figure 4.18. However, the use of a thin cap layer, 2 nm of aluminium, cannot prevent the oxidation of the sample and a high content of oxygen is present. In order to minimise the sample oxidation, a thicker cap layer of heavier metals and/or noble metals that wet the C_{60} film can be used as an alternative. However, a thick layer is expected to stop emitted electrons before they reach the sample surface, hence the electron yield will be significantly reduced and any small signal, such as potential dichroism, will be lost in the noise level.

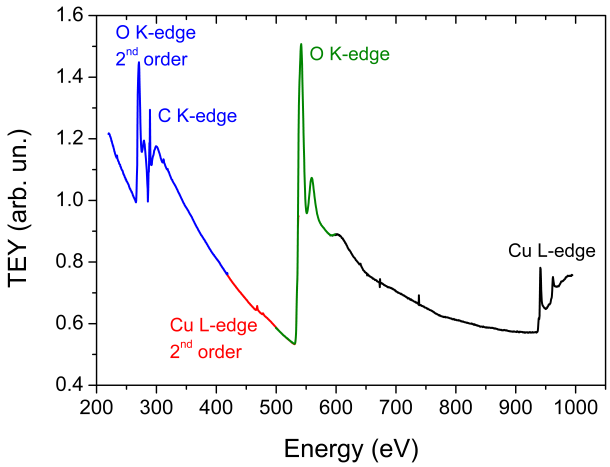

Figure 4.18: *XAS spectra of a Ta(5)/C_{60}(10)/Cu(2.5)/C_{60}(10)/Al(2) sample, revealing the elemental compositions at various photon energy. K and L edges corresponding to the excitation of an electron from n =1 and 2 shells, respectively are labelled. Oxygen is present in the sample due to the thin cap layer giving rise to extra features such as a shift in the edge position within the XAS region [71].*

To improve the quality of the signal and deconvolute artifacts that are due to shifts in energy of the equipment, XAS spectra are measured repetitively. This shows a large variation in oxygen peak during the measurements due to a radiolysis process, which results from irradiating the sample with X-ray and attributes to dissociate oxygen from the sample. Figure 4.19 reveals a comparison in XAS spectra between the first and the twelfth scans of the same sample. The oxide shoulders of both K-edge and $L_{2,3}$ edges show a reduction that could be associated with the measurement conditions; the X-ray

beam and the vacuum seem to provide a partial annealing environment to the sample.

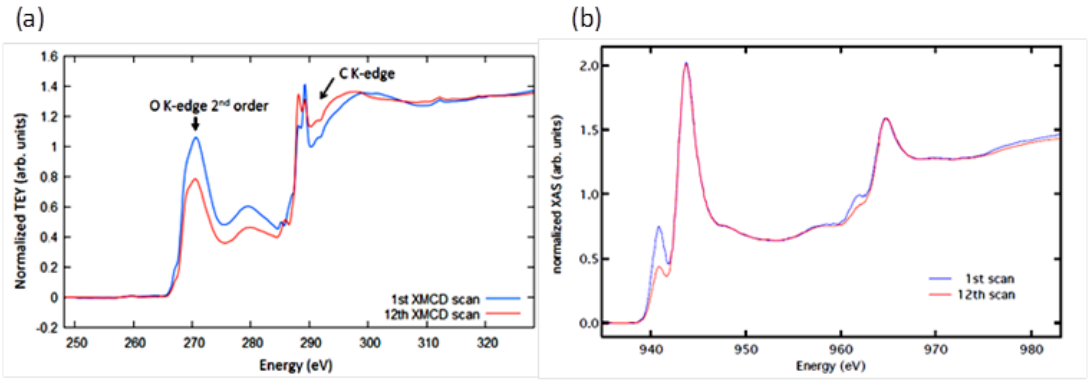

Figure 4.19: *The electron photoemission of the (a) Carbon K-edge and (b) Cu $L_{2,3}$ edges. Both elements show the presence of oxygen peaks that are reduced during the measurements. A comparison between the first (blue) and the twelfth (red) scans of a Ta(5)/C_{60}(10)/Cu(2.5)/C_{60}(10)/Al(2) sample showing a significant reduction of oxygen peaks that is seen in both the carbon edge and Cu edge [71].*

Measuring XAS spectra with the two opposite circular polarisations and taking their difference provides an important insight to investigate magnetic properties of the sample. This technique is known as XMCD, see section 3.5.2. For this purpose, the XAS spectra were measured for the Cu edges at selected right (h^+) and left (h^-) handed circularly polarised X-ray beams as shown in figure 4.20 and described in section 3.5.2. There is a small difference in the electron yield for different polarised beams as indicated in the inset in figure 4.20. This difference (dichroism) may be indicative of magnetic Cu, although the signal is very small and could be due to an artifact in the measurements. The potential dichroism is mostly observed in the L_3-edge but not L_2-edge, where the latter is almost lost in the noise. The dichroism of the L_3-edge is detected over 15 scans where the first two scans may suggest that the changes in the signal are due to the presence of oxygen which is reduced after the second scan. The data over the rest of the scans reveal a very small dichroism that could indicate magnetism in the Cu L_3-edge, however it is not firm evidence since the signal is within the noise level.

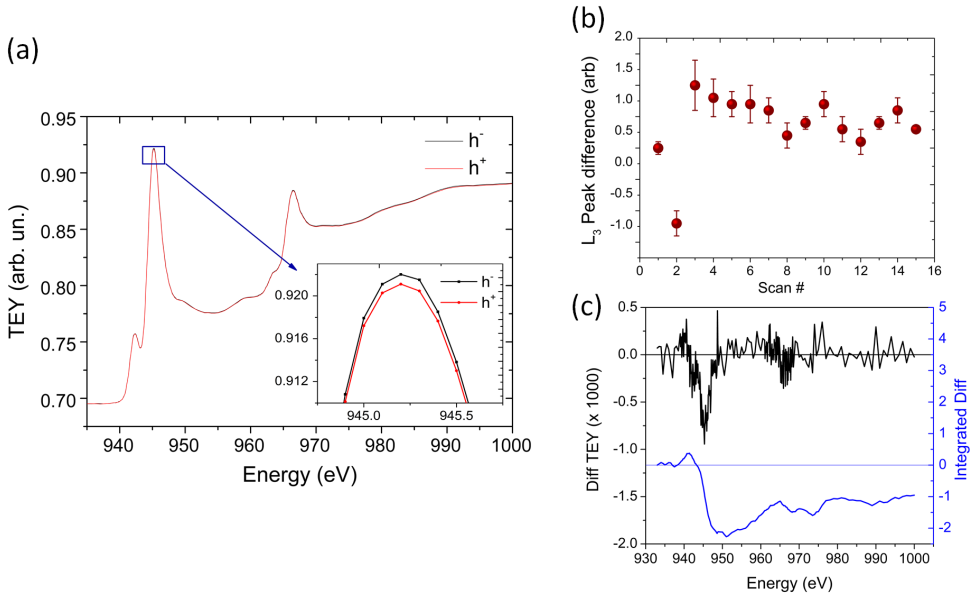

Figure 4.20: *(a) The absorption of left (h^-) and right (h^+) circularly polarized X-rays for $L_{2,3}$ Cu edges, obtained from a multilayer of Ta(5)/C_{60}(10)/Cu(2.5)/C_{60}(10)/Al(2). The two spectra (black and red) correspond to the absorption of right and left handed circularly polarised light respectively. Inset: the L_3-edge dichroism signal measured at room temperature and averaged over 15 measurements; it might provide evidence for an induced magnetic moment in the Cu edge. (b) The dichroism signal of Cu L_3-edge shows the consistency in the data after the 3rd scan despite the electron yield is very small. The first two scans demonstrate a different signal compared to the rest of the scans. This could be due to the presence of oxygen which is reduced during the measurements and recovers the Cu/C_{60} interface. (c) XMCD averaged for 15 scan, the dichroism is apparent in L_3 edge but the signal for L_2 disappears in the noise [71].*

Another strategy to observe the dichroism was to deposit samples with a thicker cap layer to prevent the oxidation process. A 3 nm silver (Ag) cap was added to the Al cap in this investigation, however the electron yield was too low. Alternatively, the total fluorescence yield (TFY) was measured instead of the electron yield. The sample with the silver/aluminium cap showed no oxygen shoulder compared to the sample with only the aluminium cap, see figure 4.21b. Although the oxidation is prevented by using a thick cap layer, the dichroism signal is less straightforward to observe and is not clearly distinguishable in the noise level as illustrated in figure 4.21c.

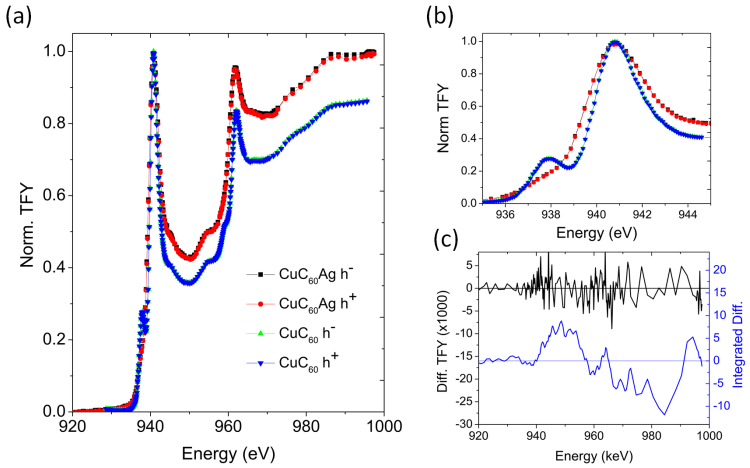

Figure 4.21: *The dependence of the absorption of circularly polarized X-rays on the capping layer at the Cu $L_{2,3}$ absorption edges. (a) XAS for a thick cap Ta(5)/C_{60}(10)/Cu(2.5)/C_{60}(10)/Ag(3)/Al(2) sample and the sample with a thin cap layer Ta(5)/C_{60}(10)/Cu(2.5)/C_{60}(10)/Al(2). (b) The L_3-edge of both samples show the absence of an oxygen shoulder for the sample capped with Ag(3)/Al(2). (c) The difference between up and down polarisations (dichroism) of the sample capped with silver/aluminium and measured in fluorescence mode. The dichroism signal here is within the noise level compared to dichroism signal in the aluminium capped sample in figure 4.20 [71].*

4.3 Conclusion

In this chapter, the emergent spin ordering that arises at the diamagnetic (Cu) metal and C_{60} interfaces has been studied intensively using magnetometry, LE-μSR and XAS. The findings highlight the essential role of interfacial coupling on the emergent magnetism due to hybridisation and charge transfer at Cu/C_{60} interfaces. The data obtained using magnetometry shows that the samples are ferromagnetic at room temperature but only when/or is maximised when the metallic layer is thin and continuous. In thick metallic layers, the bulk properties dominate, hence the charge transfer is screened by free electrons, resulting in a quenching of the emergent magnetism. The magnetisation also disappears when the interfaces are decoupled by an aluminium (or alumina) spacer which prevents any electron transfer or hybridisation arising due to the metal-organic interface. The magnetisation dependence on temperature showed a trend that follows a typical magnetic ordered system. To complement these results, a comprehensive study

of reproducibility and degradation was performed on Cu/C_{60} systems. The emergent magnetism can be controlled and protected by increasing the number of interfaces, a good choice of a cap layer and annealing. The roughness plays a role in the quality of the samples and it can be controlled by annealing.

The μSR results showed that the emergent magnetism is localised at or close to Cu/C_{60} interface which is correlated with an additional frequency that appeared in the remanent state. Decoupling the interface with alumina suppressed this oscillation. The emergent magnetism at the C_{60} interface with different Cu layer thicknesses was probed by muons to elucidate the dependence on thickness that was achieved by magnetometry. It showed consistent results with the magnetism arising from the thin metallic interface (2.5 nm) but not thick film (15 nm), where the charge transfer plays an important role in controlling the spin ordering at metallo-molecular interfaces.

XAS showed evidence that the emergent magnetism does not arise because of the presence of magnetic impurities. This was done by tuning X-rays with a wide range of energies to investigate the transition magnetic metals where no sign of magnetic impurities was observed. However, the requirements of X-ray spectroscopy, as a surface sensitive tool, has some restrictions with respect to the sample. In this sense, a thin cap layer is required to allow the collection of electrons from the sample surface but sample oxidation appeared to be a problem. Replacing the thin cap layer with a thick one prevents sample oxidation but presents another difficulty related to very low yield of electrons. A dichroism signal was observed but was very small and particularly challenging to distinguish from the noise signal.

CHAPTER 5

Emergent magnetism at paramagnetic metal/C_{60} interfaces

5.1 Introduction

The transformation of non-magnetic elements into magnetic materials using molecular interfaces in diamagnetic Cu and C_{60} systems is presented in chapter 4. This observation gave the motivation to further understand this effect and to perform a systematic study investigating the influence of interfacial hybridisation on the modification of magnetic properties in other transition metals.

Paramagnetic manganese (Mn) and scandium (Sc) have been chosen as standard elements for this study. Bulk Mn and Sc are not magnetic under ambient conditions. Mn is a paramagnetic 3d metal that has a Stoner factor of 0.63, approximately six times larger than the one of diamagnetic Cu. Sc is the first in the series of transition metals and only has one electron in the 3d shell. It is paramagnetic but considered to be on the threshold of ferromagnetism; it has a Stoner factor of 0.825 and therefore lies close to the ferromagnetic instability where the Stoner factor is unity [25]. The density of states of Sc has a sharp peak at the Fermi energy [108], thereby making Sc magnetically very sensitive to external effects.

Similar to chapter 4, the observations made are based on using different techniques: SQUID magnetometry, low energy muon spectroscopy (LE-μSR) and X-ray absorption spectroscopy (XAS) and the related technique X-ray magnetic circular dichroism (XMCD) spectroscopy. In this chapter, the observation of emergent magnetism of both Mn/C_{60} and Sc/C_{60} multilayers using magnetometry is discussed. We studied the room temperature magnetisation and the change that the magnetism undergoes with changing the metal film thickness. We focused more on Sc/C_{60} multilayers due to the sharp peak that characterises Sc at the Fermi energy and any changes in density of states at the Fermi energy could significantly affects the magnetic properties. LE-μSR spectroscopy and XMCD have been used as complementary approaches to investigate the Sc/C_{60} system. In LE-μSR, we discuss the different muon behaviours with different interface thicknesses and relate them to the magnetometry results. XMCD is used to explore the magnetism at the carbon edge considering the change in the molecular orbitals due to charge transfer and hybridisation effects. In this chapter, the various

results for the Sc/C_{60} system obtained from each technique are compared.

5.2 Characterisation of hybrid paramagnetic metal/C_{60} interfaces

5.2.1 Magnetometry

Following the same sample deposition and measurement protocol described in chapter 4, the studied samples here are multilayers of Mn (Sc)/C_{60} where the metallic films are sequentially sputter deposited followed by thermal sublimation of C_{60}. The magnetometry discussion is divided into two main sections. The first section 5.2.1.1 focuses on the Mn/C_{60} interfaces, which presents a picture of the emergent magnetism of the paramagnetic metal interfaces compared to the Cu/C_{60} interfaces. This includes room temperature and the thickness dependence magnetisation measurements. The second section 5.2.1.2 describes the same concept but in a Sc/C_{60} system and discusses the divergence of the magnetic behaviour in this system. Further insight into the magnetic properties are investigated through the temperature dependence of magnetisation.

5.2.1.1 Mn/C_{60} interfaces

Room temperature measurements of the Mn/C_{60} system show a clear magnetic hysteresis, similar to the Cu/C_{60} system 4.2.1.1. The insertion of a thin spacer such as Al to decouple the interface between Mn and C_{60} suppresses the effect and the measurement follows the background signal, see figure 5.1.

Due to the low magnetic moment of the samples, the paramagnetic response which originates from Mn in addition to the diamagnetic response of the sample holder and the substrate are a relatively large contribution to the signal measured. These contributions have been subtracted from the measurements of all the samples to eliminate any input from bulk leaving only the magnetic signal due to the interfacial effect. Figure

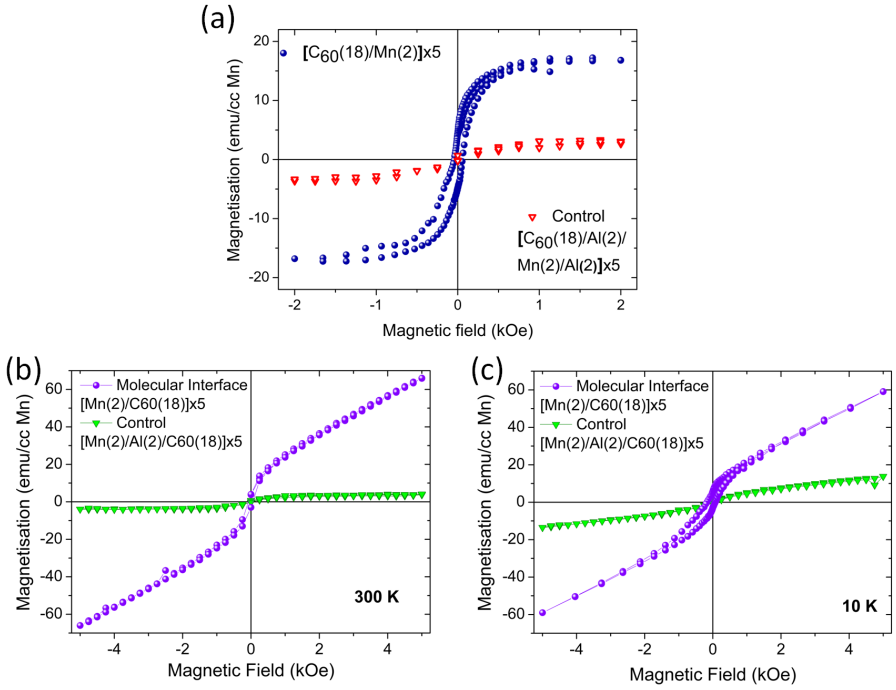

Figure 5.1: *(a) The field dependent magnetisation of a sample with the structure Ta(5)/[C_{60}(18)/Mn(2)]×5/Al(5) measured by a SQUID magnetometer at room temperature. The data indicated by red symbols is the control with the spacer where the interfaces are decoupled and the magnetisation suppressed; Ta(5)/[C_{60}(18)/Al (2)/Mn(2)/Al (2)]×5/Al(5). (b) The raw data for the same samples showing the paramagnetic contribution which have been corrected to exclude any effect from the bulk. (c) Low temperature measurements for the same samples [71].* ***All thicknesses in brackets are in nm.***

5.1a shows the corrected data whereas figure 5.1b shows the raw data with the background contributions.

The paramagnetic Mn and C_{60} system exhibits a similar magnetisation dependence on the thickness of the metallic layer to Cu/C_{60}. The magnetisation of multilayered Mn/C_{60} reaches a maximum when the Mn layer is approximately $\sim$ 4 nm. The magnetisation decays once the metallic layer exceeds 5 nm or if it is very thin and not continuous, less than 2 nm, as shown in figure 5.2. However, the magnetisation of the Mn/C_{60} samples is 3-4 times weaker than that of the Cu/C_{60}, as reported in chapter 4. This is probably due to strong charge transfer of up to $3e^-$ per C_{60} molecule on Cu sub-

strates [98]. Also, the d bands near the Fermi level are highly hybridised between the Cu surface and the molecule which means there is a strong metal-fullerene coupling [109; 110]. The d bands in Cu are also filled with electrons and are close to the Fermi level [25], whereas this is not the case for Mn. Cu also has better lattice matching with C_{60} which allows more charge transfer [99]. However, bulk Mn is paramagnetic and much closer to the Stoner criterion than diamagnetic Cu, so the effect propagates $\sim$ five times further in Mn than in Cu. The latter has a relatively weak exchange interaction and very small DOS(E_F), with Stoner factor of one order of magnitude less than unity, that makes the effect disappear quickly as it is becomes close to bulk [25].

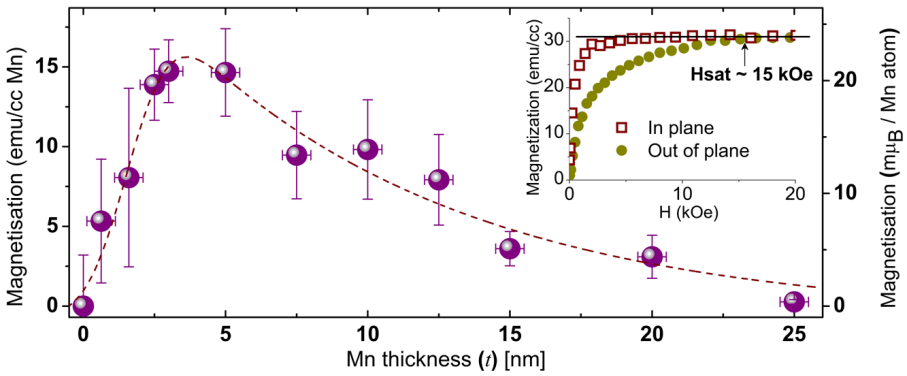

Figure 5.2: *Dependence of the magnetisation on the Mn film thickness for a total of 96 samples with the structure: Ta(5)/[C_{60}(10–20)/Mn(t)/C_{60}(10–20)]×(1–5)/Al(5). The data were taken at room temperature and the magnetisation here is the average, taking into consideration the thickness of the Mn layers only. The error bars in thickness and magnetisation are calculated corresponding to the roughness and the standard error of the mean respectively. Inset, In-plane and out-of-plane magnetisation versus applied magnetic field measured at room temperature for [C_{60}(15)/Mn(2.5)]×4 sample. The sample shows in-plane easy axis anisotropy with out-of-plane saturation field H_{sat} of 15 kOe [71].*

Magnetic measurements of Mn/C_{60} films exhibit magnetic hysteresis loops typical of an anisotropic easy axis that lies in the plane of the film. The loops measured along the hard axis (out-of-plane) have saturation fields that reach 15 kOe at room temperature, see the inset in figure 5.2. The fact that the samples show different magnetic behaviours in in-plane and out-of-plane orientations indicates the anisotropic nature of

the magnetisation, not consistent with the randomly distributed impurities or particles.

The magnetic properties of the samples are affected by various parameters such as the deposition pressure and substrate alignment with respect to the evaporation source. However, it has been observed that the sample roughness in particular could play important role in controlling the magnetic properties which could be correlated to different surface reconstructions. A set of samples were deposited in the same growth in order to adopt a correlation between sample roughness and the corresponding emergent magnetism. The measurements shown in figure 5.3a correspond to identical structures of Mn/C_{60} samples deposited adjacent to one another on one sample plate. Specular X-ray reflectivity has been employed in the characterisation of the roughness and thicknesses of these multilayer samples as shown in figure 5.3b. All multilayers studied consist of Mn/C_{60} bilayer subunits with a total thickness of approximately 21 nm. However, there is a variation in the RMS roughness of the samples that is consistent with the measured magnetisation. The measured magnetisation is observed to decrease dramatically with increasing C_{60} layer roughness.

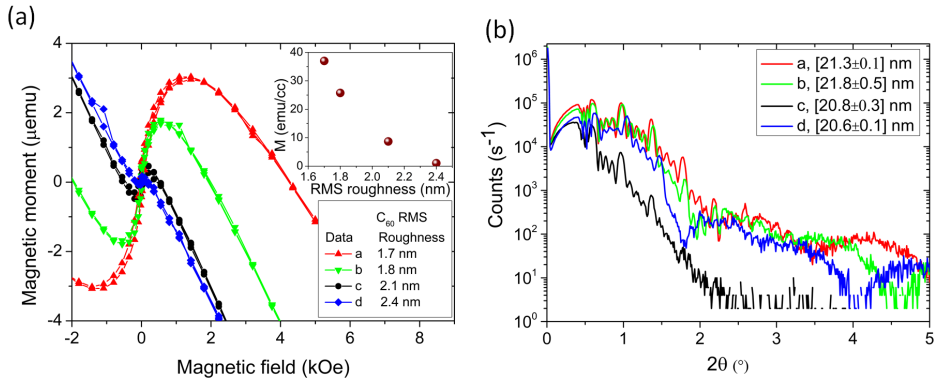

Figure 5.3: *Identical sample structures, grown side by side, show different magnetisation which could be due to roughness or thickness uniformity. (a) Raw magnetisation data of four Mn/C_{60} samples grown simultaneously on the same sample plate. The samples have a structure of Ta(5)/[C_{60}(18)/ Mn(2.5)]×4/ Al(5). Measurements taken at room temperature. (b) Low angle XRR of the same samples showing the thickness of one of bilayer is obtained by fitting the specular XRR from the samples via Bede software. The surface roughness of the samples is also determined using the same fit; table in (a). Surface roughness is observed to be associated with low magnetisation (M) as shown in the inset in (a) [71].*

5.2.1.2 Sc/C_{60} interfaces

In addition to observing emergent magnetism when diamagnetic Cu and paramagnetic Mn are in contact with C_{60}, paramagnetic scandium (Sc) has also shown evidence for ferromagnetic ordering using C_{60} molecular interfaces. The studied samples are thin films of Sc/C_{60} multilayers deposited *in-situ* under high vacuum conditions. The samples have a general structure of Ta(3.5 nm)/[C_{60}(15 nm)/Sc(*x nm*)]×4/Al(5 nm) where the thickness of Sc layer (x) was varied. Room temperature measurements of Sc/C_{60} multilayers were carried out via SQUID magnetometry and exhibited a clear magnetic behaviour as presented in figure 5.4a. In the metal, free electrons play a role in screening the charge transfer which leads to quenching of the emergent magnetism as the sample thickness is close to the bulk properties. This is observed clearly in the magnetisation dependence on the thickness as shown in figure 5.4b, whereby the effect follows an inverse dependence with thickness as the metallic layer exceeds $\sim$ 10 nm. Similar behaviour has been previously confirmed in both Cu/C_{60} and Mn/C_{60} multilayers. It is also expected that the magnetisation disappears if the metallic layer is discontinuous, however, Sc/C_{60} multilayers reveal a different trend. The magnetisation increases, whereas the magnetic moment is roughly constant, even if the Sc layer is very thin, $\sim$ <0.5 nm, with a value of magnetisation that exceeds 130 emu/cc as shown in figure 5.4b. This could be due to wetting properties of C_{60} by Sc films where at smaller thickness the Sc layer would be continuous.

One possible explanation is that the increase in the magnetisation is correlated to the oscillatory change in the magnetisation as a function of metallic film thickness which can be observed from the residual of the exponential fit as shown in the top panel of figure 5.4. The explanation could be based on the quantum well (QW) states that cause the complete quenching of magnetic moment for certain thicknesses as observed in palladium (Pd), rhodium (Rh) and platinum (Pt) thin films [111]. These QW states cross the Fermi level periodically as the thickness of the overlayer film changes accordingly, inducing oscillations in the DOS at the Fermi level. Therefore magnetism is enhanced and suppressed periodically whereby it satisfies the Stoner criterion or not respectively. This kind of behaviour has been studied extensively theoretically [111–113] in Pd thin films and confirmed experimentally by S. Sakurage et al. [114]. Like

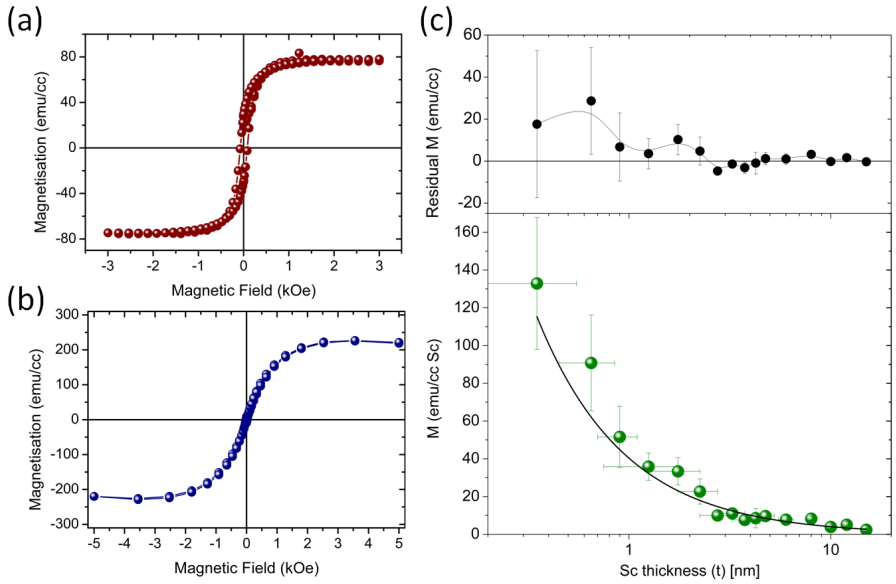

Figure 5.4: *(a) Room temperature hysteresis loop of typical sample with structure Ta(3.5)/[C_{60}(15)/Sc(1.8)]×4/Al(5). (b) Magnetisation per unit volume of Sc atom for Ta(3)/[C_{60}(20)/Sc(0.8)/C_{60}(20)/Al(5) was measured by a SQUID magnetometer at 300 K showing superparamagnetic-like behaviour. (c) Bottom: Room temperature magnetisation dependence of Sc thickness for a typical structure of Ta(3.5)/[C_{60} (15)/Sc(x)]×4/Al(5). Top: The residuals from the exponential fit of magnetisation data in the bottom curve are plotted as a function of Sc layer thickness.*

Sc, Pd is nearly magnetic and a small change in the DOS can alter the magnetic ground state to satisfy the Stoner criterion [25]. Thus Pd magnetism is very sensitive to any change in the environment, for example a monolayer of Pd revealed magnetism on a Ag substrate whereas a bilayer of Pd on the same substrate exhibited no magnetism [115]. The effect could extend further in multilayer films up to 15 monolayers (∼5 nm) in Pd thin films [114]. At specific thicknesses, i.e. specific boundary conditions, electrons in the metallic band can not scatter into the interface as there are no available states to occupy. Instead they experience a total reflection at the surface of the metal and are effectively confined between the surface and interfacial QW states. The resultant QW state in this case will exhibit either constructive or destructive interference depending on the film's thickness. The DOS will change accordingly and reach a state to validate the Stoner criterion for ferromagnetism. The thickness that does not satisfy the

condition is distinguished by a complete quench in the magnetic moment resulting in an overall oscillatory behaviour between magnetic and non-magnetic states [111; 114].

Although the formation of QW states may explain the oscillatory manner of magnetism, detailed discussions based on the energy band calculations and electron dynamics at the interface are required to understand the magnetic behavior of Sc/C_{60} system. In the energy band calculations, the band offset between the band edges of the two materials controls the confinement of the wave function well within specific layers.The phase matching conditions at the interface, on the other hand, plays a role in the electron reflection [116]. Whether or not there is a connection between the formation of QW states in Sc/C_{60} system and emergent magnetism remains to be explored. An experimental study that involves photoemission techniques [117] can be used to measure the electronic band structure and investigate the emergence of the QW states [116; 118; 119].

The oscillatory behaviour could alternatively be explained in a similar way to the Ruderman-Kittel-Kasuya-Yosida (RKKY) coupling mechanism between ferromagnetic layers embedded in nonmagnetic spacer layers [120–122]. In a structure: ferromagnetic metal/normal metal/ferromagnetic metal, the first magnetic layer interacts with the conduction electrons of the non-magnetic metal and spin polarises the electrons. The spin-polarised electrons propagate through the non-magnetic layer and couple to the other magnetic layer. The coupling depends on the separation between the magnetic layers. Hence the coupling may be either ferromagnetic or antiferromagnetic, leading to an oscillatory behaviour. In principle, the RKKY interaction appears to be a good candidate for the mechanism of oscillatory behaviour assuming the Sc/C_{60} interface is ferromagnetic and the part of Sc layer which is away from the interface is the non-magnetic spacer. However, this theory may not apply because the Sc layer could be either completely magnetic or the non-continuous layer which will not provide a perfect transport bridge to couple the other magnetic layers.

Another possible explanation is that reducing the thickness could lead to the formation of Sc/C_{60} nanoparticles which can behave in a superparamagnetic manner. The superparamagnetic behaviour is marked by an absence of magnetic hysteresis, i.e. no

coercivity. In this study, magnetometry measurements show nearly zero coercive field for samples deposited with very thin Sc layers, as shown in figure 5.4b. The samples with thicker Sc layers, exceeding 1.5 nm, do not show this behaviour as represented in figure 5.4a. Similar to superparamagnetic materials, the coercivity also shows an increase as the temperature is lowered. The temperature T dependent of coercivity H_c is plotted in figure 5.5a. It follows the dependence predicted for superparamagnetic system with high blocking temperature T_B according to

$$H_c = H_{c0}\left[1 - \left(\frac{T}{T_B}\right)^{\frac{1}{2}}\right] \tag{5.1}$$

where H_{c0} is the coercivity at 0 K [123; 124].

Further analysis of the layered structure of the Sc/C_{60} was accomplished by measuring the magnetisation behaviour as a function of temperature for samples with different thicknesses of Sc layers; 2.0 nm and 0.2 nm . Figure 5.5 shows the temperature dependence of the magnetisation. In the zero-field cooling process (ZFC), the sample was cooled from 300 K down to 5 K without applying an external magnetic field. The magnetisation was then measured as a function of temperature in a small applied field of 100 Oe during a warming process. In the case of field cooling (FC), the sample was cooled from 300 K down to 5 K in the same small applied field. In both samples, the observed ZFC and FC magnetisation curves indicate a thermal hysteresis that moves to lower temperatures. The difference between ZFC and FC curves with temperature reflects the irreversibility of the magnetic behaviour and is related to the energy barrier of the magnetic anisotropy of the samples and the thermal energy. In the ZFC process, where there is no external field applied to the sample, the spins exhibit random orientations. Applying a field at low temperature may align some of the spins if the magnetic anisotropy of the sample is sufficiently low. By increasing the temperature (i.e. raising the available thermal energy) under the same field, the ZFC magnetisation curve increases as the temperature increases. The rise in magnetisation could be consistent with the inhomogeneous nature of the particles in which the particle size distribution and individual anisotropy axes are associated with different temperatures to align them. During the FC process, the same system with low anisotropy retains the magnetisation while lowering the temperature (i.e. decreasing the available thermal

energy) [125; 126].

The thin Sc samples, figure 5.5b, show a thermal hysteresis that could be corresponded to superparamagnets but not related to ferromagnetic materials. The experimental observation of this behaviour may give an indication of the dynamic nature of the magnetic ordering at metallo-molecular interfaces.

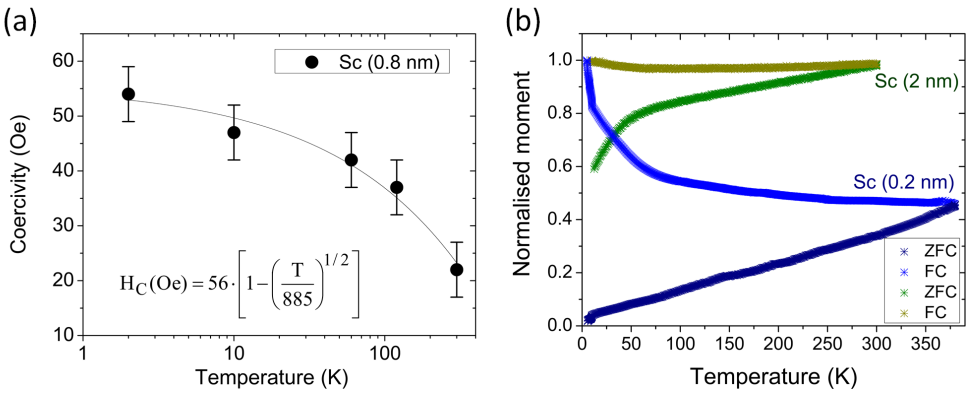

Figure 5.5: *(a) The coercivity for 0.8 nm Sc film with C_{60} interfaces as a function of temperature. The solid line represents the dependence for superparamagnetic systems with a high blocking temperature of 885 K; it is fitted to equation 5.1. (b) Magnetisation versus temperature curves under zero-field cooling (ZFC) and field cooling (FC) conditions for Ta(3.5)/[C_{60}(15)/Sc(x)]×4/Al(5): (a) x = 2 nm (b) x = 0.2 nm. In ZFC condition, the sample is cooled with zero field. At the lowest temperature an external field of 100 Oe is applied to rotate the spins and the magnetisation curve is measured while heating. The FC measurement is the process when the same applied field is maintained but the magnetisation curve is recorded while the sample is cooling down. The data for 0.2 nm Sc film in (b) is smoothed.*

5.2.2 Low energy muon spin spectroscopy

The charge transfer resulting from the hybridisation between the 3d band and the molecular orbitals varies depending on the metal thickness. Free electrons in a thick metallic layer screen the charge transfer rapidly, compared to a thin layer where the role of free electrons is less pronounced. Magnetometry measurements suggest that magnetism only appears in the thin metallic layers where the charge transfer effect

takes place but not the thick metallic layers. In LE-μSR experiment, the spin-polarised muon beam was tuned with energies from 2 keV to 14 keV in order to penetrate the sample with a depth between a couple of nm and a few hundred nm. The investigated sample has a structure of Ta(3 nm)/C_{60}(20 nm)/Sc(2 nm)/C_{60} (50 nm)/Sc(5 nm)/C_{60}(20 nm)/Au(10 nm). The sample consisted of a thick top Sc (5 nm) layer and a thin bottom Sc (2 nm) layer to provide information about the emergent magnetism in different interfacial thicknesses chosen according to figure 5.2. These layers are separated with a 50 nm thick C_{60} layer to provide good energy contrast for the implanted muons. The depth profile was calculated before performing the experiment using *TRIM.SP* in order to identify the desired energies that are needed to target specific layers within the sample as shown in figure 5.6a. The magnetometry measurement of the equivalent sample is also shown in figure 5.6b.

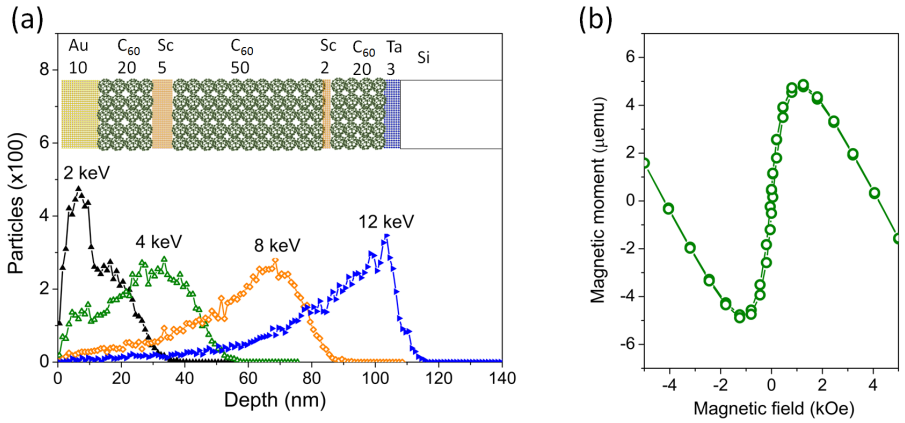

Figure 5.6: *(a) Low energy muon implantation profiles of the multilayered system for muons tuned with different kinetic energies to target specific layers, calculated using TRIM.SP. Sample structure: Ta(3)/C_{60}(20)/Sc(2)/C_{60}(50)/Sc(5)/C_{60}(20)/Au(10). Inset: Schematic of the sample stack used for μSR experiment. The Sc layers are separated with a 50 nm thick C_{60} layer to provide good energy contrast. (b) Raw magnetisation data of the sample measured via SQUID magnetometry at room temperature showing an emergent magnetism.*

Figure 5.7 shows μSR time spectra collected at 250 mK in a zero-field (ZF) state where no external field was applied to the samples. The figure shows the depolarisation of muon particles at various depths (energies) from 2-12 keV. These particles can

be implanted at depths ranging from few nanometres to hundreds of nanometres. At an energy of 2 keV and 4 keV where the implanted muons probe the gold layer and the thick top Sc (10 nm) layer respectively; the polarisation has a very small loss of about ~ 0.05. The constant depolarisation rate at both 2 keV and 4 keV is a feature implying that the thick Sc interface behaves in the same way as the bulk where there is no sign of magnetism. However, the spin-polarised positive muons implanted at 8-12 keV that stop at the thin Sc(2 nm)/C_{60} interface exhibited a rapid loss in polarisation from an initial value of 0.18 to a value of ~ 0.02. The rapid loss occurs in the thin Sc/C_{60} interface but not in the thick Sc/C_{60} interface. This gives indication of the presence of local magnetism that affects the precession and hence the polarisation of the implanted muons.

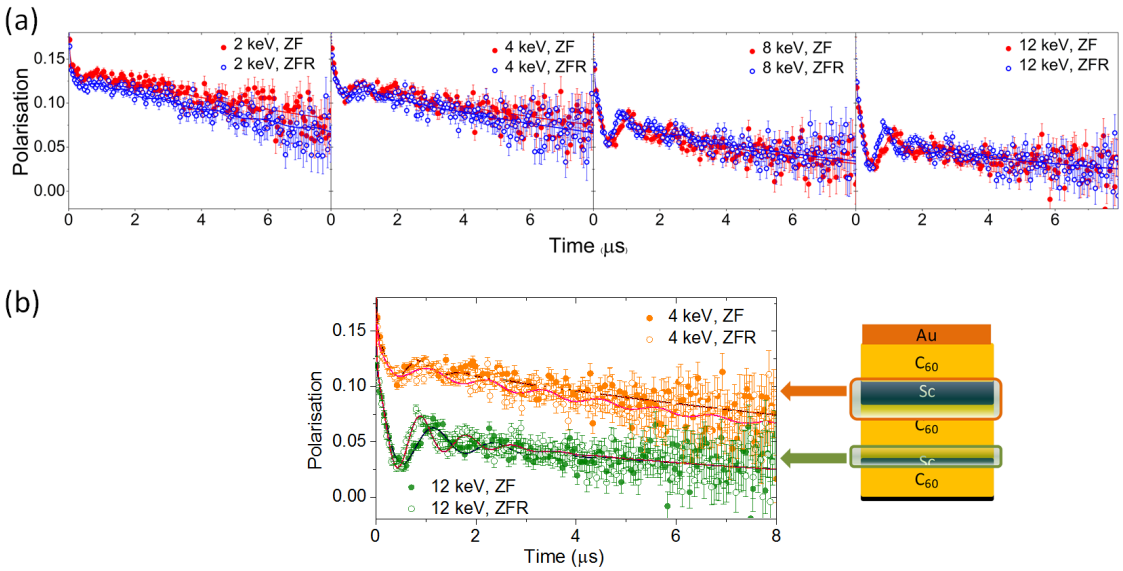

Figure 5.7: *Low-energy muon spectroscopy (μSR) spectra showing the asymmetry (depolarisation) of the muon particles in a time frame of 8 μs for a multilayered system of Ta(3)/C_{60}(20)/ Sc(2)/C_{60}(50)/ Sc(5)/C_{60}(20)/Au(10). The spectra are for four energies targeting different layers within the sample. The data with open circles were taken in the zero field remanence (ZFR) state whereas the closed circles in the zero field (ZF) state. (b) Comparison between μSR time spectra of 4 keV and 12 keV energies where the thick top Sc layer and thin bottom Sc layer are located respectively. Right: schematic of the sample structure pointing to the top and bottom Sc layer where the μSR spectra of these layers are studied.*

To extend the scope of the investigation, μSR spectra were also measured in the zero-field remanent (ZFR) state. In this state, an external field of 500 G is applied to magnetise the sample but it was removed during the measurements; remanence of $\sim$ 0.3 Oe. This allows enhancement in the local field in the area of interest, therefore better resolution of muon depolarisation will be obtained. In the ZFR state, the μSR spectra clearly revealed different oscillations as the implanted muons approach the thin Sc layer, whereas the oscillations remained nearly the same for the top layers. This can be seen at both 2 keV and 4 keV spectra as presented in figure 5.7. It showed no pronounced change in the oscillations as the muons probe the gold layer and the thick top Sc layer. However, there is a noticeable shift in the oscillation at 8 keV and it gets even larger at 12 keV, implying the presence of magnetic moments at these penetration depths.

To gain better understanding and to distinguish between bulk and thin layer contributions to the μSR signal, the data in figure 5.7 was fitted using equation 3.9 that describes the time dependence of the muon spin-polarisation behaviour when it is subjected to a field. The extracted frequency and amplitude of the oscillations were plotted in figure 5.8 as a function of implanted muon energy. At zero-field, the μSR spectra showed an unexpected oscillation of 1.1 MHz. The amplitude of this oscillation increases as muons approach the bottom interface and it peaked at 10-12 keV where the thin Sc layer is located. The amplitude of the signal decreases when the implanted muon energies exceed 12 keV and are implanted away from the thin Sc interface. The observed oscillation could be attributed to the interfacial magnetisation, as was the case for Cu (section 4.2.2.2). The results also ascribe changes in the frequency as a function of the Sc thickness when it is measured in the zero-field remanent state. This is indicated by an additional frequency of 0.85 MHz that has no contribution in the thick Sc layer (blue data in figure 5.8a); as no local magnetism is expected at the interface with thick metallic layer as shown in 5.2.1.2. The amplitude of this frequency increases as the muons probe the bottom interface and show a maximum signal at 12 keV where the thin Sc interface is located. The fit of the 0.85 MHz signal to the layer contributions, as presented in the inset of figure 5.8, indicates that the layers at the bottom interfaces contribute more strongly. The asymmetry tail displays a progressively smooth decrease as the energy of the implanted muons increases; this means the dominant contribution

to the signal arises from spin ordering that is localised at the bottom Sc/C_{60} interface. By considering the results shown in figure 5.8a and b, it may be deduced that the only interface involved in the magnetic signal is the bottom one where the Sc layer is thin.

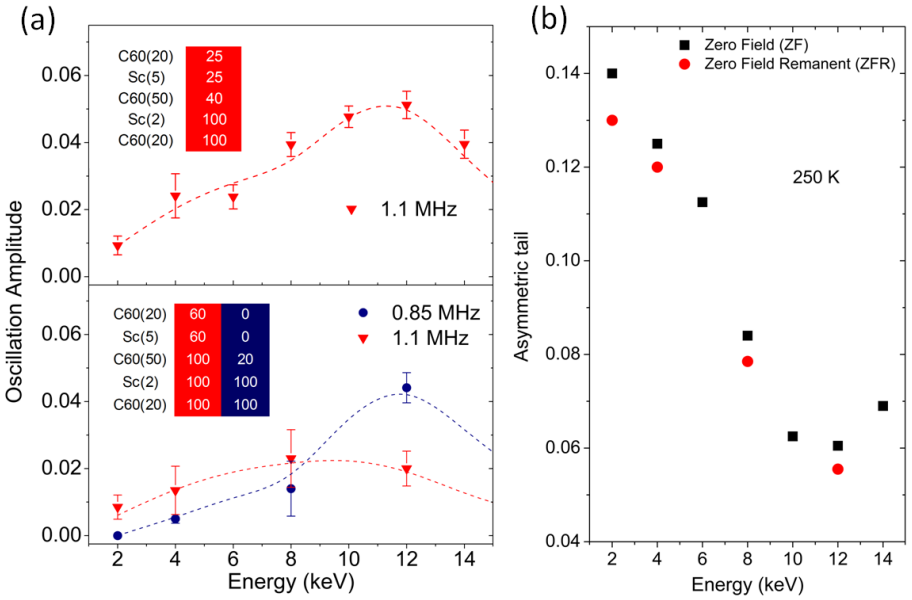

Figure 5.8: *(a) Amplitude of the muon oscillation at zero field (1.1 MHz, top) and zero field remanence (1.1 MHz and 0.85 MHz, bottom) in the energy range 2 keV to 14 keV. The inset shows the percentage of each layer that contributing to the signal where 100% indicates the whole of the layer is contributing and 0% is not contributing. The dotted lines are the fit corresponding to the layer contributions to the oscillation signal as shown in the inset. The strongest signal is assigned to the bottom Sc(2)/C_{60} interface. (b) Muon spin polarisation asymmetry tail of the oscillation as a function of implanted muon energy showing a reduction in the amplitude as the bottom interface is probed, here the bottom Sc(2)/C_{60} interface is contributing more.*

It is also important to consider the muonium states that are associated with the presence of C_{60} and rule out any possible muonium contributions to the emergent magnetism. To address this issue the muon spin depolarisation was investigated at a low temperature of 20 K as a function of implanted muon energy, see figure 5.9 for μSR spectra at different energies from which the frequencies due to the oscillation were extracted. The signal allows the frequency oscillations of C_{60} muonium, 1.2 MHz, 7.4 MHz and 8.6 MHz, which is similar to the oscillations observed in C_{60}/Cu. The

amplitude of these frequencies is shown as a function of the implanted muon energies in figure 5.9. The oscillation amplitude of the muonium signal is expected to follow the C_{60} contribution, i.e. the muon particles stopping at C_{60} layers, and raises rapidly crossover energy scale. However, the muonium signal is almost constant for all energies. The fact that the muonium signal is constant and does not follow the C_{60} contribution (as shown by the blue dotted line) suggests the presence of local magnetism may arise from inside the sample and prevents the muonium formation.

All the data presented here appears to be consistent with the local magnetism originating at the thin bottom Sc interface rather than the thick Sc interface. This observation lends strong support to the idea of the charge transfer and screening effects of free electrons in metals. The thick layers are more resistive to the charge transfer hence no spin ordering was observed at the thick Sc interface.

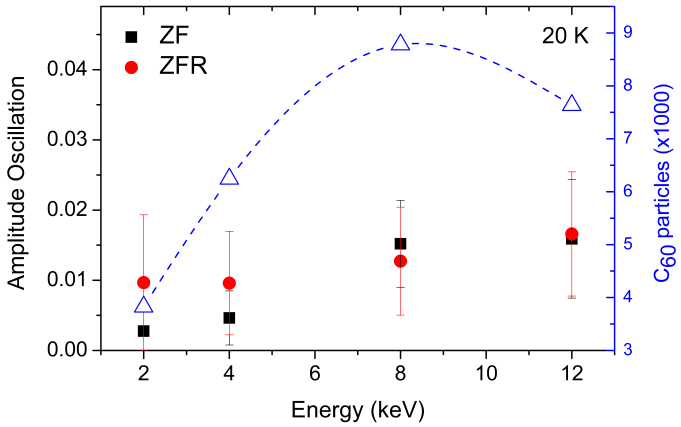

Figure 5.9: *Low temperature measurements at 20 K, of the amplitude of oscillation for the three muonium frequencies of C_{60} at different energies, the blue line is the contribution of the C_{60} layers to the signal.*

5.2.3 X-ray absorption spectroscopy and magnetic dichrosim

The critical role played by hybrid interfaces in transforming the paramagnetic element Sc into a magnetic material when placed in contact with C_{60} molecules is elucidated by magnetometry and low energy muon spectroscopy studies. However, the resolution

of these techniques is not high enough to distinguish the contribution of carbon in the emerging spin ordering. XAS, on the other hand, by means of XMCD is used here to study the changes in carbon due to interfacial effect with Sc. The measured samples are multilayers of C_{60} molecules and Sc with different thicknesses of the Sc layers; 2.0 nm and 4.5 nm. An aluminium cap was used to allow X-ray penetration to the Sc/C_{60} interfaces, as the technique is surface sensitive. The normal measurement geometry consists of the sample plane in a perpendicular orientation to the photon beam whereas the field is applied parallel to the photon beam. This geometry was changed so the angle of incidence of the photon beam was set to 45^o relative to the sample normal. Rotating the sample plane at grazing angle allows the magnetisation to be aligned to the polarisation vector of the beam and maximise XMCD intensity. The sample was magnetically saturated out of plane using a field of 1 T. Figure. 5.10 shows a comparison of the two XAS spectra of two [C_{60}(15 nm)/Sc(x)]$\times$4 samples with different Sc layer thicknesses (x = 2.0 nm and 4.5 nm). These samples were measured at incident photon energies corresponding to the carbon (C) K-edge where the excitation of electrons from a core level to an unoccupied level is studied. Here XAS is also denoted as near-edge X-ray-absorption fine structure (NEXAFS) because the excitation energy is in the region of $\sim$50 eV of the absorption edge allowing more electronic and geometric information to be obtained. The averaged circularly-polarised XAS spectra at the C K-edge was recorded at room temperature; the intensities of which are normalised to the maximum intensity. The XMCD spectra of two samples obtained by taking the difference between the normalised XAS spectra for the two polarisations over the same edge is denoted by the red line and shown in the bottom panel of figure 5.10. The spectral features observed in the region 283–289 eV are assigned to the C $1s \rightarrow \pi^*$ transitions whereas the broader features above the ionisation threshold of 290 eV are attributed to the C $1s \rightarrow \sigma^*$ transitions.

As expected, the hybridisation between the p orbital of C_{60} and the 3d band of Sc leads to a sizable interfacial magnetic moment that is revealed as a difference in the absorption between left and right circularly polarised X-rays at the C K-edge. These XMCD results prove the existence of spin-split states in carbon; otherwise, the XMCD line shape would have been completely flat. The XMCD peaks observed in both samples around photon energies $\sim$284.1 eV and $\sim$287.5 eV are resulting from the l C $1s$

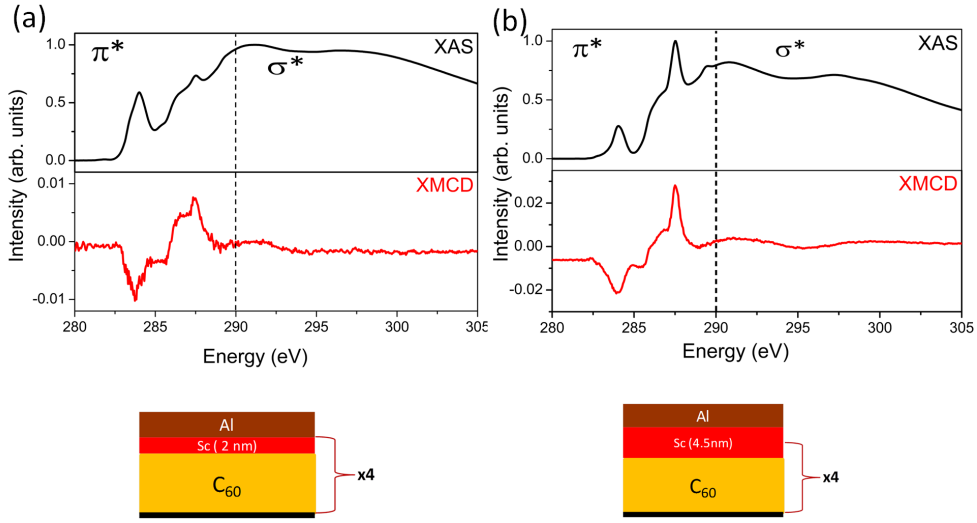

Figure 5.10: *Near edge X-ray absorption of Sc/C_{60} multilayered system. (a) top: room temperature normalised XAS (black) spectrum of Ta(3.5)/[C_{60}(15)/Sc(2)]×4/Al(5), thicknesses in brackets in nm, at the carbon edge obtained by averaging signals for positive (h^+) and negative (h^-) helicity was measured in normal incidence geometry. bottom: Corresponding XMCD (red) intensity obtained by taking the difference between the XAS positive and negative helicity. (b) show the same measurements to (a) but with thicker Sc layer of about 4.5 nm measured at 300 K with 1 T field applied in-plane to the sample and 45^o grazing incidence. Bottom; Schematic of the samples structure.*

/ π^* transition to the lowest unoccupied molecular orbital (LUMO) and other higher energy (LUMO) π^* orbitals [110; 127], further details about molecular orbitals will be discussed later in this section.

This study also showed that the magnetic response observed in the XMCD spectra for both samples is obtained only from transitions of the *1s* electron into the π^* states whereas the transitions into the σ^* states shows much weaker magnetic signal. This gives an indication that the only spin-polarised hybridisation effect occurs between C $2p_z$ orbitals and the Sc 3d band as shown by the emergence of magnetism. The emergent magnetic effects observed in the XMCD experiment, can be quantified by estimating the XAS intensity contribution from the C K-edge. These effects can be evaluated by calculating the C K-edge XMCD intensity to the total intensity of the XAS obtained from the two different photon polarisations at specific transitions. This

results in a dichroism intensity of about 5% of the total XAS intensity at the C K-edge for the x = 4.5 nm sample, where x is the Sc thickness. The C K-edge XMCD signal is particularly strong, especially considering that it originates from a non-magnetic element, and reflects the significant degree of hybridisation between the p_z electronic states and the 3d metallic bands. Similar results have been shown in a number of previous experimental studies for magnetic systems; e.g., 5% for graphene/Ni(111) [128], 3% for C_{60}/ Fe(001) [129] and 1% for C_{60}/ Fe_3O_4 [130]. For the x = 2.0 nm sample, the dichroic signal was about 1% at the C K-edge and it is relatively weak comparing to the x = 4.5 nm sample, however, this signal is expected to be higher. The measurement geometry could be the reason; XMCD signal is proportional to the magnetisation vector and to the photon polarisation vector [131]. The x = 2.0 nm sample was measured at normal incidence where the easy magnetisation axis is in plane to the sample surface due to shape anisotropy. Measuring in an external field of 1 T perpendicular to the sample will rotate the magnetisation vector parallel to the polarisation vector but the sample behaves paramagnetically with nearly zero remanence and exhibits a much smaller XMCD intensity. However, if the magnetisation vector is tilted by 45 degree, in grazing incidence geometry, a component of the magnetisation vector preferred along the polarisation vector which increases XMCD intensity which is the case for the x = 4.5 nm sample, as shown in figure 5.10. The observed weak dichroic signal for the x = 2 nm sample could be related also to the measurement conditions and more statistics or studies may be needed to investigate the strength of the magnetic signal. The study disregards the strength of the dichroism signal present in the samples but gives strong support to the role played by the hybrid interfaces in emergent magnetism.

To further understand the emergent magnetism in these structures, the molecular electronic structure needs to be considered. Due to π-bonding and icosahedral geometry of C_{60} molecules, their electronic structure is characterised by delocalised and highly degenerate orbitals. Thus the XAS spectrum of the molecule in the ground state features narrow, easily identifiable molecular orbitals[127]. Any perturbation on the electronic structure of the molecule due to interactions with different metals can be observed effectively by XAS. Extensive experimental work about the electronic structure of C_{60} was investigated by XAS [110; 132–136]. The NEXAFS of solid C_{60} is found to exhibit two distinctly pronounced resonances that are associated with the

LUMO of the molecules and separated by the C *1s* ionisation potential (289.5 eV), see figure 5.10. The sharp and most pronounced resonances observed below this energy are named π^* states. These orbitals are related to unoccupied orbitals directed perpendicular to the molecular sphere, while above the ionisation potential the resonances are described alternately as σ^* states which are distigushed by broader features [136].

The XAS spectrum for solid C_{60} has a first peak at 284.5 eV which corresponds to the C *1s* transition to the LUMO. This is followed by three peaks at 286.1, 286.7 and 288.3 eV identified as LUMO+1, LUMO+2, and LUMO+3, respectively, and corresponding to the excitations to other π^* orbitals. The energies of these resonances and the assigned orbitals are based on the Hückel molecular orbital theory on C_{60} [137; 138]. At the interface between C_{60} molecules and the paramagnetic transition-metal Sc, these assigned molecular orbitals experience changes due to orbital perturbations associated with charge transfer and hybridisation of the π -electronic states with the 3d band of the metal. These changes could appear as a shift in the photon energies or broadening of the molecular electronic structure due to the interfacial bonding between C_{60} molecules and the Sc metal. The NEXAFS spectra presented in figure 5.11 shows considerable changes in the molecular orbitals compared to the solid C_{60} spectrum reported previously [139; 140]. The energies of the molecular orbitals are shifted by about 0.3 eV compared to the literature values, this may be due to a small error in the photon energy calibration or metal charge transfer effect. The room temperature spectrum showed broadening in both the π^* and σ^* features. This broadening is assigned to hybridisation between the molecular orbitals of C_{60} and the Sc 3d band where these features become progressively broader as the hybridisation increases. This has been previously observed but with different metallic substrates such as Al and Au [133; 135]

As discussed earlier, the NEXAFS spectrum for C_{60} has distinctive features correlated to energy levels for each molecular orbital. However the LUMO+1 and LUMO+2 resonances on the x = 4.5 nm sample merge into a single peak and are shifted to a higher energy LUMO peak. This phenomenon is coupled with the fact that strong hybridisation effects occur at the Sc/C_{60}interface [129; 135]. The LUMO peak of the sample is also accompanied by an asymmetric line shape associated with the appearance of a small shoulder at an energy of 283.3 eV. This can be interpreted as a partial occupation

of the LUMO due to charge transfer from Sc to C_{60} in analogy with a previous study for C_{60} on Fe [129]. This agrees with a photoemission spectroscopy (PES) study of C_{60} on Cu [110]. The comparison of the C*1s* absorption spectra of Sc/C_{60} and solid C_{60} reveals that strong hybridisation and charge transfer play a major role in altering the electronic structure of C_{60}, and thus correlated emergent spin ordering was clearly observed in the absorption spectra with different helicity.

The 4.5 nm Sc sample was then cooled in 1 T to 4 K. The carbon NEXAFS spectrum is displayed in the bottom panel of figure 5.11b. In order to compare spectra taken at different temperatures, the lineshapes were fitted to Gaussian-Lorentzian functions to extract the energy and width of these features. Figure 5.11b shows the fitting of the NEXAFS spectra at both 300 K and 4 K. The spectrum at 4 K is dominated by broadened peaks indicating orbital hybridisation, similar to the measurements at room temperature. Unlike the room temperature spectrum, the peaks are more distinctive. The peaks at σ^* resonance seem to be more pronounced at low temperature where they are much attenuated at room temperature. This is could be because C_{60} molecules experience a phase transition from orientationally disordered face centered cubic structure to simple cubic orientationally ordered structure as the temperature drops below 90 K, although a small amount of static disorder is still present and not completely frozen below this temperature [58]. The transformation to a highly ordered system leads to an increase in the symmetry of the molecule and a reduction of the perturbations in the molecular orbitals and thus modifies the carbon NEXAFS spectrum. The opposite behaviour has been observed in annealed C_{60} systems where the features are washed out as the temperature increases due to the perturbation of the molecular orbitals by annealing and C_{60} decomposition [141]. At 4 K, there is a slight shift in the energy of the sample which reflects the changes in the electronic and physical structure between C_{60} and Sc. The dichroism signal at 4 K is stronger than the one observed at room temperature by 18% and new features appear. The lack of rotational motion as the individual C_{60} molecules are locked into specific orientations and the strong ferromagnetic signal at low temperatures may explain this strong dichroism signal.

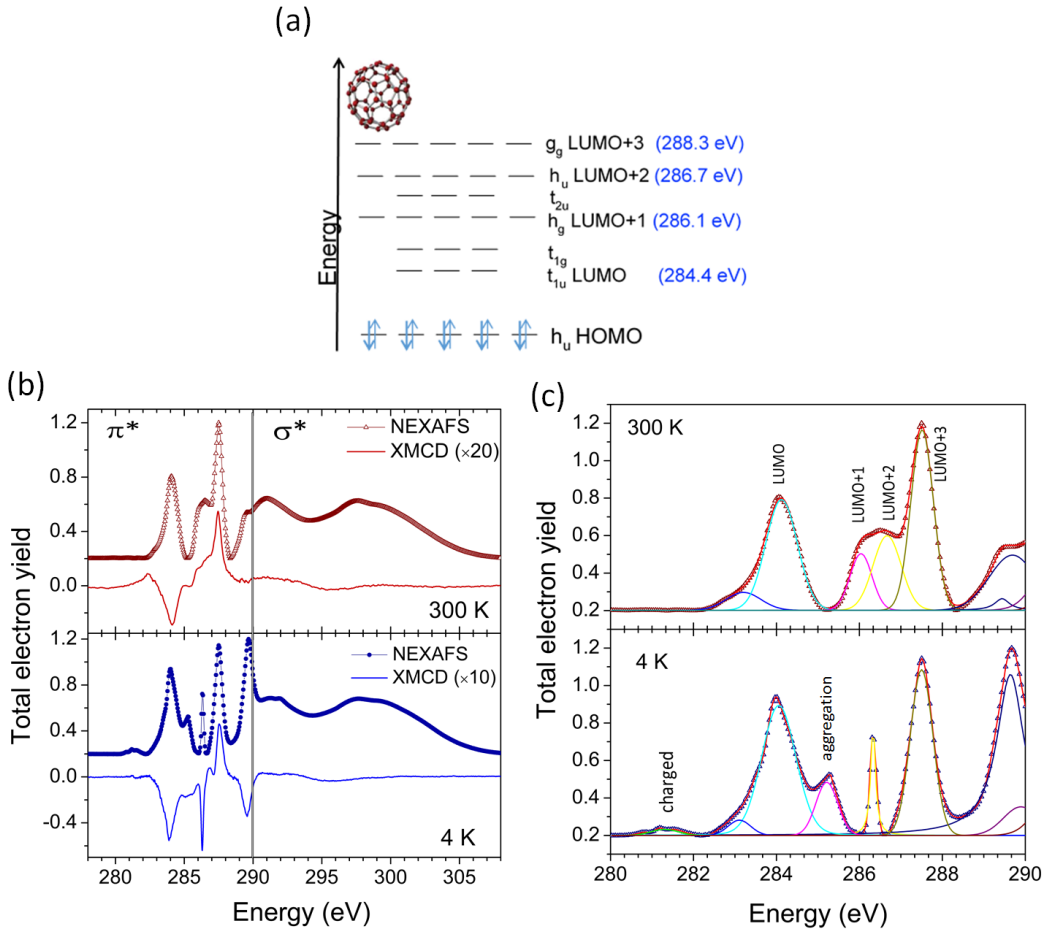

Figure 5.11: *(a) Schematic representation of the energy levels for unoccupied states of C_{60} based on Hückel molecular orbital theory [138; 142]. To the right are the transition energies of C_{60} molecule for the 1s core in Cs symmetry. (b) A comparison between the C 1s NEXAFS of unoccupied states for Ta(3.5)/[C_{60} (15)/Sc(4.5)]×4/Al(5) sample at 300 K (top panel) and 4 K (bottom panel). The corresponding NEXAFS peaks are labelled according to the energy transition from C 1s where the states above 290 eV present σ^* resonances and below this energy are the π^* resonance. The 285.8 eV peak is attributed to C_{60} aggregation [143] whereas the 281.3 eV peak is the charged C_{60} peak. The solid curve indicates the XMCD signal between the positive and negative helicity NEXAFS. Normalised to the high intensity peak and substract the background contribution. (c) The fit of the spectral line in (b) employing Gaussian-Lorentzian functions, where parameters such as line position, height and half width can be extracted. The open symbols are the experimental data and the solid lines are the fitting curves, the solid red line is the total fit whereas the other colour correspond to individual peak fit.*

5.3 Conclusion

This chapter has addressed the role played in the emergent magnetism by charge transfer and hybridisation between the molecular orbitals of C_{60} and the 3d band of paramagnetic transition metals Mn and Sc. Similar to Cu/C_{60} system, the magnetometry measurements for both Mn and Sc samples showed emergent magnetic ordering at room temperature. The dependence of magnetisation on the metallic layer thickness was also studied. The bulk properties of both systems dominates and the magnetisation is quenched as the metallic layer becomes thicker. The Mn/C_{60} system exhibited similar behaviour to the Cu/C_{60} system, where the magnetisation disappeared when the metallic layer became thick enough for the bulk properties to dominate. Also, the magnetisation experienced quenching when the metallic layer was not continuous. The effect extends deeper in paramagnetic Mn/C_{60} film but diamagnetic Cu/C_{60} shows peak magnetisation 3- 4 times stronger than the paramagnetic system within the same thickness range. In contrast, the Sc/C_{60} multilayers reveal different behaviour as the Sc layer became thinner. The magnetisation increased even down to 0.5 nm thin Sc layer and that could be wetting properties of C_{60} by Sc which maintain the continuity of the film and hence the magnetisation or superparamagnetic-like behaviour. Further analysis of the data showed an oscillatory manner of the thickness dependence of the magnetisation. The formation of QW states may be the possible mechanisms to explain this behaviour.

The goal of using LE-μSR was to perform depth profile and reproduce the thickness results from magnetometry measurements in order to confirm that the observed magnetic ordering is a property of the thin film and not a thick layer contribution. As expected, it gave further support for the thickness dependence observed by the magnetometry and confirms the role of electron screening of the bulk-like samples.

The need to understand how the emergent interfacial magnetic moment is correlated to the change in molecular orbitals of C_{60} interfaces with metal, lead us to study the electronic and magnetic structure of the carbon edge using element specific techniques; XAS and XMCD. There was a sizable XMCD signal of about 5% of the XAS intensity observed in the C K-edge, reflecting the degree of mixing between C p_z and

Sc 3d derived states at the interface. There was a significant change in the molecular orbitals accompanied with broadening and energy shifts of the unoccupied molecular orbitals in the C_{60}. This observation of the change in molecular orbitals, i.e. electronic structure, is evaluated based on the hybridisation and charge transfer change due to the interfacial effect. Furthermore, the comparison of the NEXAFS spectra at different temperatures showed pronounced changes in the molecular orbitals that agrees with the fact that the motion of the molecular orbitals are locked with specific orientation. The re-orientational dynamic behaviour of C_{60} molecules undergoes a phase transition from an orientationally disordered structure to an orientationally ordered structure as the temperature decreases. This perturbs the molecular orbitals and hence drives modification to the electronic structure.

CHAPTER 6

Transport measurements

6.1 Introduction

Due to molecular charge transfer, the emergent spin ordering has a drastic effect not only on the magnetic (presented in chapter 4 and 5) but also on transport properties. Transport measurements are very sensitive to the spin ordering and can provide information about the behaviour of conduction electrons scattering by localised spins which cannot be easily obtained using other techniques.The sensitivity of transport measurements, such as Kondo and weak localisation (WL), allows the detection of very small concentrations ($\sim$ 0.1 ppm) of magnetic spins within a sample. Therefore, measuring the effect of WL and Kondo will help us satisfy the primary goal of this work; to study the role of molecular interfaces in generating magnetism in non-magnetic systems. It is expected that one might observe an increase in the spin-scattering rate at the metallo-molecular interfaces. To aid this analysis, the theory of Hikami et al. (as described in 2.4.2) and power law expansion are used to study the spin dependent scattering due to magnetic spins on the conduction electrons.

In the present chapter, the behaviour of the resistivity as a function of magnetic field and temperature will be investigated in thin Cu films with and without C_{60}. A comparison of experimental data with the theory that yields information on spin dependent scattering will be discussed.

6.2 Spin dependent scattering in Cu/C_{60} system

The studied samples are thin films of Cu and Cu/C_{60}. They were deposited using a high purity Cu source (99.9999%) with the structure Cu(2.5 nm)/C_{60}(x nm)/Cu(2.5 nm), where x is 0, 1 and 10 nm; the 1 nm film here indicates a discontinuous film or "dusting layer". To prevent sample oxidation, a 2 nm thick capping layer of Al was deposited which becomes an insulating Al_2O_3 under ambient conditions. In order to keep the consistency of the growth conditions and ensure that no contamination could occur while moving the shutter from one position to another, the pure Cu film was deposited following the same deposition procedure as the Cu/C_{60} samples. More specifically, the 5 nm Cu sample was not deposited all at once; it was deposited in the same way as the Cu/C_{60} samples, where a 2.5 nm layer was deposited first then the shutter was moved

away and then returned back to deposit the second Cu layer. In terms of the measurement setup, the electrical contacts were made using wire bonding. Four-terminal DC resistivity measurements were performed by biasing the sample with a current of 1 mA using a Keithley 6221 Sourcemeter and measuring the output voltage with a Keithley 2182 Nanovoltmeter in a ^{4}He cryostat. The contact geometry is shown in the inset of figure 6.1a. The magnetotransport properties were measured in magnetic fields from +8 T to -8 T applied both perpendicular and parallel to the films.

Figure 6.1a shows the temperature dependence of the sample resistivity for the studied films. The samples show a metallic behaviour where the resistivity decreases as the temperature is lowered, but below 20 K the resistance rises and continues to do so down to 1.4 K, the base temperature of the cryostat. The logarithmic dependence of the resistivity on the temperature for the samples is plotted for temperatures below 25 K for clarity, as shown in figure 6.1b. It clearly shows the upturn behaviour where the resistance starts to increase with decreasing temperature below a specific temperature. The existence of Kondo impurities (Cr, Fe, Ni, etc.) can be responsible for the upturn in resistivity at low temperatures [59]. This phenomenon is associated with the screening of the spins of the impurities by the conduction electrons. Decreasing the temperature means that more conduction electrons participate in the screening process which enhances the scattering of electrons by the screened impurity and results in a logarithmic increase in resistivity, similar to the trend shown in figure 6.1b. This reveals the presence of magnetic impurities in the Cu target used (99.9999% Cu) which caused the upturn, Kondo behaviour.

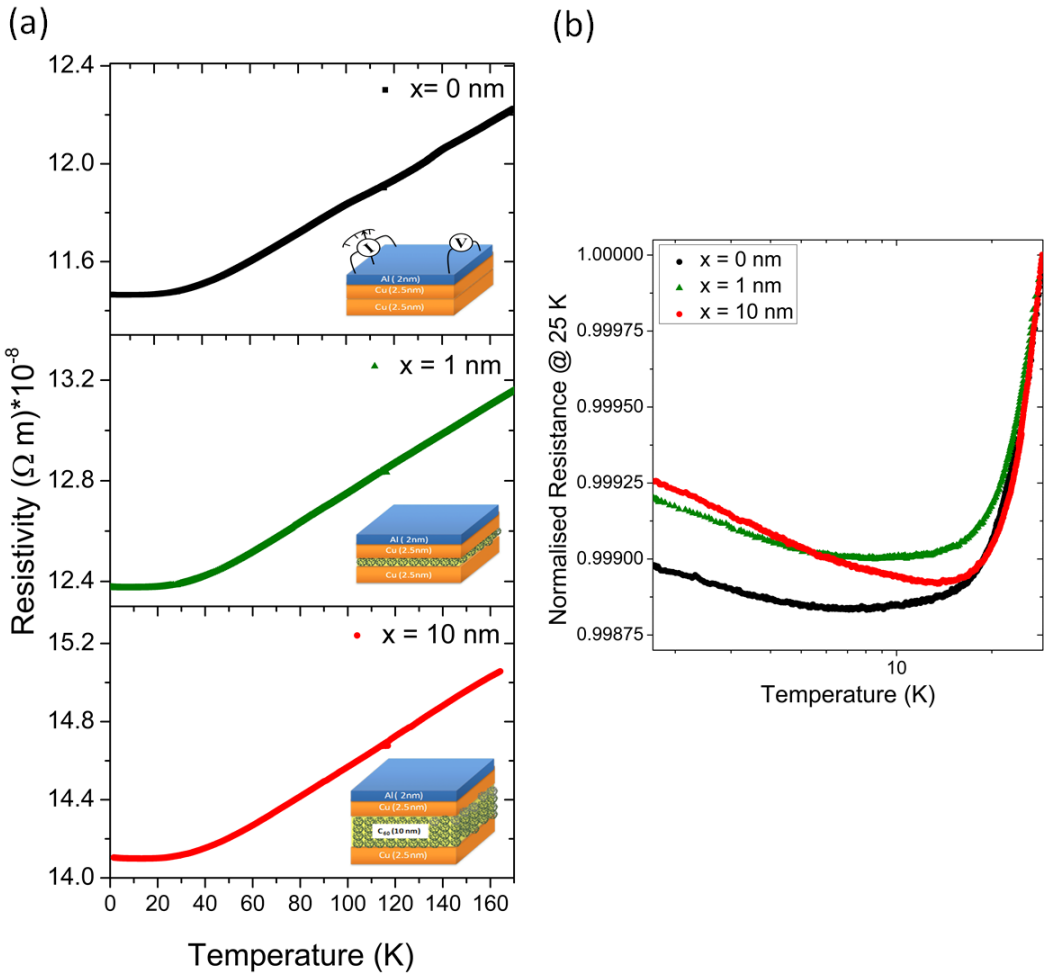

Figure 6.1: *(a) Temperature dependence of the resistivity for samples with the structure Cu(2.5)/C_{60}(x)/Cu(2.5)/Al(2) where x = 0, 1 and 10, thickness in nm. The 1 nm layer of C_{60} here is considered to be a dusting layer where the molecules are randomly distributed in between the Cu layers. The inset shows a diagram of the sample structure with four-terminal contact geometry. (b) The same data as in (a), plotted on a logarithmic scale in the low temperature region, emphasizing the contrast between the upturn temperature of different investigated samples. The resistance has been normalised to provide clear comparison of the temperature behaviour.*

The Cu/C_{60} samples in this study are expected to follow the same trend because the same pure target was used to deposit Cu layers. Assuming that the concentration of magnetic impurities for all samples is equal then the characteristic temperature T_{min} (the temperature at which the minimum resistivity occurs) should be the same. However, this is not the case for the samples with C_{60}. The effect is more pronounced for the sample with 10 nm thick layer of C_{60} (x =10 nm), T_{min} is shifted to a higher temperature range. The fact that T_{min} is higher for the x = 10 nm sample is a strong indication that the concentration of local spin moments is higher in this sample because T_{min} is roughly proportional $c^{1/5}$, where c represents the concentration of the magnetic atoms [59]. Accordingly, the concentration of local spin moments for the sample with 10 nm C_{60} is approximately 35 times larger than the one for the Cu film without C_{60}. This significant amount of magnetic moments cannot be explained only by the Kondo impurities in the Cu layer, but it can be related to other sources of magnetic spins generated in the sample. The charge transfer and hybridisation between the molecular orbitals of C_{60} and the 3d band of Cu can lead to an emergent source of magnetic moments which enhances the scattering of the conduction electrons. Also, the depth of the minimum, defined as the difference in the resistivity values between T_{min} and the lowest temperature at which the measurement is performed ρ_{min}-$\rho_{1.6K}$, exhibits proportionality to the concentration of magnetic atoms, c [59]. This provides more evidence for the presence of extra magnetic moments, whereby the sample with a 10 nm C_{60} layer has a larger depth compared to other samples. The values for Kondo parameters are given in table 6.1.

Table 6.1: Kondo parameters which are deduced from resistivity measurement in figure 6.1 and explained in the text above. ρ is the resistivity. $(T_x/T_0)^5$) shows the increase in the amount of local spin moment relative to the pure Cu sample (x = 0 nm; T_0)

Sample	x (nm)	T_{min} (K)	$\rho_{1.6K}(10^{-8}\Omega)$	ρ_{min} $(10^{-8}\ \Omega)$	ρ_{min}-$\rho_{1.6K}$ (10^{-11})	$\%\left(\frac{\rho_{min}-\rho_{1.6K}}{\rho_{min}}\right)$	$(T_{minforx}/T_0)^5$
1	0	6.85	11.466	11.464	1.75	0.015	1
2	1	7.74	12.376	12.373	2.78	0.023	1.84
3	10	13.97	14.104	14.099	4.99	0.0035	35.28

As well as the interpretation based on the Kondo scattering, an increase in resistivity below a characteristic crossover temperature has also been found in ultrathin metallic films such as Cu, Mg, Ag and Au with thicknesses less than 20 nm [144]. This behaviour can be interpreted considering the WL effect which occurs in two-dimensional disordered systems at low temperatures [145]. It results from the quantum interference between the electron waves. The backscattered waves could experience constructive interference (WL) that enhances the backscattering probability of electrons or destructive interference (weal anti-localisation; WAL) due to inelastic scattering that destroys the coherence of electron waves. An increase in resistivity takes place as the temperature decreases, similarly to the behaviour observed in the Kondo mechanism [59; 146]; details about this theory are in section 2.4.1.

The DC electrical characterization results alone cannot determine the transport mechanism that is responsible for the behaviour of the conduction electrons at low temperature in the Cu thin film and the equivalent films with C_{60} layers. However, the resistance behaviour under the influence of a magnetic field can provide evidence for the presence of WL effects. Figure 6.2 shows the resistance dependence on the magnetic field in both parallel and perpendicular configurations, respectively, in the temperature range between 1.6 K and 23 K. The measured $MR = [R(H) - R(0)]/R(0)$ for all samples is negative at high fields and positive at low fields. It also exhibits large anisotropy depending on the applied magnetic field orientation, either parallel or perpendicular to the film plane. The negative MR is expected because increasing the magnetic field due to Lorentz force destroys the coherence and gradually reduces the resistance which gives rise to negative MR [147]. Extensive studies have reported negative MR of thin Cu films [148–150] and WL effects in 2D systems was used to describe its origin [63; 144]. In the parallel magnetic field configuration (figure 6.2), the samples show a maximum MR at $H_{\parallel}$ $\sim$1 T which then decreases as the applied field increases. The same behaviour is observed when the magnetic field is applied perpendicular to the film plane. However, the maximum MR in the perpendicular configuration appears at much lower field $H_{\perp}$ $<$0.1 T, compared to the parallel configuration. This means that the WL effect could be suppressed quickly by applying a small magnetic field in the perpendicular direction, but more than ten times the field is needed to

destroy the effect if/when the field is applied in the parallel direction [149; 150].

.

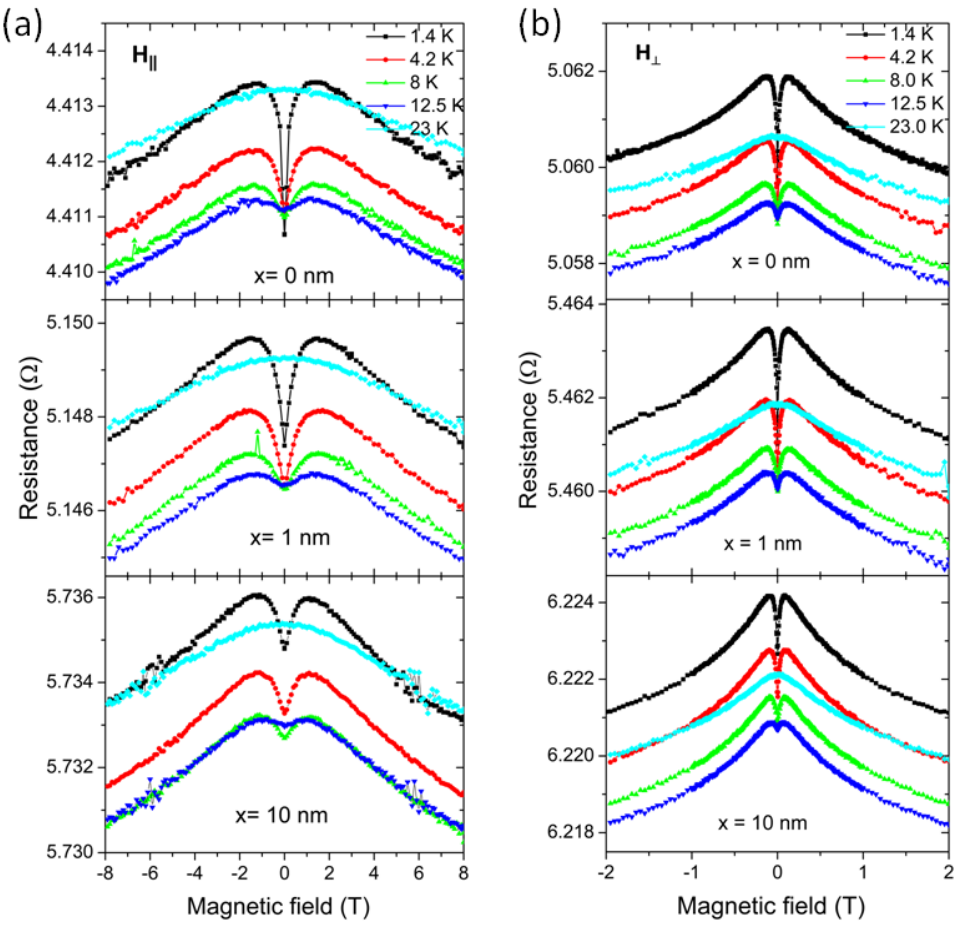

Figure 6.2: *Magnetic field dependence of the raw resistance data at various temperatures ranging from 1.4 K to 23 K for Cu(2.5)/C_{60}(x)/Cu(2.5)/Al(2) where x = 0, 1 and 10 nm. The samples were measured in a magnetic field (a) of ±8 T aligned parallel to the film plane and to the current direction. The field in (b) is applied perpendicular to the plane of the film and varied between +2 T and -2T.*

Figure 6.3a illustrates the MR as a function of temperature for samples of different C_{60} thickness, in both parallel (MR_{max} at 1 T) and perpendicular (MR_{max} at 0.1 T) fields orientations. The MR behaviour exhibits a similar dependence on temperature for both field orientations; however, the MR in the parallel field orientation shows larger values compared to the values obtained from the perpendicular field orientation, as previously observed in Cu films with the same thickness [150].

In order to allow a better comparison of the effect, the MR is also plotted as a function of C_{60} thickness at both 1.4 K and 23 K, above and below the upturn temperature respectively, see figure 6.3b. Firstly, it is observed that for all the samples there is very small MR above the upturn at 23 K. At this temperature electron-phonon and electron-electron scattering are enhanced due to thermal energy, hence the dephasing of electron waves takes place and the WL effect is no longer valid. As a consequence applying a magnetic field will not have an influence on the resistance therefore the MR is negligible. On the other hand, the WL effect is more pronounced at 1.4 K because these scattering mechanisms have a weak contribution at low temperatures and the interacting waves are phase coherent. In particular, at 1.4 K, the system is in the WL regime, where the magnetic field has a strong effect on the resistance. Being a coherence effect, it is more dominant at low temperatures and can be destroyed easily by applying a magnetic field which gives rise to the MR effect. Secondly, by comparing the behaviour of different samples at 1.4 K, it is apparent that both pure Cu and samples with 1 nm of C_{60} exhibit larger MR values in comparison to the sample with 10 nm of C_{60}. This could be attributed to the spin-flip interaction, when magnetic moments are present in the sample that can result in dephasing of the electron waves. The fact that the spin-flip interaction is strongly dependent on the concentration of the magnetic spins [151] suggests the presence of extra magnetic moments in the sample with 10 nm of C_{60} that reduce the phase coherence. This can be attributed to the molecular interfaces which change the state of the spin ordering in the system of Cu and C_{60}.

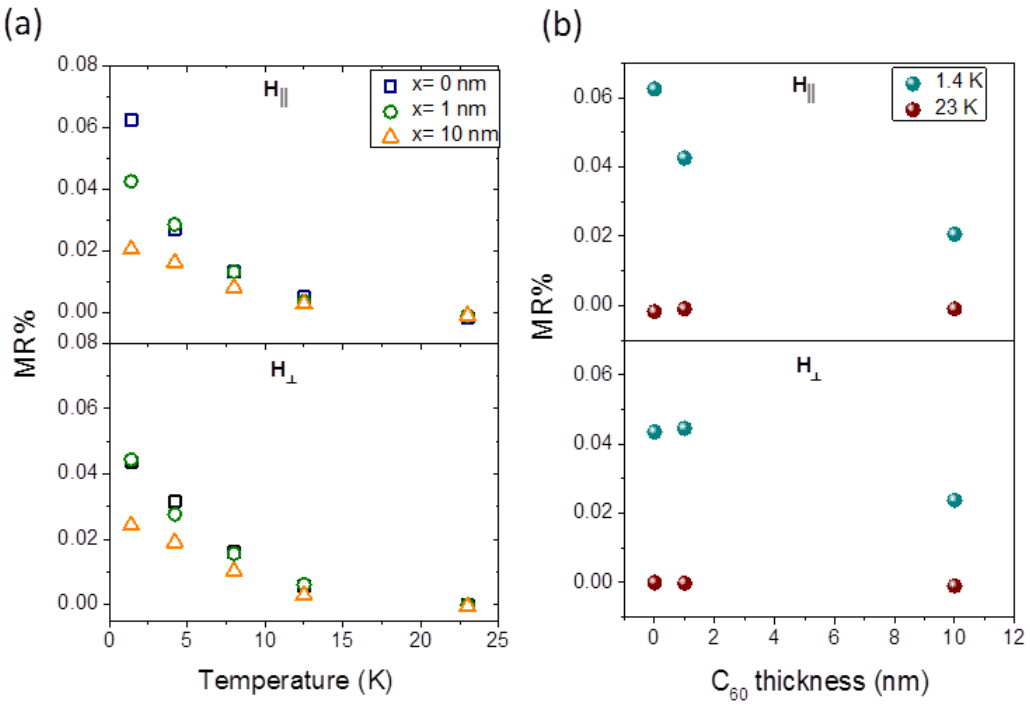

Figure 6.3: *(a) MR of the samples in figure 6.2, Cu(2.5)/C_{60}(x)/Cu(2.5)/Al(2) where x = 0, 1 and 10 nm, as a function of temperature in the parallel field (top) and in the perpendicular field (bottom) orientations. The maximum fields used to calculate the MR are 1 T and 0.1 T in the parallel and perpendicular orientations, respectively. (b) MR is plotted as a function of C_{60} layer thickness (at temperature of 1.4 K and 23 K) in the parallel field (top) and perpendicular field (bottom) orientations.*

To corroborate that the magnetic state is impacted by molecular interfaces, it is necessary to have a quantitative analysis of the magnetic scattering contribution. Theoretical studies [63] and experimental work [62] have shown that the shape of the MR can reveal information about the various scattering mechanisms that suppress the coherence of the conduction electrons in two-dimensional metal films. A combined effect of the inelastic scattering and the magnetic scattering can be described using the theory of Hikami et al. [63]. The same theory is used in order to characterise the emergence of spin ordering in the Cu/C_{60} system by studying the scattering due to the magnetic spins on the conduction electrons. Hikami et al. [63] calculated the magnetoconductance of thin films in the presence of different scattering mechanisms such as

magnetic impurities, spin-orbit coupling and inelastic scattering, where the scattering time corresponding to each mechanism can be determined, as described in detail in section 2.4.2.

The experimental data of the resistance dependence on the magnetic field in figure 6.2b has been plotted in terms of magnetoconductance as displayed in figure 6.4a. Magnetoconductance is calculated with the formula $\Delta\sigma = (1/R_{\square}(H)) - (1/R_{\square}(0))$, where $R_{\square}$ is the electrical resistance referred to a square of the film surface. The magnetoconductance data was then fitted using the theory of Hikami et al. [63] in equation 2.11. It is in very good agreement with the experimental results, as shown by the theoretical fit in figure 6.4a (indicated by red solid lines). The characteristic physical parameters of the samples such as the spin orbit scattering field (B_{so}), spin diffusion field (B_l) and coherence field (B_{φ}), identified in section 2.4.2, have been determined from the fitting. From the equation 2.18, the characteristic length (l_i) corresponding to each characteristic field can be calculated. Figure 6.4b displays the temperature dependence of the characteristic lengths of the same samples with different C_{60} thicknesses (x = 0, 1 and 10 nm). It shows a relatively weak temperature dependence for the spin orbit length and the mean free path for all samples. The coherence time, on the other hand, exhibits an increase as the temperature is decreased to 1.4 K. Interestingly, the x = 10 nm sample shows a similar trend; however, the coherence length is reduced by approximately 80 nm in comparison to the sample without C_{60}. The reduction in the coherence length is attributed to inelastic scattering such as electron-phonon, electron-electron or magnetic scattering. The electron-phonon and electron-electron scattering should yield a smaller dephasing contribution at low temperatures and can therefore be excluded. Only the magnetic scattering remains as a possible source of dephasing scattering at low temperature.

Information about the influence of magnetic scattering on the electron coherence can be obtained using equation 2.10. The data are analysed in a broad temperature range (up to 23 K), which allows for a reliable identification of the three scattering processes that contribute to the dephasing mechanism. The phase breaking rate τ_{ϕ}^{-1} (phase coherence time) which is extracted from equation 2.15 is plotted in figure 6.5

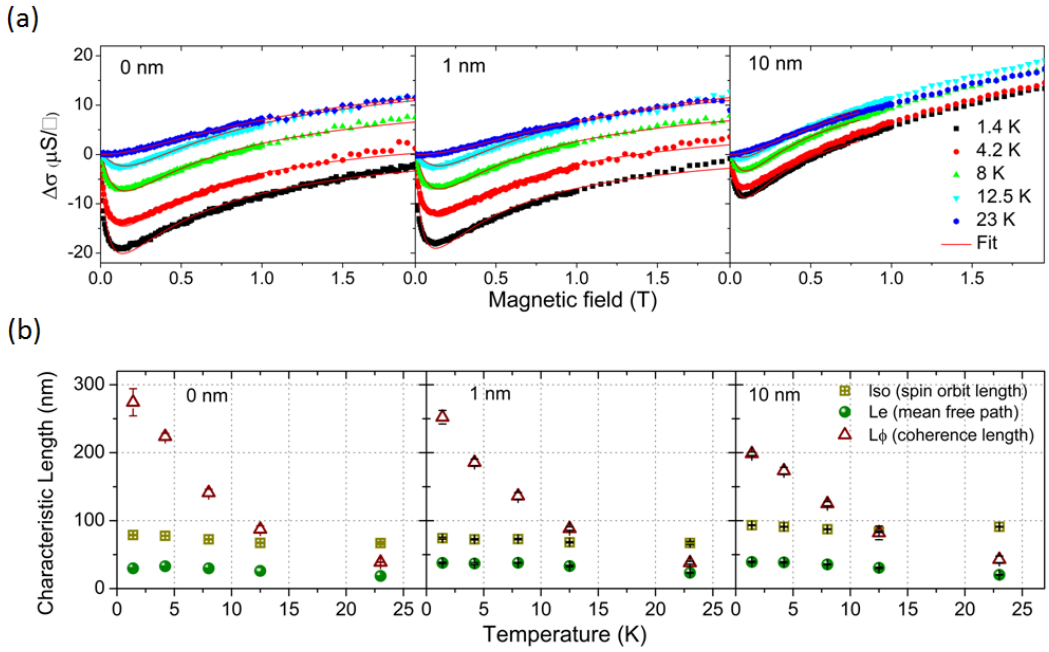

Figure 6.4: *(a) The change in conductivity as a function of magnetic field at different temperatures for Cu(2.5)/C_{60}(x)/Cu(2.5)/Al(2) where the graphs from left to right are for x = 0,1 and 10 nm, respectively. The red line represents the fit using the Hikami et al. theory. (b) The characteristic length (spin orbit length, mean free path and coherence length) as a function of temperature for the same samples as in (a).*

as a function of temperature for the three samples studied. The full curve that fits the data was calculated by the power-law expansion [152; 153]

$$\tau_{\phi}^{-1} = A_0 + A_1 T + A_3 T^3 \tag{6.1}$$

The constant A_0 is temperature independent and represents the scattering caused by magnetic spins. The linear term, A_1, is the scattering corresponding to electron-electron interactions ($\tau_{in}^{-1}\alpha T$) that dominate at low temperatures. The cubic term, A_3, corresponds to electron-phonon scattering ($\tau_{in}^{-1}\alpha T^3$) that dominates at higher temperatures (T>4.2 K). Both the linear and cubic terms are considered as inelastic scattering that are related to the magnetic scattering and phase coherence through equation 2.10.

Figure 6.5a shows the fit of the power-law expansion to the experimental data. The temperature dependence of the resulting phase breaking rate shows an increase in the rate for the Cu samples with a C_{60} layer, compared to the pure sample without C_{60}. This shift indicates an extra contribution from the different scattering mechanisms including the inelastic scattering τ_{in}^{-1} due to electron-phonon and electron-electron interactions as well as scattering due to magnetic impurities τ_m^{-1}. The contribution of these scattering mechanisms can be extracted directly from the power law expansion fit. However, due to the disordered thin-film structure, the scattering rate of the electron-electron interaction is expected to be proportional to $R_\square$. This is because of the elastic impurity scattering for the two-dimensional system [64; 152; 153]. Accordingly, the linear term A_1T, which corresponds to electron-electron scattering, is proportional to $R_\square$ and any small difference in $R_\square$ can considerably affect the phase breaking rate. This dependence can be eliminated by subtracting the linear term A_1T from the experimental data. The corrected $\tau_\phi^{-1} - A_1T$ data is plotted as a function of temperature as shown in figure 6.5b. The parameters obtained from the fitting, such as A_1T and A_0 are listed in table 6.2.

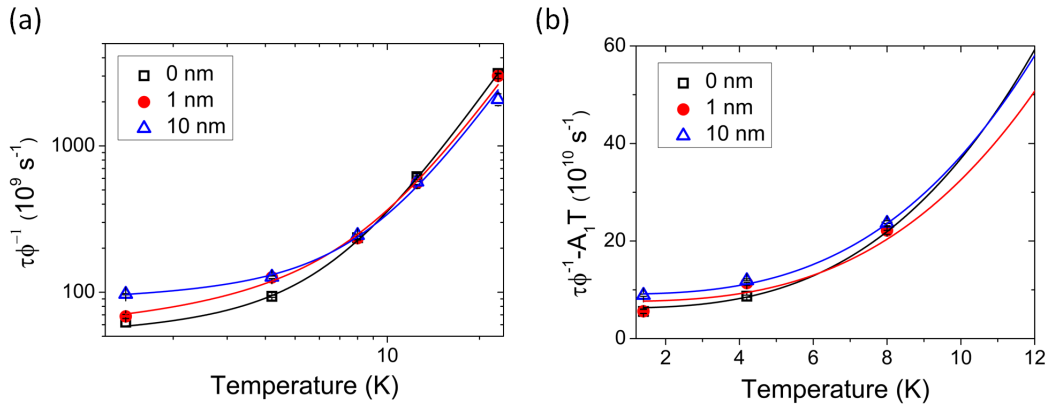

Figure 6.5: *(a) The phase breaking rate τ_ϕ^{-1} as a function of temperature for Cu(2.5)/C_{60}(x)/Cu(2.5)/Al(2) samples (the data in figure 4b), which was calculated with equation 2.15 (b) The corrected scattering rate $\tau_\phi^{-1} - A_1T$ for the elastic impurity scattering as a function of temperature. The solid lines are the fit to the data using power-law expansion (equation 6.1).*

Table 6.2: Fitting parameters extracted from the fits in figure 6.5. *R* is the sheet resistance measured at 4.2 K. In the investigated temperature range, the Cu film has a resistance of $R < 30\Omega/\square$ which is in the same limit as reported in previous studies [149]. *D* is the diffusion constant which was calculated using the formula 2.17. A_1 and A_0 are the parameters extracted from the power-law expansion fit and corresponds to electron-electron and magnetic scattering, respectively.

Sample	*x* (nm)	$R_{\square(4.20\pm0.01K)}$ ($\Omega/\square$)	D($\times10^{-3}$ m^2/s)	$A_1(10^9)$	$A_0(10^{10}); \tau_m^{-1}(s)$
1	0	(22.9209±0.0002)	4.6	(7±2)	(6.2 ±0.5)
2	1	(24.74798±0.00005)	4.3	(12±4)	(7±1)
3	10	(28.20289±0.00004)	3.8	(8±2)	(9.1 ±0.4)

The constant A_0 (as indicated in equation 6.1) represents a characteristic time related to scattering by magnetic impurities ($A_0\alpha\tau_m^{-1}$). This allows us to investigate the influence of magnetic spins on electron coherence in the metallic Cu films with and without C_{60}, and to study the role of molecular interfaces in altering the magnetic states of materials. A_0 is estimated from the fit to the data points in figure 6.5b to be $(6.2\pm0.5)\times10^9 s^{-1}$ for the pure Cu sample. The obtained value is comparable to previously reported values [153] with a high purity Cu source. On the other hand, the scattering rate due to magnetic scattering is enhanced to a value of $(7\pm1)\times10^9 s^{-1}$ by introducing a dusting layer of C_{60} between Cu layers while the sample with a 10 nm C_{60} layer exhibits a 47% rise in the magnetic scattering rate to a value of about $(9.1\pm0.4)\times10^9 s^{-1}$.

The magnetic scattering rate is usually varied proportionally to the amount of residual Kondo impurities (Cr, Fe, Ni, etc.). However, the difference in the results cannot be explained by a different concentration of residual magnetic impurities because all samples were deposited using the same 99.9999% pure Cu source within the same deposition. Hence, the concentration of impurities should be the same in all samples. The enhancement in the magnetic scattering rate for the sample with a 10 nm C_{60} layer can only be explained by assuming the existence of an additional magnetic source, other than the Kondo impurities, for instance the spin ordering that emerged due to Cu/C_{60} interface. The emergent magnetic moments can be associated with the hybridisation

and charge transfer between the molecular orbitals and the 3d band in the metal.

6.3 Conclusion

Low temperature electronic transport was used to study thin films of Cu with and without C_{60} interfaces. The Cu/C_{60} shows an upturn of the resistivity below a temperature of T_{min} $\approx$*14 K*, whereas the pure Cu film upturn temperature is approximately half this value $\approx$*7 K*. These findings are also in agreement with the resistivity behaviour that can be explained by the Kondo spin-flip scattering process. An analysis of the experimental resistivity and the MR confirms that a localized regime is established at low temperature. The MR behaviour at low temperatures exhibits a lower value in the Cu/C_{60} sample in comparison to the sample without C_{60} in both parallel and perpendicular orientations. This indicates a higher concentration of the magnetic spin in the presence of C_{60} that reduces the phase coherence. The dephasing effect due to the different scattering mechanism is studied using the theory of Hikami and the power-expansion law. This enabled us to calculate the scattering time due to the presence of magnetic spins. It has been confirmed that in the case of the Cu/C_{60} sample, an additional magnetic scattering process has been observed which therefore causes a rise in the dephasing time. The magnetic scattering rate for the Cu/C_{60} film corresponds to a higher concentration of magnetic moments that can only be explained by the presence of emergent magnetism. The emergent magnetism gives rise to this additional scattering rate and therefore causes an increase in the phase breaking mechanism.

CHAPTER 7

Conclusions and future work

Obtaining control of the interfacial spin polarisation at metallo-molecular interfaces is a crucial component in engineering the performance of future organic spintronic devices. Due to hybridization of molecular orbitals with the 3d orbitals of transition metals, new hybrid metal-organic interfacial states are formed. The electronic and magnetic properties of the organic and metallic systems are directly affected by these new states along with charge transfer process. It can lead to a change in the density of states at the Fermi energy and/or the exchange-correlation integral, causing an imbalance between spin-up and spin-down states as described by the Stoner criterion for ferromagnetism [25]. It is therefore possible to change the electronic states of non-ferromagnetic materials via molecular interfaces and transform them into magnetically ordered materials.

In this thesis, we have revealed the crucial role played by molecular interfaces in tailoring the spin order of contacting metals and transforming elements which have no magnetic contribution into materials that exhibit spontaneous magnetism at room temperature. Two different classes of transition metals have been investigated: diamagnetic (e.g. Cu) and paramagnetic (e.g. Mn and Sc). The magnetic response is confirmed by performing three different techniques; SQUID magnetometry, LE-μSR and XAS and the related technique XMCD; in which each technique probes specific details of the magnetic structure.

The data obtained using SQUID magnetometry to measure both classes of transition metals; diamagnetic Cu and paramagnetic Mn, in combination with C_{60} showed that the samples are ferromagnetic at room temperature, but only when/or it is maximised when the metallic layer is thin and continuous. In thick metallic layers, the bulk properties of the metal dominate, hence the charge transfer is screened by free electrons resulting in a quenching of the emergent magnetism. Decoupling the interface by an aluminium (or alumina) spacer prevents any electron transfer or hybridisation from arising due to the metallo-organic interface and hence quenches the magnetisation. In contrast, the paramagnetic Sc/C_{60} multilayers revealed different behaviour as the Sc layer became thinner. The magnetisation increased even below a 1-2 nm thin Sc layer, which could be explained by better wetting properties of C_{60} by Sc films, as the Sc

layer in this case would be continuous even at smaller thickness ($\sim$ 0.5 nm). The formation of superparamagnetic islands provides another mechanism that could describe the behaviour of the magnetisation in Sc ultrathin layers. Diamagnetic Cu/C_{60} showed stronger magnetisation (3–4 times) than that obtained in the paramagnetic Mn/C_{60} and Sc/C_{60} within the same metallic layer thickness (2-3 nm), which is probably due to the better lattice matching and larger charge transfer between Cu and C_{60}. Being paramagnetic, Mn and Sc are closer to complying with the Stoner criterion than diamagnetic Cu, the effects propagates longer due to the larger exchange interactions and DOS at the Fermi level.

Protecting the emergent magnetism from degradation and having reproducible results is important when dealing with organic molecules. This has been improved by increasing the number of interfaces, a good choice of capping and seed layer and/or annealing. The roughness at the interface as studied via XRR and AFM, has shown an effect on the quality of emergent spin ordering but a good control through annealing appears to improve the quality of interfaces and retains the magnetisation. With these findings, we confirmed that it is possible to improve the quality and reduce the degradation of the metallo-molecular interfaces, which are promising to overcome some disadvantages of organic devices and bring organics to the field of spintronics applications. However, being able to efficiently control the degradation that organic structures undergo and having smooth interfaces are necessary to improve the quality and make the spintronics industry profits from adopting this new promising class of magnetic materials. Molecules that are smooth and stable bind to a metallic surface, such as amorphous carbon, would provide control of film morphology and surface roughness that appears to be an obstacle to hinder the quality of our metallo-molecular materials.

LE-μSR corroborates the results obtained by magnetometry, but in particular gives more precise and detailed information about where the emergent spin ordering is localised within the sample. It showed that the emergent magnetism is localised at or close to the metallo-molecular interface. This is correlated with an additional frequency that appeared in the remanent state as muons approach the metallo-carbon interface. Decoupling the interface with alumina suppressed this additional frequency.

LE-μSR measurements for both multilayered structures of Cu and Sc have also confirmed that the spin ordering is a property of the thin metallic layers but it is reduced in thick metallic layers where the charge transfer is screened by thick films and suppresses any spin ordering associated with the process. The former creates spin ordering and gives rise to a rapid loss is the polarisation of muons. The muon response is confirmed through different measurements such as zero-field, zero-field remanent state and transverse field measurements. Also, low temperature measurements of the muonium state gave additional support to the presence of local spin ordering at the molecular interfaces. Altogether, the muon results provide evidence of the interfacial origin of the emergent spin ordering between the non-magnetic transition metals and C_{60}.

Being able to probe the electronic and magnetic properties of specific elements is a critical feature offered by XAS and XMCD. XMCD showed a sizable dichroism signal of about 5% of the XAS intensity observed in the C K-edge, suggesting spin ordering occurs due to hybridisation between C p_z and Sc 3d derived states at the interface. The molecular orbitals of C_{60} and specifically the π^* orbitals have shown a significant change in terms of broadening and energy shifts. This change in the molecular orbitals emphasizes the influence of charge transfer and hybridisation at the interface between the C_{60} molecules and the 3d band of the metal. The molecular orbitals have experienced even more changes when the system is cooled down at 4 K, where the rotation motion of C_{60} is frozen, and 18% enhancement in the XMCD signal was associated with this process. Although XAS has not served the purpose of investigating the magnetism in the metallic elements due to oxidation and low yield associated with the measured signal, it showed evidence that ruled out the presence of magnetic impurities that could give rise to the magnetism.

The work here presents conclusive evidence for the emergent spin ordering at metallo-C_{60} interfaces. Despite the emergent magnetism being about one or two orders of magnitude smaller than for ferromagnetic iron or cobalt, it could be maximised in the future by using molecules with a large electron affinity such as polyoxometalates. Also, metals with a large exchange integral such as zinc would facilitate satisfying the Stoner criterion. The ability to manipulate the spin ordering at metallic surfaces using

organic molecules and charge transfer could lead the work towards the future development of multifunctional devices such as for molecular memories and spin capacitors. This can take place via applying electric fields 'gating'. Application of electric field alters the charge transfer between the 3d metal and the p orbitals of carbon and hence the Fermi energy position at the interface. This change in the Fermi energy in turn affects the magnetic properties and enable a desired active control of the spin structure.

Low temperature electronic transport was also considered in this work paving the way towards spintronic applications. The localised spin ordering that is created at the metallo-molecular interfaces was studied through Kondo and WL; sensitive probes to determine spin ordering. The focus was on the Cu/C_{60} system using a six-nine pure Cu target. The Cu film shows logarithmic dependence of the resistivity on the temperature. However, when C_{60} is deposited into the Cu matrix, the emergent spin ordering gives rise to additional magnetic scattering and therefore causes an increase of the Kondo temperature T_K from 7 K to 14 K. An analysis of the experimental resistivity and the MR confirms that a WL regime is also established for both films at low temperature. Low temperature MR measurements caused by the WL in these films enable us to determine the temperature dependence of various dephasing rates within the films; spin-orbit interaction, mean free path and magnetic scattering using both the theory of Hikami [63] and the power-expansion law [152; 153]. The results confirmed the occurrence of an additional magnetic scattering that has a pronounced contribution when C_{60} molecules are embedded into the non-magnetic Cu. C_{60} creates localised spins that increase the concentration of magnetic moments in the Cu/C_{60} film and hence alter the magnetic scattering rate.

The spin dependent scattering studied by Kondo and WL could play an important role for quantum computation, as the electrons scattered from the same spin are mutually correlated. The ability to tune the spin-electron interaction via the control of charge transfer using gate voltages may have great promise with applications in low temperature thermometry and quantum devices.

In conclusion, this thesis shows the crucial role of metal/molecular interfaces in their magnetic properties. It raises the possibility of tailoring the electronic states

between different materials and switching the non-magnetic elements into magnetic ordered materials. The ability to create and manipulate the spin ordering will open the possibilities of exploring new molecular functionalities toward further research in spintronic applications. The spin ordering arising at the transition metal/C_{60} interfaces is not only of great potential leading to applications, but also shows there are a lot of new physics at metallo-molecular interfaces to be discovered. Further research in this exciting field would lead to a novel opportunity to incorporating new generation of materials into devices with multiple functionalities.

REFERENCES

[1] A. R. Rocha, V. M. Garcia-Suarez, S. W. Bailey, C. J. Lambert, J. Ferrer, and S. Sanvito, "Towards molecular spintronics," *Nature materials*, vol. 4, no. 4, pp. 335–339, 2005.

[2] K. V. Raman, "Interface-assisted molecular spintronics," *Applied Physics Reviews*, vol. 1, no. 3, p. 031101, 2014.

[3] K. V. Raman, A. M. Kamerbeek, A. Mukherjee, N. Atodiresei, T. K. Sen, P. Lazić, V. Caciuc, R. Michel, D. Stalke, S. K. Mandal, S. Blügel, M. Münzenberg, and J. S. Moodera, "Interface-engineered templates for molecular spin memory devices.," *Nature*, vol. 493, no. 7433, pp. 509–13, 2013.

[4] C. Barraud, C. Deranlot, P. Seneor, R. Mattana, B. Dlubak, S. Fusil, K. Bouzehouane, D. Deneuve, F. Petroff, and A. Fert, "Magnetoresistance in magnetic tunnel junctions grown on flexible organic substrates," *Applied Physics Letters*, vol. 96, no. 7, p. 2502, 2010.

[5] S. Parkin, "Flexible giant magnetoresistance sensors," *Applied physics letters*, vol. 69, no. 20, pp. 3092–3094, 1996.

[6] F. Yan, G. Xue, and F. Wan, "A flexible giant magnetoresistance sensor prepared completely by electrochemical synthesis," *Journal of Materials Chemistry*, vol. 12, no. 9, pp. 2606–2608, 2002.

[7] A. Bedoya-Pinto, M. Donolato, M. Gobbi, L. E. Hueso, and P. Vavassori, "Flexible spintronic devices on kapton," *Applied Physics Letters*, vol. 104, no. 6, p. 062412, 2014.

[8] D. McCamey, H. Seipel, S.-Y. Paik, M. Walter, N. Borys, J. Lupton, and C. Boehme, "Spin rabi flopping in the photocurrent of a polymer light-emitting diode," *Nature materials*, vol. 7, no. 9, pp. 723–728, 2008.

[9] C. Yang, E. Ehrenfreund, and Z. V. Vardeny, "Polaron spin-lattice relaxation time in π-conjugated polymers from optically detected magnetic resonance," *Physical review letters*, vol. 99, no. 15, p. 157401, 2007.

[10] Y. Sheng, T. Nguyen, G. Veeraraghavan, Ö. Mermer, and M. Wohlgenannt, "Effect of spin-orbit coupling on magnetoresistance in organic semiconductors," *Physical Review B*, vol. 75, no. 3, p. 035202, 2007.

[11] D. Huertas-Hernando, F. Guinea, and A. Brataas, "Spin-orbit coupling in curved graphene, fullerenes, nanotubes, and nanotube caps," *Physical Review B*, vol. 74, no. 15, p. 155426, 2006.

[12] S. Sanvito and A. R. Rocha, "Molecular-spintronics: the art of driving spin through molecules," *Journal of Computational and Theoretical Nanoscience*, vol. 3, no. 5, pp. 624–642, 2006.

[13] P. Bobbert, W. Wagemans, F. Van Oost, B. Koopmans, and M. Wohlgenannt, "Theory for spin diffusion in disordered organic semiconductors," *Physical review letters*, vol. 102, no. 15, p. 156604, 2009.

[14] A. V. Khaetskii and Y. V. Nazarov, "Spin-flip transitions between zeeman sublevels in semiconductor quantum dots," *Physical Review B*, vol. 64, no. 12, p. 125316, 2001.

[15] S. Sanvito, "Molecular spintronics: The rise of spinterface science," *Nature Physics*, vol. 6, pp. 562–564, 2010.

[16] K. Bairagi, A. Bellec, V. Repain, C. Chacon, Y. Girard, Y. Garreau, J. Lagoute, S. Rousset, R. Breitwieser, Y.-C. Hu, Y. C. Chao, W. W. Pai, D. Li, A. Smogunov, and C. Barreteau, "Tuning the Magnetic Anisotropy at a Molecule-Metal Interface," *Physical Review Letters*, vol. 114, no. 24, p. 247203, 2015.

[17] T. L. A. Tran, P. K. J. Wong, M. P. De Jong, W. G. Van Der Wiel, Y. Q. Zhan, and M. Fahlman, "Hybridization-induced oscillatory magnetic polarization of C_{60} orbitals at the C_{60}/Fe(001) interface," *Applied Physics Letters*, vol. 98, no. 22, pp. 10–13, 2011.

[18] T. Moorsom, M. Wheeler, T. Mohd Khan, F. Al Ma'Mari, C. Kinane, S. Langridge, D. Ciudad, A. Bedoya-Pinto, L. Hueso, G. Teobaldi, V. K. Lazarov, D. Gilks, G. Burnell, B. J. Hickey, and O. Cespedes, "Spin-polarized electron transfer in ferromagnet/C_{60} interfaces," *Physical Review B*, vol. 90, no. 12, p. 125311, 2014.

[19] M. Wheeler, B. Hickey, and O. Cespedes, "Enhanced exchange bias of spin valves fabricated on fullerene-based seed layers," *Magnetics, IEEE Transactions on*, vol. 48, no. 11, pp. 3047–3050, 2012.

[20] O. Céspedes, M. Ferreira, S. Sanvito, M. Kociak, and J. Coey, "Contact induced magnetism in carbon nanotubes," *Journal of Physics: Condensed Matter*, vol. 16, no. 10, p. L155, 2004.

[21] M. S. Ferreira and S. Sanvito, "Contact-induced spin polarization in carbon nanotubes," *Physical Review B*, vol. 69, no. 3, p. 035407, 2004.

[22] C. Barraud, P. Seneor, R. Mattana, S. Fusil, K. Bouzehouane, C. Deranlot, P. Graziosi, L. Hueso, I. Bergenti, V. Dediu, F. Petroff, and A. Fert, "Unravelling the role of the interface for spin injection into organic semiconductors," *Nature Physics*, vol. 6, no. 8, pp. 615–620, 2010.

[23] M. Gruber, F. Ibrahim, S. Boukari, H. Isshiki, L. Joly, M. Peter, M. Studniarek, V. Da Costa, H. Jabbar, V. Davesne, *et al.*, "Exchange bias and room-temperature magnetic order in molecular layers," *Nature materials*, 2015.

[24] S. Heutz, "Molecular spintronics: A warm exchange," *Nature materials*, vol. 14, no. 10, pp. 967–968, 2015.

[25] J. F. Janak, "Uniform susceptibilities of metallic elements," *Physical Review B*, vol. 16, no. 1, pp. 255–262, 1977.

[26] L.-S. Wang, J. Conceicao, C. Jin, and R. Smalley, "Threshold photodetachment of cold C_{60}," *Chemical physics letters*, vol. 182, no. 1, pp. 5–11, 1991.

[27] R. Lof, M. Van Veenendaal, B. Koopmans, H. Jonkman, and G. Sawatzky, "Band gap, excitons, and Coulomb interaction in solid C_{60}," *Physical review letters*, vol. 68, no. 26, p. 3924, 1992.

[28] T. Ohno, Y. Chen, S. Harvey, G. Kroll, J. Weaver, R. Haufler, and R. Smalley, "C_{60} bonding and energy-level alignment on metal and semiconductor surfaces," *Physical Review B*, vol. 44, no. 24, p. 13747, 1991.

[29] J. Weaver, J. L. Martins, T. Komeda, Y. Chen, T. Ohno, G. Kroll, N. Troullier, R. Haufler, and R. Smalley, "Electronic structure of solid C_{60}: experiment and theory," *Physical review letters*, vol. 66, no. 13, p. 1741, 1991.

[30] D. Thouless, "Magnetism in condensed matter by Stephen Blundell," *American Journal of Physics*, vol. 71, no. 1, pp. 94–94, 2003.

[31] J. M. Coey, *Magnetism and magnetic materials*. Cambridge University Press, 2010.

[32] E. C. Stoner, "Collective electron ferromagnetism," *Proceedings of the Royal Society of London. Series A, Mathematical and Physical Sciences*, pp. 372–414, 1938.

[33] S. von Oehsen, *Spin-polarized currents for spintronic devices: point-contact Andreev reflection and spin filters*. Cuvillier Verlag, 2007.

[34] M. Verdaguer, "Molecular electronics emerges from molecular magnetism," *Science*, vol. 272, no. 5262, p. 698, 1996.

[35] D. Gatteschi, "Molecular magnetism: A basis for new materials," *Advanced Materials*, vol. 6, no. 9, pp. 635–645, 1994.

[36] J. S. Miller and D. Gatteschi, "Molecule-based magnets," *Chem. Soc. Rev.*, vol. 40, pp. 3065–3066, 2011.

[37] H. M. McConnell, "Ferromagnetism in solid free radicals," *The Journal of Chemical Physics*, vol. 39, no. 7, pp. 1910–1910, 1963.

[38] H. McConnell, "Comments about "organic ferromagnetism"," in *Proc. Robert A. Welch Found. Conf. Chem. Res*, vol. 11, pp. 144–150, 1967.

[39] J. S. Miller, A. J. Epstein, and W. M. Reiff, "Ferromagnetic molecular charge-transfer complexes," *Chemical Reviews*, vol. 88, no. 1, pp. 201–220, 1988.

[40] J. M. Manriquez, G. T. Yee, R. S. McLean, A. J. Epstein, and J. S. Miller, "A room-temperature molecular/organic-based magnet," *Science*, vol. 252, no. 5011, pp. 1415–1417, 1991.

[41] E. M. Chudnovsky, "Quantum hysteresis in molecular magnets," *Science*, vol. 274, no. 5289, p. 938, 1996.

[42] M. Mannini, F. Pineider, C. Danieli, F. Totti, L. Sorace, P. Sainctavit, M.-A. Arrio, E. Otero, L. Joly, J. C. Cezar, *et al.*, "Quantum tunnelling of the magnetization in a monolayer of oriented single-molecule magnets," *Nature*, vol. 468, no. 7322, pp. 417–421, 2010.

[43] S. Heutz, C. Mitra, W. Wu, A. J. Fisher, A. Kerridge, M. Stoneham, A. Harker, J. Gardener, H.-H. Tseng, T. S. Jones, *et al.*, "Molecular thin films: a new type of magnetic switch," *Advanced Materials*, vol. 19, no. 21, pp. 3618–3622, 2007.

[44] D. Langreth, B. I. Lundqvist, S. D. Chakarova-Käck, V. Cooper, M. Dion, P. Hyldgaard, A. Kelkkanen, J. Kleis, L. Kong, S. Li, *et al.*, "A density functional for sparse matter," *Journal of Physics: Condensed Matter*, vol. 21, no. 8, p. 084203, 2009.

[45] N. Atodiresei, V. Caciuc, P. Lazic, and S. Blügel, "Chemical and van der waals interactions at hybrid organic-metal interfaces," *http://psi-k.org*.

[46] J. B. Neaton, M. S. Hybertsen, and S. G. Louie, "Renormalization of molecular electronic levels at metal-molecule interfaces," *Physical review letters*, vol. 97, no. 21, p. 216405, 2006.

[47] S. Steil, N. Großmann, M. Laux, A. Ruffing, D. Steil, M. Wiesenmayer, S. Mathias, O. L. Monti, M. Cinchetti, and M. Aeschlimann, "Spin-dependent trapping of electrons at spinterfaces," *Nature Physics*, vol. 9, no. 4, pp. 242–247, 2013.

[48] D. Çakır, D. M. Otálvaro, and G. Brocks, "From spin-polarized interfaces to giant magnetoresistance in organic spin valves," *Physical Review B*, vol. 89, no. 11, p. 115407, 2014.

[49] N. Baadji and S. Sanvito, "Giant resistance change across the phase transition in spin-crossover molecules," *Physical review letters*, vol. 108, no. 21, p. 217201, 2012.

[50] M. Gobbi, F. Golmar, R. Llopis, F. Casanova, and L. E. Hueso, "Room-Temperature Spin Transport in C_{60}-Based Spin Valves," *Advanced Materials*, vol. 23, no. 14, pp. 1609–1613, 2011.

[51] X. Zhang, S. Mizukami, Q. Ma, T. Kubota, M. Oogane, H. Naganuma, Y. Ando, and T. Miyazaki, "Spin-dependent transport behavior in C_{60} and Alq_3 based spin valves with a magnetite electrode," *Journal of Applied Physics*, vol. 115, no. 17, p. 172608, 2014.

[52] X. Zhang, S. Mizukami, T. Kubota, Q. Ma, M. Oogane, H. Naganuma, Y. Ando, and T. Miyazaki, "Observation of a large spin-dependent transport length in organic spin valves at room temperature," *Nature communications*, vol. 4, p. 1392, 2013.

[53] H. W. Kroto, J. R. Heath, S. C. O'Brien, R. F. Curl, and R. E. Smalley, "C_{60}: buckminsterfullerene," *Nature*, vol. 318, p. 162, 1985.

[54] R. Lin, F. Wang, M. Wohlgenannt, C. He, X. Zhai, and Y. Suzuki, "Organic spin-valves based on fullerene C_{60}," *Synthetic Metals*, vol. 161, no. 7, pp. 553–557, 2011.

[55] S. Braun, W. R. Salaneck, and M. Fahlman, "Energy-level alignment at organic/metal and organic/organic interfaces," *Advanced Materials*, vol. 21, no. 14-15, pp. 1450–1472, 2009.

[56] T. Tran, T. Q. Le, J. G. Sanderink, W. G. van der Wiel, and M. P. de Jong, "The multistep tunneling analogue of conductivity mismatch in organic spin valves," *Advanced functional materials*, vol. 22, no. 6, pp. 1180–1189, 2012.

[57] S. Liang, R. Geng, B. Yang, W. Zhao, R. C. Subedi, X. Li, X. Han, and T. D. Nguyen, "Curvature-enhanced spin-orbit coupling and spinterface effect in fullerene-based spin valves," *Scientific reports*, vol. 6, 2016.

[58] W. David, R. Ibberson, T. Dennis, J. Hare, and K. Prassides, "Structural phase transitions in the fullerene C_{60}," *EPL (Europhysics Letters)*, vol. 18, no. 3, p. 219, 1992.

[59] J. Kondo, "Resistance minimum in dilute magnetic alloys," *Progress of Theoretical Physics*, vol. 32, no. 1, pp. 37–49, 1964.

[60] K. Yosida, *Theory of Magnetism.: Edition en anglais*, vol. 122. Springer Science & Business Media, 1996.

[61] E. Abrahams, P. Anderson, D. Licciardello, and T. Ramakrishnan, "Scaling theory of localization: Absence of quantum diffusion in two dimensions," *Physical Review Letters*, vol. 42, no. 10, p. 673, 1979.

[62] G. Bergmann, "Weak localization in thin films," *Physica Scripta*, vol. 107, no. 1, pp. 1–58, 1984.

[63] S. Hikami, A. I. Larkin, and Y. Nagaoka, "Spin-orbit interaction and magnetoresist ance in the two dimensional random system," *Progress in Theoretical Physics*, vol. 63, no. 2, pp. 707–710, 1980.

[64] B. Kramer, G. Bergmann, and Y. Bruynseraede, *Localization, interaction, and transport phenomena: Proceedings of the International Conference, August 23–28, 1984 Braunschweig, Fed. Rep. of Germany*, vol. 61. Springer Science & Business Media, 2012.

[65] K. Seshan, *Handbook of thin-film deposition processes and techniques - principles, methods, equipment and applications (2nd Edition)*. William Andrew Publishing/Noyes, oct 2002.

[66] E. Williams, "An introduction to sputtering of magnetic and magneto-optic thin films for data recording," *Journal of Magnetism and Magnetic Materials*, vol. 95, pp. 356–364, may 1991.

[67] K. Ellmer, "Magnetron sputtering of transparent conductive zinc oxide: relation between the sputtering parameters and the electronic properties," *Journal of Physics D: Applied Physics*, vol. 33, no. 4, pp. R17–R32, 2000.

[68] B. Bhushan, J. V. Coe Jr, and B. Gupta, "Method for coating fullerene materials for tribology," Sept. 24 1996.

[69] R. Pankajavalli, C. Mallika, O. Sreedharan, M. Premila, and P. Gopalan, "Vapour pressure of C_{60} by a transpiration method using a horizontal thermobalance," *Thermochimica acta*, vol. 316, no. 1, pp. 101–108, 1998.

[70] M. C. Wheeler, *Manipulation of fullerene C_{60} spintronic devices via ferromagnetic resonance*. PhD thesis, 2014.

[71] F. Al Ma'Mari, T. Moorsom, G. Teobaldi, W. Deacon, T. Prokscha, H. Luetkens, S. Lee, G. E. Sterbinsky, D. A. Arena, D. A. Maclaren, M. Flokstra, M. Ali, M. C. Wheeler, G. Burnell, B. J. Hickey, and O. Cespedes, "Beating the Stoner criterion using molecular interfaces," *Nature*, vol. 254, pp. 69–74, 2015.

[72] D. Windover, E. Barnat, J. Kim, M. Nielsen, T. Lu, A. Kumar, H. Bakhru, C. Jin, and S. Lee, "Thin film density determination by multiple radiation energy dispersive x-ray reflectivity," *JCPDS–International Center of Diffraction Data*, 2000.

[73] J. Als-Nielsen and D. McMorrow, *Elements of modern X-ray physics*. John Wiley & Sons, 2011.

[74] L. G. Parratt, "Surface studies of solids by total reflection of x-rays," *Physical review*, vol. 95, no. 2, p. 359, 1954.

[75] H. Kiessig, "Untersuchungen zur totalreflexion von röntgenstrahlen," *Annalen der Physik*, vol. 402, no. 6, pp. 715–768, 1931.

[76] U. Pietsch, V. Holy, and T. Baumbach, *High-resolution X-Ray scattering: from thin films to lateral nanostructures*. Advanced Texts in Physics, Springer New York, 2004.

[77] J. Als-Nielsen and D. McMorrow, *Elements of modern X-ray physics*. Wiley, 2001.

[78] M. Sugawara, M. Kondo, S. Yamazaki, and K. Nakajima, "Exact determination of superlattice structures by small-angle x-ray diffraction method," *Applied physics letters*, vol. 52, no. 9, pp. 742–744, 1988.

[79] M. Wormington, C. Panaccione, K. M. Matney, and D. K. Bowen, "Characterization of structures from x-ray scattering data using genetic algorithms," *Philosophical Transactions of the Royal Society of London A: Mathematical, Physical and Engineering Sciences*, vol. 357, no. 1761, pp. 2827–2848, 1999.

[80] N. Jalili and K. Laxminarayana, "A review of atomic force microscopy imaging systems: Application to molecular metrology and biological sciences," *Mechatronics*, vol. 14, no. 8, pp. 907–945, 2004.

[81] A. San Paulo and R. Garcia, "Unifying theory of tapping-mode atomic-force microscopy," *Physical Review B*, vol. 66, no. 4, p. 041406, 2002.

[82] R. Garcıa and R. Perez, "Dynamic atomic force microscopy methods," *Surface science reports*, vol. 47, no. 6, pp. 197–301, 2002.

[83] P. Klapetek, D. Necas, and C. Anderson, "Gwyddion user guide," *Online http://gwyddion. net*, 2004.

[84] A. Chtchelkanova, S. A. Wolf, and Y. Idzerda, *Magnetic interactions and spin transport*. Springer Science & Business Media, 2013.

[85] J. Clarke and A. I. Braginski, *The SQUID handbook, vol. 1 Fundamentals and technology of SQUID and SQUID systems*. Wiley-VCH Verlag GmbH & Co. KGaA, 2004.

[86] C. Graham, "High-sensitivity magnetization measurements," *Journal of Materials Sciences and Technology*, vol. 16, no. 02, pp. 97–101, 2000.

[87] *Magnetic property measurement system SQUID VSM everCool option user's manual*. Quantum Design, 2007.

[88] S. J. Blundell, "Spin-polarized muons in condensed matter physics," *Contemporary Physics*, vol. 40, no. 3, pp. 175–192, 1999.

[89] P. Bakule and E. Morenzoni, "Generation and applications of slow polarized muons," *Contemporary Physics*, vol. 45, no. 3, pp. 203–225, 2004.

[90] E. Morenzoni, E. M. Forgan, H. Glückler, T. J. Jackson, H. Luetkens, C. Niedermayer, T. Prokscha, T. M. Riseman, M. Birke, A. Hofer, J. Litterst, M. Pleines, and G. Schatz, "Muon spin rotation and relaxation experiments on thin films," *Hyperfine Interactions*, vol. 133, no. 1-4, pp. 179–195, 2001.

[91] T. Prokscha, E. Morenzoni, C. David, a. Hofer, H. Glückler, and L. Scandella, "Moderator gratings for the generation of epithermal positive muons," *Applied Surface Science*, vol. 172, no. 3-4, pp. 235–244, 2001.

[92] S. F. J. Cox, "Implanted muon studies in condensed matter science," *Journal of Physics C: Solid State Physics*, vol. 20, no. 22, pp. 3187–3319, 1987.

[93] A. Suter and B. Wojek, "Musrfit: a free platform-independent framework for μsr data analysis," *Physics Procedia*, vol. 30, pp. 69–73, 2012.

[94] J. Yano and V. K. Yachandra, "X-ray absorption spectroscopy," *Photosynthesis Research*, vol. 102, no. 2, pp. 241–254, 2009.

[95] J. Stöhr, "Exploring the microscopic origin of magnetic anisotropies with X-ray magnetic circular dichroism (XMCD) spectroscopy," *Journal of Magnetism and Magnetic Materials*, vol. 200, no. 1, pp. 470–497, 1999.

[96] G. van der Laan and A. I. Figueroa, "X-ray magnetic circular dichroism - A versatile tool to study magnetism," *Coordination Chemistry Reviews*, vol. 277, pp. 95–129, 2014.

[97] A. Rose-Innes, *Low Temperature Laboratory Techniques*. English Universities Press, 1973.

[98] S. Cho, Y. Yi, J. Seo, C. Kim, M. Noh, K.-H. Yoo, K. Jeong, and C.-N. Whang, "Origin of charge transfer complex resulting in ohmic contact at the C_{60}/Cu interface," *Synthetic metals*, vol. 157, no. 2, pp. 160–164, 2007.

[99] W. W. Pai, H. Jeng, C.-M. Cheng, C.-H. Lin, X. Xiao, A. Zhao, X. Zhang, G. Xu, X. Shi, M. Van Hove, *et al.*, "Optimal electron doping of a C_{60} monolayer on Cu(111) via interface reconstruction," *Physical review letters*, vol. 104, no. 3, p. 036103, 2010.

[100] D. Kittel and P. McEuen, *Introduction to solid state physics*, vol. 8. Wiley New York, 1976.

[101] A. J. Drew, J. Hoppler, L. Schulz, F. Pratt, P. Desai, P. Shakya, T. Kreouzis, W. Gillin, A. Suter, N. Morley, *et al.*, "Direct measurement of the electronic spin diffusion length in a fully functional organic spin valve by low-energy muon spin rotation," *Nature materials*, vol. 8, no. 2, pp. 109–114, 2009.

[102] P. D. De Reotier and A. Yaouanc, "Muon spin rotation and relaxation in magnetic materials," *Journal of Physics: Condensed Matter*, vol. 9, no. 43, p. 9113, 1997.

[103] W. Eckstein, *Computer simulation of ion-solid interactions*, vol. 10. Springer Science & Business Media, 2013.

[104] E. Morenzoni, H. Glückler, T. Prokscha, R. Khasanov, H. Luetkens, M. Birke, E. Forgan, C. Niedermayer, and M. Pleines, "Implantation studies of kev positive muons in thin metallic layers," *Nuclear Instruments and Methods in Physics Research Section B: Beam Interactions with Materials and Atoms*, vol. 192, no. 3, pp. 254–266, 2002.

[105] E. Ansaldo, C. Niedermayer, and C. Stronach, "Muonium in fullerite," 1991.

[106] C. Niedermayer, "Fullerenes with μSR," *Hyperfine interactions*, vol. 97, no. 1, pp. 285–304, 1996.

[107] T. Duty, J. Brewer, K. Chow, R. Kiefl, A. MacFarlane, G. Morris, J. Schneider, B. Hitti, R. Lichti, L. Brard, *et al.*, "Zero-field μSR in crystalline C_{60}," $Hyperfine Interactions, vol.\ 86, no.\ 1, pp.\ 789 - -795, 1994.$

[108] S. G. Das, "Electronic structure and magnetic properties of scandium," *Physical Review B*, vol. 13, no. 9, p. 3978, 1976.

[109] L.-L. Wang and H.-P. Cheng, "Rotation, translation, charge transfer, and electronic structure of C_{60} on Cu(111) surface," *Physical Review B*, vol. 69, no. 4, p. 045404, 2004.

[110] K.-D. Tsuei, J.-Y. Yuh, C.-T. Tzeng, R.-Y. Chu, S.-C. Chung, and K.-L. Tsang, "Photoemission and photoabsorption study of C_{60} adsorption on Cu(111) surfaces," *Physical Review B*, vol. 56, no. 23, pp. 15412–15420, 1997.

[111] A. Niklasson, S. Mirbt, H. L. Skriver, and B. Johansson, "Quantum-well-induced ferromagnetism in thin films," *Physical Review B*, vol. 56, no. 6, p. 3276, 1997.

[112] S. C. Hong, J. I. Lee, and R. Wu, "Ferromagnetism in pd thin films induced by quantum well states," *Physical Review B*, vol. 75, no. 17, p. 172402, 2007.

[113] S. Mirbt, B. Johansson, and H. L. Skriver, "Quantum-well-driven magnetism in thin films," *Physical Review B*, vol. 53, no. 20, p. R13310, 1996.

[114] S. Sakuragi, T. Sakai, S. Urata, S. Aihara, A. Shinto, H. Kageshima, M. Sawada, H. Namatame, M. Taniguchi, and T. Sato, "Thickness-dependent appearance of ferromagnetism in Pd(100) ultrathin films," *Physical Review B*, vol. 90, no. 5, p. 054411, 2014.

[115] R. Fink, C. Ballentine, J. Erskine, and J. A. Araya-Pochet, "Experimental probe for thin-film magnetism in p($1\times$ 1) Pd and V on Ag(100)," *Physical Review B*, vol. 41, no. 14, p. 10175, 1990.

[116] J. Ortega, F. Himpsel, G. Mankey, and R. Willis, "Quantum-well states and magnetic coupling between ferromagnets through a noble-metal layer," *Physical Review B*, vol. 47, no. 3, p. 1540, 1993.

[117] P. Loly and J. Pendry, "Removing the limits to accurate band-structure determination by photoemission," *Journal of Physics C: Solid State Physics*, vol. 16, no. 2, p. 423, 1983.

[118] T. Miller, A. Samsavar, G. Franklin, and T.-C. Chiang, "Quantum-well states in a metallic system: Ag on Au(111)," *Physical review letters*, vol. 61, no. 12, p. 1404, 1988.

[119] F. Himpsel, "Fe on au (100): Quantum-well states down to a monolayer," *Physical Review B*, vol. 44, no. 11, p. 5966, 1991.

[120] P. Bruno and C. Chappert, "Ruderman-kittel theory of oscillatory interlayer exchange coupling," *Physical Review B*, vol. 46, no. 1, p. 261, 1992.

[121] C. Chappert and J. Renard, "Long-period oscillating interactions between ferromagnetic layers separated by a nonmagnetic metal: a simple physical picture," *EPL (Europhysics Letters)*, vol. 15, no. 5, p. 553, 1991.

[122] P. Bruno and C. Chappert, "Erratum: Oscillatory coupling between ferromagnetic layers separated by a nonmagnetic metal spacer [phys. rev. lett. 67, 1602 (1991)]," *Physical Review Letters*, vol. 67, p. 2592, 1991.

[123] Q. Chen and Z. J. Zhang, "Size-dependent superparamagnetic properties of $MgFe_2O_4$ spinel ferrite nanocrystallites," *Applied physics letters*, vol. 73, p. 3156, 1998.

[124] J. Vejpravova, V. Sechovskỳ, D. Niznanskỳ, J. Plocek, A. Hutlová, and J. Rehspringer, "Superparamagnetism of co-ferrite nanoparticles," *Proceeding of Contributed Paper, Part III (WDS'05)*, pp. 518–523, 2005.

[125] P. Joy, P. A. Kumar, and S. Date, "The relationship between field-cooled and zero-field-cooled susceptibilities of some ordered magnetic systems," *Journal of Physics: Condensed Matter*, vol. 10, no. 48, p. 11049, 1998.

[126] B. D. Cullity and C. D. Graham, *Introduction to magnetic materials*. John Wiley & Sons, 2009.

[127] B. Wästberg, S. Lunell, C. Enkvist, P. A. Brühwiler, A. J. Maxwell, and N. Mårtensson, "1s X-ray absorption spectroscopy of C_{60}: The effects of screening and core-hole relaxation," *Physical Review B*, vol. 50, no. 17, p. 13031, 1994.

[128] M. Weser, Y. Rehder, K. Horn, M. Sicot, M. Fonin, A. B. Preobrajenski, E. N. Voloshina, E. Goering, and Y. S. Dedkov, "Induced magnetism of carbon atoms at the graphene/Ni(111) interface," *Applied Physics Letters*, vol. 96, no. 1, p. 012504, 2010.

[129] T. Tran, P. K. J. Wong, M. De Jong, W. van der Wiel, Y. Zhan, and M. Fahlman, "Hybridization-induced oscillatory magnetic polarization of C_{60} orbitals at the C_{60}/Fe(001) interface," *Applied Physics Letters*, vol. 98, no. 22, p. 222505, 2011.

[130] P. J. Wong, W. Zhang, K. Wang, G. van der Laan, Y. Xu, W. G. van der Wiel, and M. P. de Jong, "Electronic and magnetic structure of C_{60}/Fe_3O_4(001): a hybrid interface for organic spintronics," *Journal of materials chemistry C*, vol. 1, no. 6, pp. 1197–1202, 2013.

[131] Y. Zhu, *Modern techniques for characterizing magnetic materials*. Springer Science & Business Media, 2005.

[132] A. Maxwell, P. Brühwiler, A. Nilsson, N. Mårtensson, and P. Rudolf, "Photoemission, autoionization, and X-ray-absorption spectroscopy of ultrathin-film C_{60} on Au(110)," *Physical Review B*, vol. 49, no. 15, p. 10717, 1994.

[133] A. Maxwell, P. Brühwiler, S. Andersson, D. Arvanitis, B. Hernnäs, O. Karis, D. Mancini, N. Mårtensson, S. Gray, M.-J. Johansson, *et al.*, "C_{60} on Al(111): Covalent bonding and surface reconstruction," *Physical Review B*, vol. 52, no. 8, p. R5546, 1995.

[134] A. Maxwell, P. Brühwiler, D. Arvanitis, J. Hasselström, and N. Mårtensson, "Length Scales in Core Level Excitation: C 1s X-Ray Absorption of C_{60}/Al," *Physical review letters*, vol. 79, no. 8, p. 1567, 1997.

[135] A. Maxwell, P. Brühwiler, D. Arvanitis, J. Hasselström, M.-J. Johansson, and N. Mårtensson, "Electronic and geometric structure of C_{60} on Al(111) and Al(110)," *Physical Review B*, vol. 57, no. 12, p. 7312, 1998.

[136] L. Terminello, D. Shuh, F. Himpsel, D. Lapiano-Smith, J. Stöhr, D. Bethune, and G. Meijer, "Unfilled orbitals of C_{60} and C_{70} from carbon K-shell X-ray absorption fine structure," *Chemical physics letters*, vol. 182, no. 5, pp. 491–496, 1991.

[137] R. Haddon, "Electronic structure, conductivity and superconductivity of alkali metal doped (C_{60})," *Accounts of chemical research*, vol. 25, no. 3, pp. 127–133, 1992.

[138] R. Haddon, L. E. Brus, and K. Raghavachari, "Electronic structure and bonding in icosahedral C_{60}," *Chemical Physics Letters*, vol. 125, no. 5, pp. 459–464, 1986.

[139] S. Satpathy, V. Antropov, O. Andersen, O. Jepsen, O. Gunnarsson, and A. Liechtenstein, "Conduction-band structure of alkali-metal-doped C_{60}," *Physical Review B*, vol. 46, no. 3, p. 1773, 1992.

[140] P. Brühwiler, A. Maxwell, P. Rudolf, C. Gutleben, B. Wästberg, and N. Mårtensson, "C 1s autoionization study of electron hopping rates in solid C_{60}," *Physical review letters*, vol. 71, no. 22, p. 3721, 1993.

[141] M. Pedio, F. Borgatti, A. Giglia, N. Mahne, S. Nannarone, S. Giovannini, C. Cepek, E. Magnano, G. Bertoni, E. Spiller, *et al.*, "Annealing temperature dependence of C_{60} on silicon surfaces: bond evolution and fragmentation as detected by NEXAFS," *Physica Scripta*, vol. 2005, no. T115, p. 695, 2005.

[142] P. Brühwiler, O. Karis, and N. Mårtensson, "Charge-transfer dynamics studied using resonant core spectroscopies," *Reviews of Modern Physics*, vol. 74, no. 3, p. 703, 2002.

[143] A. Patnaik, K. K. Okudaira, S. Kera, H. Setoyama, K. Mase, and N. Ueno, "Polarized near-edge X-ray-absorption fine structure spectroscopy of C_{60}-functionalized 11-amino-1-undecane thiol self-assembled monolayer: molecular orientation and evidence for C_{60} aggregation.," *The Journal of chemical physics*, vol. 122, no. 15, pp. 154703–154703, 2005.

[144] A. A. Abrikosov and A. Beknazarov, *Fundamentals of the theory of metals*, vol. 1. North-Holland Amsterdam, 1988.

[145] P. A. Lee and T. Ramakrishan, "Disordered electronic systems," *Reviwe of Modern Physics*, vol. 57, no. 2, pp. 287–337, 1985.

[146] J. B. Boyce and C. P. Slichter, "Conduction-electron spin density around Fe impurities in Cu above and below TK," *Physical Review Letters*, vol. 32, no. 2, pp. 61–64, 1974.

[147] J. S. Dugdale, *The electrical properties of disordered metals*. Cambridge University Press, 2005.

[148] C. Barone, F. Romeo, S. Pagano, C. Attanasio, G. Carapella, C. Cirillo, A. Galdi, G. Grimaldi, A. Guarino, A. Leo, A. Nigro, and P. Sabatino, "Nonequilibrium fluctuations as a distinctive feature of weak localization," *Scientific Reports*, vol. 5, p. 10705, 2015.

[149] C. Van Haesendonck, L. Van den Dries, Y. Bruynsraede, and G. Deutscher, "Negative magnetoresistance in thin copper films," *Physica B+ C*, vol. 107, no. 1, pp. 7–8, 1981.

[150] J. Dai and J. Tang, "Weak localization and magnetoresistance of island-like thin copper films," *Journal of Applied Physics*, vol. 92, no. 10, pp. 6047–6050, 2002.

[151] A. J. Trionfi, *Electron phase coherence in mesoscopic normal metal wires* . PhD thesis, 2007.

[152] J. Vranken, C. Van Haesendonck and Y. Bruynseraede, "Enhanced magnetic surface scattering of weakly localized electrons," *Phys. Rev. B*, vol. 37, no. 14, p. 8502(R), 1988.

[153] C. V. Haesendonck, J. Vranken, and Y. Bruynseraede, "Resonant Kondo scattering of weakly localized electrons," *Physical Review Letters*, vol. 58, no. 19, pp. 1968–1971, 1987.